Charles University in Prague
Faculty of Mathematics and Physics

Femtoscopy with multi-strange baryons at RHIC

Doctoral Thesis

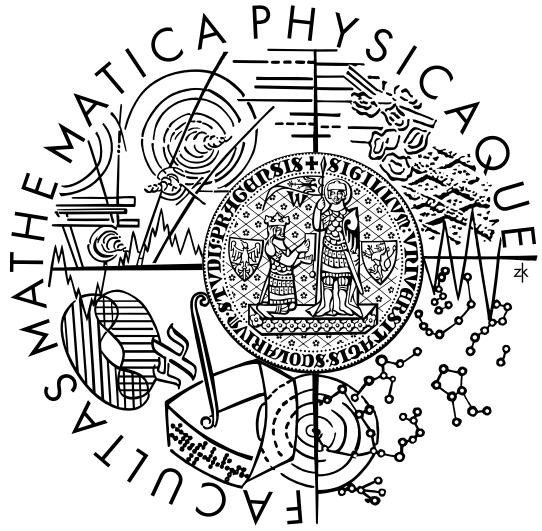

Mgr. Petr Chaloupka

Supervisor: prom. fyz. Michal Šumbera CSc.
Nuclear Physics Institute ASCR

June, 2010

Declaration of Originality

This doctoral thesis contains results of my research carried out at the Nuclear Physics Institute between years 2002 to 2010. Some of this work was carried out within STAR Collaboration.

Excluding introductory parts the research described in this thesis is original unless where an explicit reference is made to work of others. I further state that no part of this thesis or any substantially the same has been submitted for any qualification other than the degree of Doctor of Philosophy as the Charles University in Prague.

Abstrakt

Dosavadní výsledky měření jádro-jaderných srážek na RHIC naznačují, že hmota vytvořená ve srážkách prochází během svého vývoje fází, v které dominují partonové stupně volnosti. Tato horká a hustá hmota vykazuje silný stupeň kolektivního chování, které se projevuje silnou transversální expanzí. Zvláště zajímavé jsou výsledky měření eliptického toku baryonů s vícenásobnou podivností (Ξ a Ω), které ukazují, že i tyto částice se podstatnou mírou účastní kolektivní expanze. Výsledky takovýchto měření jsou silně závislé od toho, zda k rozvoji kolektivního chování došlo během pozdní (hadronové) fáze a nebo již dříve během rané (partonové) fáze. Vzhledem k tomu, že se předpokládá, že baryony s vícenásobnou podivností mají malé hadronové účinné průřezy a tudíž se ze systému oddělí dříve než ostatní částice, lze usuzovat, že měření s nimi budou citlivá především na možnou partonovou fázi vývoje systému.

Hlavním cílem této práce je studovat femtoskopické korelace mezi piony a Ξ ve srážkách zlato-zlato při energiích srážky na nukleonový pár $\sqrt{s_{NN}}$=200 GeV a $\sqrt{s_{NN}}$=62 GeV, které byly zaznamenány experimentem STAR na urychlovači RHIC. Měření dvoučásticových korelací v hybnostním prostoru při malých relativních rychlostech slouží ke studiu prostoro-časových rozměrů emisních zdrojů. Tato měření s využitím párů neidentických částic jsou citlivá nejen k rozměrům zdroje, ale také k relativním prostoro-časovým asymetriím mezi zdroji těchto dvou druhů částic. Vzhledem k tomu, že tato asymetrie může vzniknout jako důsledek kolektivní expanze, nebo popřípadě brzkého vyzáření Ξ, mohou být výsledky měření $\pi-\Xi$ korelací použity ke studiu dynamiky systému vzniklého při srážce těžkých jader.

V této práci jsou prezentovány vůbec první výsledky femtoskopických měření s použitím baryonů s vícenásobnou podivností. V měřené korelační funkci je pozorován jak efekt elektromagnetické tak i silné interakce, která se projevuje v podobě rezonance $\Xi^*(1530)$. Toto je také zároveň první pozorování této rezonance ve srážkách těžkých jader.

Výsledky těchto měření ukazují, že ve srážkách zlato-zlato při energiích srážky na nukleonový pár $\sqrt{s_{NN}}$=200 GeV a $\sqrt{s_{NN}}$=62 GeV se liší zdroj pionů a Ξ nejen svou velikostí, ale oba zdoje jsou vůči sobě i posunuty v prostoro-čase. V této práci je také ukázáno, že tato pozorovaná asymetrie je v souladu s předpovědmi modelů, které předpokládají účast vícenásobně podivných baryonů na kolektivní expanzi. Toto měření je tak nezávislým potvrzení transverzálního toku baryonů s vícenásobnou podivností.

Abstract

Au-Au collisions at RHIC energies exhibit features suggesting that the system has undergone evolution through a stage of partonic matter. The hot and dense system created in the collision builds up substantial collectivity leading to rapid transverse expansion. In particular recent measurements show that Ξ and Ω baryons develop substantial elliptic flow. Properties of the induced flow strongly depend on whether the collectivity is achieved on partonic or hadronic level. Multi-strange baryons may be, due to their presumably small hadronic cross-sections, mainly sensitive to the early (possibly partonic) stage.

The main objective of this thesis is to study femtoscopic $\pi-\Xi$ correlations in Au+Au collisions at $\sqrt{s_{NN}}$=200 GeV and $\sqrt{s_{NN}}$=62 GeV recorded by the STAR experiment at RHIC. Measurements of momentum correlations of particles at small relative velocities are used to extract information about space-time extension of the particle-emitting source at the time of kinetic freeze-out. Non-identical particle measurements are sensitive not only to the size of the system, but also to an emission asymmetry between different particle species. Since this asymmetry may arise from the collective expansion and/or early decoupling of Ξ these measurements of $\pi-\Xi$ correlations provide important test of the dynamics of heavy-ion collisions.

In this work are presented first femtoscopic measurements with multi-strange baryons. In the measured $\pi-\Xi$ correlation function effects of Coulomb and strong interactions were observed with the latter going via $\Xi^*(1530)$ resonance. It is a first observation of this resonance in collisions of heavy nuclei.

The measurements show that in Au+Au collisions at energies $\sqrt{s_{NN}}$=200 GeV and $\sqrt{s_{NN}}$=62 GeV the average emission space-time points of pions and Ξ are are not identical. It is presented that the observed emission asymmetries and source-sizes are in agreement with emission of particles coming from a source in which both the pions and Ξ take part in the collective transverse expansion. This measurement is hence an independent confirmation of a flow of multi-strange baryons in high energy heavy-ion collisions.

Věnováno babičce a dědovi.

Acknowledgments

I would like to express my gratitude towards the STAR Collaboration in which I had the privilege to work with many outstanding scientists and met many good friends.

I want to thank the members of the STAR HBT group for the discussions and comments on my analysis - mainly Mike Lisa, and Zbigniew Chajecki. Above all I offer my sincere gratitude to Dr. Fabrice Retiere who was my mentor for most of the work. Not only his expertise and insight was indispensable for my thesis, but I indeed enjoyed working with Him. I would also like to thank Dr. Lednicky for help and consultations on the theory of femtoscopy.

There are many more friends from the STAR Collaboration whose help on various topics I would like to acknowledge. I especially have to mention two: Jérôme Lauret for his support of Prague's group computing efforts, and Davin Lynn from the SVT group who gave me the chance to learn about and work with silicon drift detectors.

I was lucky to work in great team of coworkers in the Prague's heavy-ions group. I'd like to thank my fellow students Jan Kapitán, Michal Zerola, Michal Bysterský, and Pavel Jakl for their support in either physics or computing related matters, and also for just being good friends.

The greatest acknowledgment is extended towards my supervisor Dr. Šumbera. Without his help and support I would never be where I am today. He introduced me to the beautiful field of heavy-ion physics for which I am very grateful. He oversaw my whole research and always pointed me to the right directions when I needed help while giving me plenty of freedom for my own independent decisions and work. He has created conditions for my work, and work of other students, that are comparable with any world-class research facility.

And finally, I want to thank my family - my parents, grandparents and my little sister. Without your unconditional support this all would not be possible.

Contents

Chapter 1

Strong interaction, quarks, partons and QCD

1.1 Road to quarks and color

Looking back at the history of nuclear and particle physics it is stunning how much have our knowledge and understanding of the basic principles of physics advanced in last hundred years. It was only in 1911 when Ernest Rutherford discovered nucleus by scattering of α-particle off golden foil[1]. Since then followed era of discoveries in this new field that completely reshaped our view of what are the basic building blocks and forces of the universe we live in. The early discovery of proton was followed by the discovery of positron in 1932 by Carl Anderson [2] and neutron by James Chadwick [3] in the same year. Important advance in the theory of nuclear forces was Yukawa's realization of the relation between range of the force mass of the mediating particle and in 1934 showing that short range strong interaction has to be mediated by particle of a mass of approximately 200MeV. Further studies of nuclear binding energies and proton neutron scattering led to a conclusion of a charge independence of the strong interaction by Cassen and Condon [4] and later to the introduction of an internal quantum number of "isospin" by Heisenberg. The concept of the particle-mediated strong force invariant under transformation in the isospin space paved the way to unitary symmetry, quark model and eventually Quantum Chromodynamics.

Multitude of new particles were discovered in the mid of the 20^{th} century. The experiments shown that certain particles, such as the kaons or certain hyperons (at that time called $V_1^{0,+}, V_2^{0,+,-}$), were created easily in particle collisions, but decayed much more slowly than expected from their large masses and large production cross sections. It was also observed that these particles are always produced in pairs. To resolve this a concept of new quantum number called "strangeness" was introduced by Kazuhiko Nishijima and Murray Gell-Mann. The property of strangeness is that it is conserved during strong and electromagnetic inter-

actions, but not in the weak interactions. Based on the similarities of the already known particles and the concept of underlying $SU(3)$ flavor symmetry existence of new particles Σ^0, and Ξ^0 was predicted in 1955 by Gell-Mann. The two particles were found soon after in 1956 and 1959. In the following years discoveries of resonances from vector meson octet as well as from spin 3/2 baryon decuplet were made. Observation of $\Xi^*(1530)$ (which is a particle of main interest for this thesis) and Ξ^{*0} was announced in 1962 and led to immediate prediction, made by Gell- Mann and Ne'eman, of not yet discovered iso-singlet Ω^-. Its discovery in 1964 was a confirmation of $SU(3)$ flavor symmetry called by Gell-Mann the Eightfold Way [5, 6] Even before the discovery of Ω^- two papers, one from Zweig [7] and one from Gell-Mann [8], laid out basics of what is known as additive quark model. In the quark model the structure of the groups could be explained by the existence of three fundamental particles of three flavors that the hadrons are made of. However some key problems still remained. A Δ^{++} resonance in the baryon decuplet has spin of 3/2 and in the the quark model is composed of three identical up quarks with parallel spins. The quarks are fermions and they should follow the Pauli exclusion principle thus fully symmetric state would not be possible. The problem was resolved in 1965 independently by Yoichiro Nambu with Moo-Young Han and W. Greenberg by assigning quark additional inner $SU(3)$ gauge degree of freedom that was later given name color charge. Deep inelastic scattering (DIS) of electrons on protons at SLAC showed that the originally purely mathematical concept of quark model has connection with reality and protons are indeed composite objects made of partons.

Hand in hand with experimental discoveries theoretical description of the strong interaction was developed. The Quantum Chromodynamics (QCD) is at present generally accepted description of the strong interaction. QCD is a quantum field theory belonging to a class of non-abelian gauge theories. The central idea of gauge theories is an invariance of the system under transformations of internal degrees of freedom. The corresponding gauge symmetry group then plays crucial role in determining the dynamics of the theory. The concept of gauge invariance has been around for about ninety years but only later on with the success of QCD it has been recognized as the principle governing fundamental forces between elementary particles. It is of a historical interest that a first idea of gauge invariance came already in 1919 from Hermann Weyl [9]. Initially he tried to derive classical electrodynamics from local scale ("gauge") invariance. This effort failed but the same principle was successfully used later in for Quantum Electrodynamics(QED). In the case of QED the gauge transformation is not of measurable variable, but of an interval one - the phase of particle wave function. The symmetry associated with phase is that of global $U(1)$ symmetry group. However this initial success was overlooked for about 50 years mainly due to the fact that the QED was already derived and the gauge invariance was seen merely as coincidental symmetry not a driving principle of dynamics of the theory. Next step toward successful gauge theory of the strong interaction was made in 1954 by Robert Mills and Chen Ning Yang [10] in which they

tried to derive the strong interaction base on $SU(2)$ isotopic-spin gauge invariance based on previous suggestion of proton and neutron differing only in iso-spin projection. Even thought this attempt yielded theory with massless force mediators (thus long range interactions), it meant that the previous idea of Weyl was extended from abelian $SU(1)$ group to nonabelian symmetry groups. This has a profound consequences since in these, now called Yang-Mills theories, the vector fields are self-coupled as a direct result of the noncomutativity of the non-abelian gauge symmetry group. In the 1960's and 1970's, this principle was successfully used to unify electric and weak interaction into the Weinberg-Salam-Glashow electroweak theory [11] with $SU(2)\times U(1)$-invariant Lagrangian. The masslessness of classical Yang-Mills fields was avoided by elaborating the theory with an additional "Higgs field". A further attempt(before the prediction of color) to describe the strong interaction by gauge field theory was done by Yval Ne'eman in 1961 in [12]. This theory was derived based on $SU(3)$ flavor symmetry where the nowadays role of color charge was played by flavor quantum number and role of self-interaction force-mediators field was played by eight vector mesons. With the success of quark model in describing the large amount of hadrons and introduction of color it has become evident that quarks, rather then meson or nucleons are the sources of the strong interaction and the role of the relevant internal quantum number is played by color.

generation	quark	flavor	mass[MeV]	J	B	Q	I_z
First	u	up	1.3-3.0	$\frac{1}{2}$	$\frac{1}{3}$	$\frac{2}{3}$	$\frac{1}{2}$
	d	down	3-7	$\frac{1}{2}$	$\frac{1}{3}$	$-\frac{1}{3}$	$-\frac{1}{2}$
Second	c	charm	1250±90	$\frac{1}{2}$	$\frac{1}{3}$	$\frac{2}{3}$	$\frac{1}{2}$
	s	strange	95±25	$\frac{1}{2}$	$\frac{1}{3}$	$-\frac{1}{3}$	$-\frac{1}{2}$
Third	t	bottom	174200±3300	$\frac{1}{2}$	$\frac{1}{3}$	$\frac{2}{3}$	$\frac{1}{2}$
	b	top	4200±70	$\frac{1}{2}$	$\frac{1}{3}$	$-\frac{1}{3}$	$-\frac{1}{2}$

Table 1.1: The main quark properties J-spin, B-baryon number, Q-electric charge, I_z-isospin. Mass taken from [13].

Therefore in the Quantum Chromodynamics (QCD), the theory we believe that describes well the strong interaction the main constituents are six quarks. These are massive 1/2-spin fermion fields described by Dirac bispinors ψ_f carrying flavor quantum number f which is conserved in the strong interaction. Their main properties are listed in Table 1.1.

1.2 QCD Lagrangian

The dynamics of the non-interacting quarks is described by simple Lagrangian:

$$\mathcal{L} = \overline{\psi}_f(i\gamma^\mu\partial_\mu - m_f)\psi_f, \tag{1.1}$$

where f denotes flavor of the quark, and with accordance with Einstein notation summing over repeating indexes is performed. As stated above the dynamics of the system is can be derived from invariance of the Lagrangian under local $SU(3)$ transformations in the space of inner color quantum number. This means that the quarks of every flavor are postulated to be in 3-dimensional color space and transform in it as a vector and antiquarks as co-vector:

$$\psi(x) = \begin{pmatrix} \psi_r(x) \\ \psi_g(x) \\ \psi_b(x) \end{pmatrix}, \overline{\psi}(x) = \begin{pmatrix} \overline{\psi}_r(x) & \overline{\psi}_g(x) & \overline{\psi}_b(x) \end{pmatrix}, \tag{1.2}$$

where subscripts r,g,b denote the three color charges(red, green, blue). The unitary transformation $U \in SU(3)$ ($UU^\dagger = 1$, $|U| = 1$)then transforms

$$\psi(x) \to U\psi(x) \qquad \overline{\psi}(x) \to \overline{\psi}(x)U^\dagger. \tag{1.3}$$

Without an incursion into group theory, the unitary operator U can be rewritten as:

$$U = \exp\left(i \sum_a \theta_a T_a\right), \tag{1.4}$$

where θ_a are real numbers and T_a are called the generators of the group. For unitary group the generators are hermitian operators. The symmetry being local means that the operator U changes smoothly as a function of space-time coordinates, $U = U(x)$, and therefore coefficients θ_a depend on the coordinates as well: $\theta_a = \theta_a(x)$. In the case of $SU(3)$ group there are eight generators T_a. They can be chosen in an arbitrary way, the simplest and most common choice are using traceless Gell-Mann matrices:

$$\begin{gathered} \lambda_1 = \begin{pmatrix} 0 & 1 & 0 \\ 1 & 0 & 0 \\ 0 & 0 & 0 \end{pmatrix} \lambda_2 = \begin{pmatrix} 0 & \text{-i} & 0 \\ \text{i} & 0 & 0 \\ 0 & 0 & 0 \end{pmatrix} \lambda_3 = \begin{pmatrix} 1 & 0 & 0 \\ 0 & \text{-1} & 0 \\ 0 & 0 & 0 \end{pmatrix} \lambda_4 = \begin{pmatrix} 0 & 0 & 1 \\ 0 & 0 & 0 \\ 1 & 0 & 0 \end{pmatrix} \\ \lambda_5 = \begin{pmatrix} 0 & 0 & \text{-i} \\ 0 & 0 & 0 \\ \text{i} & 0 & 0 \end{pmatrix} \lambda_6 = \begin{pmatrix} 0 & 0 & 0 \\ 0 & 0 & 1 \\ 0 & 1 & 0 \end{pmatrix} \lambda_7 = \begin{pmatrix} 0 & 0 & 0 \\ 0 & 0 & \text{-i} \\ 0 & \text{i} & 0 \end{pmatrix} \lambda_8 = \frac{1}{\sqrt{3}} \begin{pmatrix} 1 & 0 & 0 \\ 0 & 1 & 0 \\ 0 & 0 & \text{-2} \end{pmatrix}. \end{gathered} \tag{1.5}$$

In therms of these matrices the generators are $T_a \equiv \frac{\lambda_a}{2}$. The non-interacting Lagrangian (1.1)

is not invariant under transformation (1.3):

$$\begin{aligned}\mathcal{L}' &= \left(\overline{\psi}U^\dagger\right)\left(i\gamma^\mu\partial_\mu - m\right)(U\psi) \\ &= \overline{\psi}U^\dagger\left[i\gamma^\mu(\partial_\mu U)\psi + iU\gamma^\mu(\partial_\mu\psi) - mU\psi\right] \\ &= \overline{\psi}\left(i\gamma^\mu\partial_\mu - m\right)\psi + i\overline{\psi}\gamma^\mu(\partial_\mu U)\psi,\end{aligned} \tag{1.6}$$

where the summation over flavor was omitted. It can be seen that the last term vanishes only if U is independent of the space-time coordinate x_μ. The principle of obtaining obtaining dynamics of the system from gauge invariance means to recover the gauge invariance of the (1.6) by introduction of vector field $A_\mu(x)$ into the Lagrangian with a proper interaction term that cancels under the transformation the last term of (1.6). The simplest such Lagrangian can be written as:

$$\mathcal{L} = \overline{\psi}(i\gamma^\mu\partial_\mu - m)\psi - \frac{1}{4}F^a_{\mu\nu}F^{a\,\mu\nu} + g\overline{\psi}\gamma^\mu\psi A_\mu, \tag{1.7}$$

where vector field $A_\mu \equiv A^a_\mu T^a$ describes eight gluons. Thus arranging quarks into triplet (1.2) with $SU(3)$ transformation (1.4) directly requires eight vector fields. The $F_{\mu\nu}$ is the corresponding field strength tensor and g regulates the strength of the interaction. In order for the interaction term of (1.7) to cancel out the last term of (1.6) the vector field has to transform as

$$A_\mu \to UA_\mu U^\dagger - \frac{i}{g}(\partial_\mu U)U^\dagger. \tag{1.8}$$

Very important property of the QCD, arising from choosing non-commutative $SU(3)$ group is revealed when looking at the kinetic term for the vector field $F^a_{\mu\nu}F^{\mu\nu}_a$. The non-commutativity of the vector field operators render the kinetic term with QED-like

$$G^{QED}_{\mu\nu} = \partial_\mu A_\nu - \partial_\nu A_\mu \tag{1.9}$$

non-invariant. The gauge invariance recovered by introducing additional term:

$$F^a_{\mu\nu} \equiv \partial_\mu A^a_\nu - \partial_\nu A^a_\mu + gf^{abc}A^a_\mu A^b_\nu, \tag{1.10}$$

where coefficients f^{abc} are the structure constants fulfilling the commutation relations of the $SU(3)$ generators

$$[T_a, T_b] = if^{abc}T_c. \tag{1.11}$$

This additional term gives a rise to a self-interactions of the vector field(gluons) via kinetic

term, as it unfold into:

$$\begin{aligned} F^a_{\mu\nu}F^{a\,\mu\nu} =& (\partial_\mu A^a_\nu - \partial_\nu A^a_\mu)^2 \\ &+ g f^{abc}\left[\left(\partial_\mu A^a_\nu - \partial_\nu A^a_\mu\right) A^{b\,\mu} A^{c\,\nu} + \left(\partial^\mu A^{a\,\nu} - \partial^\nu A^{a\,\mu}\right) A^b_\mu A^c_\nu\right] \\ &+ g^2 f^{abc} f^{ade} A^a_\mu A^b_\nu A^{d\,\mu} A^{e\,\nu}. \end{aligned} \tag{1.12}$$

The second and third term describe three and four gluon interaction. Thus as a consequence of chosen non-abelian symmetry we have acquired eight gluon fields that can interact with each via its color charge. In QCD we thus have three interaction vertexes:

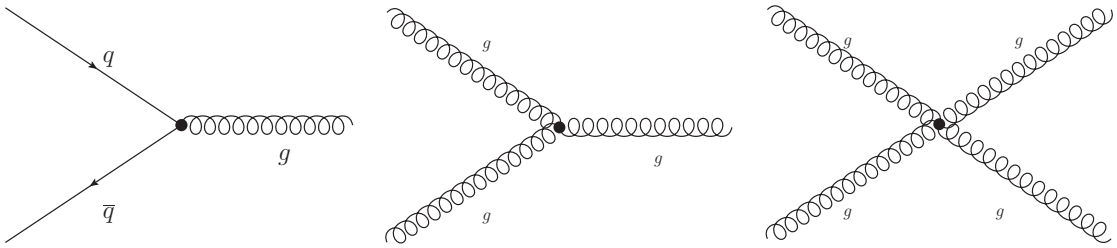

1.3 Asymptotic freedom

Similar to QED, the propagator of non-interacting gluon is proportional to $1/q^2$ which leads to quark-quark potential of the shape of $\sim 1/r$. The profound consequence of the gluon self-interaction terms is revealed when we study how the interaction, ie. the effective coupling constant $g^2(q^2)$, changes as function of the transferred 4-momentum q^2 when higher order quantum correction are considered. With the aid regularization and renormalization the effective coupling constant is expressed as

$$g^2(q^2) = \frac{g^2(\mu^2)}{1 - [\Pi(q^2) - \Pi(\mu^2)]}, \tag{1.13}$$

where μ is a scale parameter(the momentum transfer at which the coupling constant is measured) that enters trough the renormalization process. The $\Pi(q^2)$ comes from the 'vacuum polarization' tensor

$$\Pi^{\mu\nu}(k) = (g^{\mu\nu}k^2 - k^\mu k^\nu)\Pi(k^2). \tag{1.14}$$

which describes response of the vacuum to a charge placed into it. In the leading order perturbation QCD:

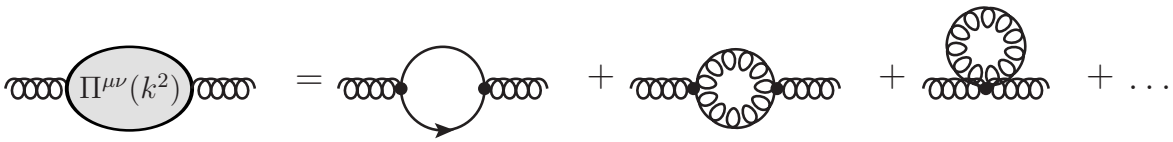

(1.15)

When performing such calculation , which is out of a scope of this work, one can see that terms coming from gluon loops are added with opposite sigh that those coming from fermion loop. This can be intuitively understood in the terms of screening and anti-screening of the color charge. The diagram of 1.15 can be summed in general Yang-Mill theory with N colors and n light flavors . In the leading order the coupling constant 1.13 will then be

$$g^2(q^2) = \frac{g^2(\mu^2)}{1 + \frac{g^2(\mu^2)}{(4\pi)^2}\left(\frac{11}{3}N - \frac{2}{3}n\right)\ln\left(\frac{q^2}{\mu^2}\right)} \tag{1.16}$$

In the QED the conventional electric charge is defined at low momentum transfer $\mu^2 \to 0$. with the structure constant $\alpha = g^2(\mu^2 \to 0)/4\pi \approx 1/137$. In QED case ($N = 0$ and $n = 1$) there are no color fields and only one electron with mass m_e. Thus 1.16 takes form of

$$g^2_{\mathrm{QED}}(q^2) = \frac{4\pi\alpha}{1 - \frac{2}{3}\frac{\alpha}{4\pi}\ln\left(\frac{q^2}{m_e^2}\right)}. \tag{1.17}$$

showing the effective coupling increases with energy transfer. In the QCD with $N = 3$ colors and $n = 3$ light quarks the situation is dramatically different as 1.16 gives

$$g^2_{\mathrm{QCD}}(q^2) = \frac{g^2(\Lambda^2)}{1 + 9\frac{g^2(\Lambda^2)}{(4\pi)^2}\ln\left(\frac{q^2}{\Lambda^2}\right)}. \tag{1.18}$$

where λ is a dimensional parameter introduced again by the renormalization process. Compared to previous case the g^2 decreases with increasing momentum transfer. This behavior is called *asymptotic freedom*. Therefore applicability of perturbative calculations in QCD is limited to high momentum transfers. A typical scale for measurements and calculations of the strong coupling constant $\alpha_S(q^2) = g^2(q^2)/4\pi$ is at the mass of the Z^0 boson at $M_{Z^0} = 91.2\mathrm{GeV}/c^2$. The current world average is $\alpha_S(M_{Z^0}) = 0.1189 \pm 0.0010$ [14].

Although all of the information about strong interaction is contained in the fundamental QCD Lagrangian 1.4 we are not able to extract information from it according to our wishes as the mathematical techniques of non-perturbative calculation are not yet developed enough. We thus have to rely on effective theories and lattice calculation to learn about QCD vacuum properties, quark confinement and chiral symmetry breaking.

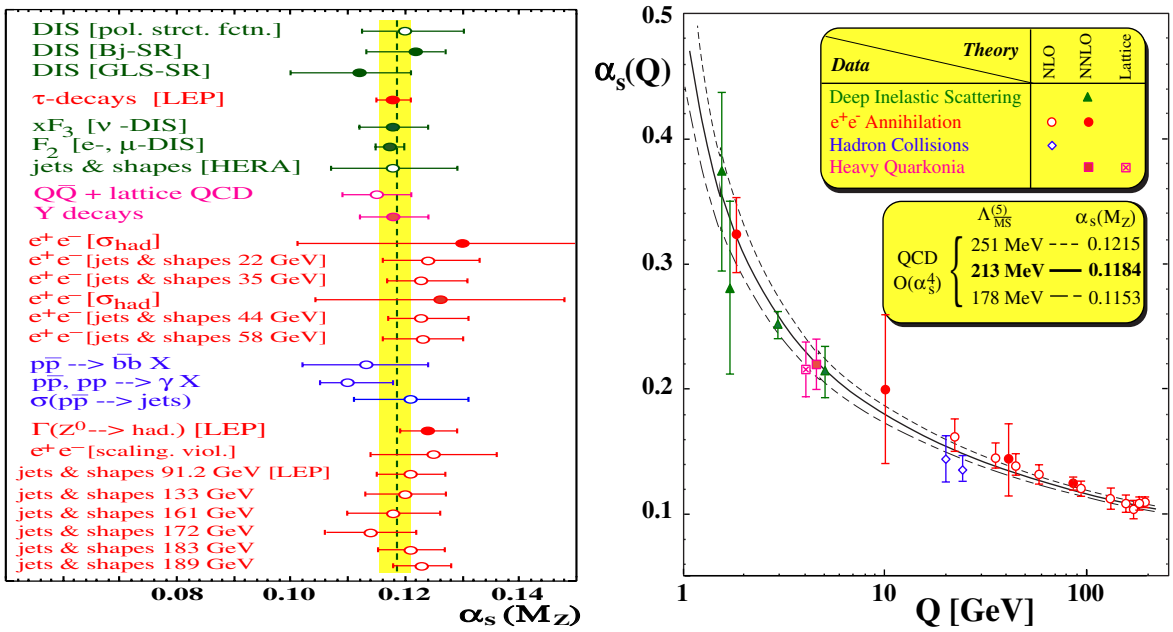

Figure 1.1: Left: Summary of $\alpha_s(M_Z)$ Right: The running coupling constant as a function of momentum transfer Q^2 determined from different processes. Figures taken from [15, 14]

1.4 QCD vacuum at zero and finite temperature

1.4.1 Confinement

Important property of strongly interacting particles is a *color confinement* [16], the absence of hadronic states other than color singlets. In a nature we are thus unable to isolate and directly observe any colored particle, quarks, gluon or any colored combination. There is not a complete proof and understanding of the confinement, however rather solid and consistent picture can be drawn from the above mentioned properties of running coupling constant and lattice calculations.

The property of asymptotic freedom means that as the coupling constant $\alpha_s \to 0$ the gluon propagator will behave as free propagator proportional $\sim 1/q^2$. This means that in the high energy limit, ie. at small distances, the inter quark potential will be similarly as in QED of the form $\sim 1/r$. However at large distances the inter quark potential does not vanish as in the QED case, but since the gluons are color-charged they spread the color and effective color charge seen by the two quarks increase. The inter quark potential then increases as well. At a certain distance when the potential energy of the pair becomes high it is more energetically convenient to create $q\bar{q}$ pair out of vacuum and create two bound states instead.

This picture is supported by lattice calculations of inter quarks potential between static, infinitely heavy, quarks. In the lattice calculation the space-time continuum is discretized

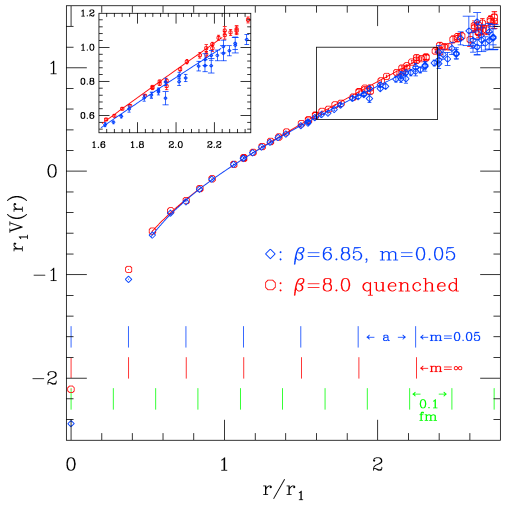

Figure 1.2: The heavy quark effective potential calculated with three flavor QCD. Vertical bars show the scale of the lattice spacing a, and intervals in physical units 0.1 fm wide for reference. Figure taken from [17].

into lattice points and QCD action, based on Feynmann path integral, is calculated between the individual points. The numerical calculation with static quarks of three flavors [17] shows, as seen in Figure 1.2, that in the non-perturbative regime the potential increases linearly with r. The slope of the linear rise is usually called the *string constant*, since it can be thought of as the tension of a spring.

1.4.2 High density and finite temperature

The above calculations considered behavior of color charge and strong force in the QCD vacuum, which results in the confinement of quarks inside hadrons. However the properties of the strong force intuitively suggest that a state of matter in which the long-distance confining force is wekened so that colored particles can travel across distance larger then size of hadron, may exist under certain conditions. This deconfined phase called *Quark-Gluon Plasma*(QGP) [18, 19] behavior of which would be driven by degrees of freedom of quarks and gluons instead of hadrons could be created in two distinct ways:

The first way is low temperature ($T = 0$) large baryon density matter. At certain critical baryon density ρ_c the baryons start to overlap. The quark will interact at short distances and the matter will dissolve into degenerate quark matter. Such a matter would have high net-baryon density $n_q \gg n_{\bar{q}}$ and is assumed to exist in universe in such a places such as cores of neutron stars.

The second way is to create hadronic matter of high temperature (and low baryon density). To study the behavior of hadronic matter at high temperature the tools of finite

temperature field theory [20, 21] have to be used. In the framework of finite temperature field theory particle propagators and vacuum polarization tensor $\Pi^{\mu\nu}$ of 1.15 can be calculated. Indeed calculation from lattice QCD suggest that as the temperature increases the effective inter-quark potential is modified. As shown in the Figure 1.3, in the vicinity of the critical temperature T_c the linear part of the potential, responsible for quark confinement, is weakened. Consequently, nuclear matter heated above the critical temperature should not exhibit confinement.

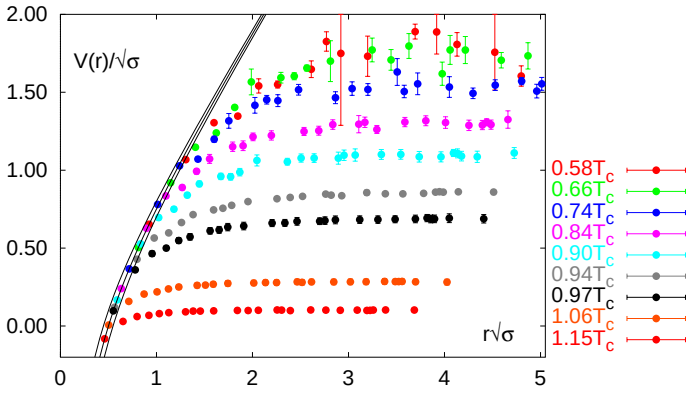

Figure 1.3: Temperature dependence of the heavy quark potential for three flavor QCD in the vicinity of critical temperature T_c. Values are scaled by string tension $\sqrt{\sigma}$ obtained at zero temperature. Figure from [22].

The latter case of the high temperature QGP is believed to resemble a matter that existed in the early stages of the universe and may possibly be recreated in the high energy nuclear collisions.

1.5 Phase transition in QCD

In the previous text it was advocated that for hadronic matter which is described at the most fundamental level by QCD there exists a phase transition from confined hadronic matter into deconfined QGP phase. To study such a phase transition is of a high importance for modern nuclear physics and well as astrophysics. It is believed that deconfined QGP phase existed in the early universe shortly after the Big-bang ($t \sim 10^{-6}s$) and as the universe cooled down it uderwent a phase transition similar to that that we hope to recreate in the heavy-ion collisions. It's therefore of interest to study, both theoretically and experimentally, nuclear matter at high temperature with aim to create deconfined phase governed by partonic degrees of freedom and study the phase transition. The experimental access to information about such deconfined is essential as even the most fundamental questions are not easily answered from the first principle calculations, such as: At what temperature does the phase transition occur? What is the nature if the phase transition, is it first or second order phase transition

or is it a crossover? To what degree can we create a thermally equilibrated partonic matter in the heavy ion collisions?

1.5.1 The bag model of hadrons

Event thought the perturbative QCD cannot describe the behavior of the confined quarks, there are some phenomenological models that can give a relevant description. One of the simplest, though illustrative models is the "MIT bag model" [23, 24] in which the long distance non-perturbative behavior is replaced by a vacuum pressure acting on the hadron. Confinement of the quarks is then the result of the balance between the inward pressure of the bag and the outward pressure arising from non-zero kinetic energy of the quarks inside.

The hadrons are considered to be made of massless quarks which are allowed to move freely inside a bag of a finite dimension,and are infinitely massive outside of the bag. Finding relation between size R of the bag and energy E of the quarks corresponds to solving Dirac equation and require that the scalar fermion density vanishes at the distance of R[19, 25]. The solution yields eigenvalues for ER:

$$ER = \omega_q \approx\ 2.043,\ 5.396,\ 8.578, \ldots. \tag{1.19}$$

The non-perturbative effects of QCD which bound the quarks in the hadron are substituted by a phenomenological bag pressure B. The total energy(mass) of the hadron E_H then comes from two terms: the energy associated with the volume due to the external pressure and kinetic energy of the quarks inside[25]:

$$E_H = \frac{4\pi}{3} R^3 B + \sum_q \frac{\omega_q}{R}, \tag{1.20}$$

where q runs over quark content of the hadron.

Equilibrium between the external pressure of the vacuum and internal pressure due to the kinetic energy of the quarks is reached when $dE/dR = 0$. In case of $\sum_q \omega_q \to N_q \omega_q$ the radius of the hadron R is related to the vacuum pressure B by

$$R^4 = \frac{N_q \omega_q}{4\pi B}. \tag{1.21}$$

The actual value of the bag constant can be obtained from fits of mass spectra of light hadrons. In literature the found value ranges $145MeV < B^{1/4} < 235MeV$ [26, 18, 19, 24, 23].

This model allows for a simple explanation of the phase transition from the normal hadronic matter, with the quarks confined in the hadrons, to the deconfined phase. It can be seen that if the pressure exerted from the quarks inside rises, there will be a point when the pressure from inside exceeds the pressure of the bag. At this point the bag pressure will

not be able anymore to hold the quarks inside of the hadron. The quarks and gluons will then undergo a phase transition from the confined to the *deconfined state*.

The thermodynamical properties of a gas of non-interacting quarks and gluons can be calculated using grand-canonical partition function

$$\ln\mathcal{Z} = V \sum_{i}^{particles} (\pm) g_i \int \frac{d^3p}{(2\pi)^3} \ln\left(1 \pm e^{-(E(p)-\mu)/T}\right), \tag{1.22}$$

where + in ± applies to fermions and − to bosons, μ is baryo-chemical potential, and g_i stands for degeneracy factors of each particle. The evaluation[26] of 1.22 gives pressure for gas of gluons

$$P_G = T\left(\frac{\partial \ln\mathcal{Z}}{\partial V}\right)_{\mu,T} = g_G \frac{\pi^2}{90} T^4, \tag{1.23}$$

and similarly for gas of massless quarks and antiquarks

$$P_Q \approx g_Q \frac{T^4}{12}\left[\frac{7\pi^2}{30} + \left(\frac{\mu}{T}\right)^2 + \frac{1}{2\pi^2}\left(\frac{\mu}{T}\right)^4\right]. \tag{1.24}$$

The degeneracy factor of gluon is

$$g_G = 8(colors) \times 2(polarizations) = 16. \tag{1.25}$$

If we consider only two light quarks (up,down) the quark degeneracy factor is

$$g_Q = 3(colors) \times 2(spin\ states) \times 2(flavors) = 12. \tag{1.26}$$

We get from 1.23-1.26 the pressure exerted by the QGP gas, which at the point of phase transition, at a critical temperature T_c, is equal to the bag pressure B

$$\begin{aligned} B &= P_{QGP} = P_Q + P_G \\ &= T_c^4\left[\frac{37\pi^2}{90} + \left(\frac{\mu}{T_c}\right)^2 + \frac{1}{2\pi^2}\left(\frac{\mu}{T_c}\right)^4\right]. \end{aligned} \tag{1.27}$$

Any of these conditions (high T or high μ) by itself, or their combination, should be sufficient to create the deconfined phase of the quarks and gluons.

1.5.2 Phase Transition in Lattice QCD

The running coupling constant 1.18 shows that at high momentum transfers the perturbative approach is applicable for calculations in zero temperature QCD. Similarly the asymptotic freedom may be expected at sufficiently high temperature. However, it is questionable

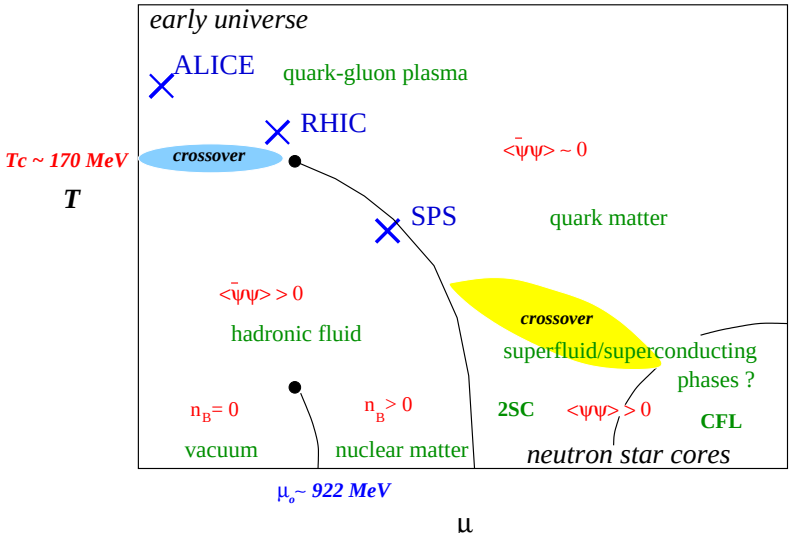

Figure 1.4: The QCD phase diagram [27] in the temperature-chemical potential plane. The solid lines depict region of expected first-order transition.

whether perturbation approach in the framework of finite temperature field theory[20] is applicable at the vicinity of the QGP phase transition that is within a reach of the heavy-ions experiments.

Calculation of the thermodynamic partition function were performed in terms of perturbative series in the powers of coupling constant up to order $\alpha_s^{5/2}$ [32, 33]. These calculations do not lead to convergent results for range of temperatures that are of interest to us, as they oscillate strongly with the order of expansion(Figure 1.5). The perturbative calculation become reliable only for $\alpha_S < 0.01$ which corresponds to temperatures of the order $T > O(10^2)$GeV. Although advancements in perturbation calculations[28, 31] indicate that improved perturbative methods may work already at temperatures that are only a few times ($\sim 4T_c$) higher than the deconfinement transition temperature(Figure 1.6) it is still out of experimental reach.

For the above reasons the so far most successful theoretical tool based on first principles calculations which gives quantitative prediction in the vicinity of the QGP phase transition remains the lattice approach to finite temperature QCD[34, 29, 27, 35]. The lattice calculation can be used to study multitude of properties of high-temperature QCD matter such as energy density, pressure, chiral condensate, viscosity, screening lengths of color charges, and equation of state.

The results of lattice calculations indeed suggest that the QCD-matter exhibits a phase transition[35, 36]. The most common quantity taken as an order parameter for the phase transition on the lattice is the value of Polyakov loop[37], which is related to a free energy of a static quark. In a pure $SU(3)_C$ gauge theory(with gluons only) the value of Polyakov

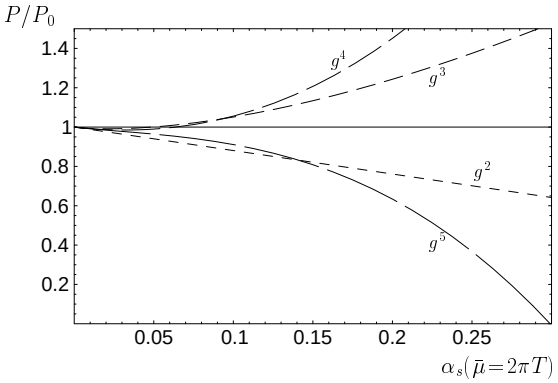

Figure 1.5: Perturbative calculations of the thermal pressure of pure glue QCD normalized to the ideal-gas value as a function of $\alpha_s(\bar{\mu} = 2\pi T)$.Figure adopted from [28].

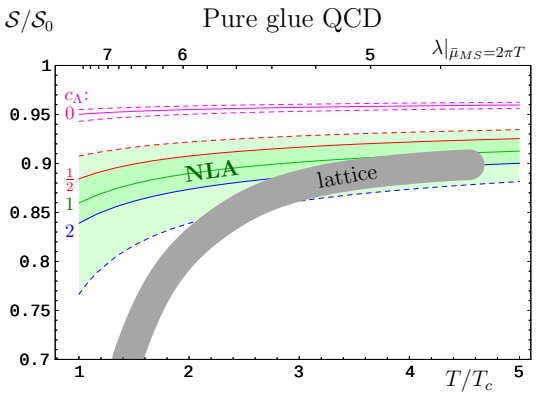

Figure 1.6: Comparison of calculation of entropy density of pure glue QCD using lattice QCD[29] and perturbation series. The calculated values are divided by Stefan-Boltzmann value [30].Figure adopted from [31].

loop is zero at low temperature and nonzero at high temperature. This phase transition indicated by the Polyakov loop, as shown in the Figure 1.7, is in the lattice calculations also accompanied by a change in the chiral condensate $\langle\overline{\psi}\psi\rangle$ which is and order parameter for chiral-symmetry restoration phase transition. The properties of the actual phase transition, even in the case of vanishing baryo-chemical potential, strongly depend on the number of considered dynamic quark flavors and their masses. In the case of pure $SU(3)$ gauge theory the critical temperature T_c is know to be $\approx$ 270MeV[29]. However when light dynamical quarks are included the calculations the T_c lowers to vicinity of 160MeV[38, 35]. As shown in Figures 1.8a and 1.8b the pressure and energy density quickly rise above the critical temperature. This change corresponds to sudden increase in the degrees of freedom available to thermal excitations(1.25 and 1.26). The values saturate at about $2T_c$, but not reaching the Stefan-Boltzmann limit for ideal gas even at $4T_c$, which is a sign that event at such a high temperature some remaining long distance interaction is still present.

Not only the critical temperature, but also the type of the phase transition itself depends on the number dynamical quarks and their masses [36, 35]. Latest advances in lattice calculation allow to extrapolate into region of non-zero chemical potential[39, 27, 40] and explore the (μ, T) phase diagram[41]. While for vanishing chemical potential the phase transition is expected to be of first or second order [42, 36], the calculations with non-zero chemical potential predict most likely a crossover type of transition. There is a possibility of existence of a critical point in the phase diagram[43, 44] . The search for such a critical point will be an important part of the program of heavy-ion physics in the near future.

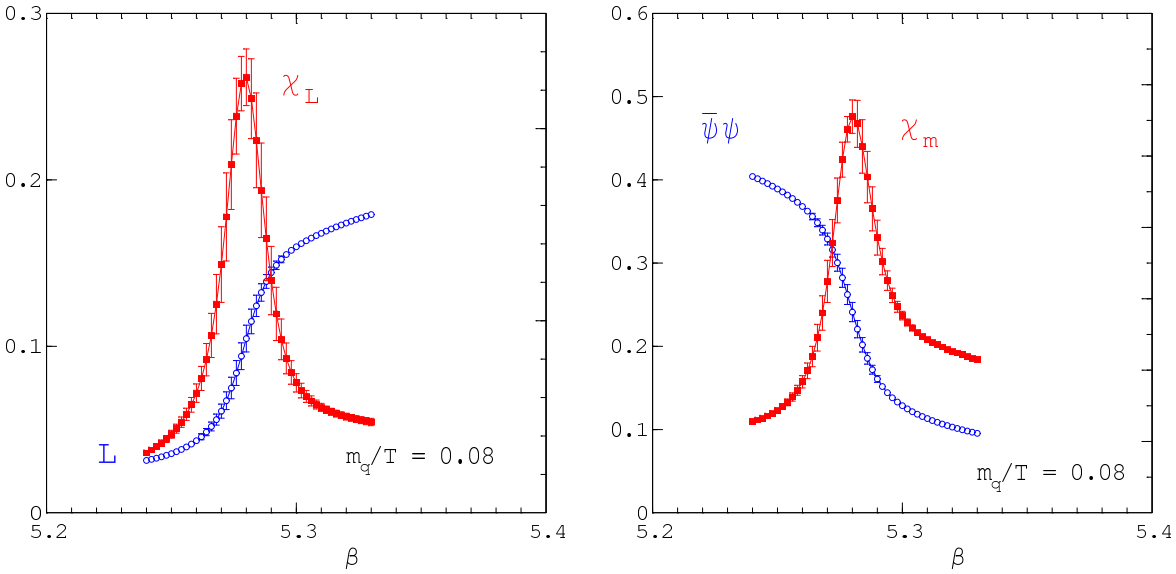

Figure 1.7: Lattice calculations in 2-flavor QCD showing deconfinement(left: $\langle L \rangle$-Polyakov loop expectation value) accompanied by chiral symmetry restoration (right: $\langle \bar{\psi}\psi \rangle$ -chiral condensate). β is a bare coupling strength used in the calculations. Increase of β corresponds to decreasing lattice spacing and increasing temperature. Figure from [35].

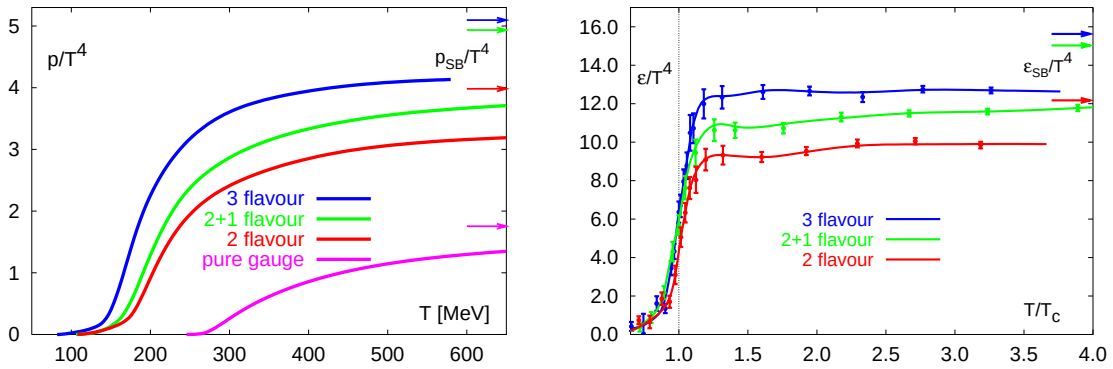

Figure 1.8: pressure (left) and energy density(right) in lattice QCD[35] divided by T^4. The calculations are done for different number of light quarks. The curve labeled (2+1)-flavor corresponds to a calculation with two light and a four times heavier strange quark mass. The arrows show values expected for the limiting case of ideal gas.

Chapter 2

Heavy Ion collisions

The collisions of heavy ions at high energies is a way to create and study hot and dense nuclear matter experimentally in the laboratory. When two heavy ions collide, part of their initial kinetic energy is deposited in the collision region and cause excitation of the QCD vacuum. If the energy density is high and the life time of the system long enough the created matter may undergo the phase transition to quark gluon plasma. We expect that by analyzing the final products of the collisions we will be able to tell not only whether the QGP was created, but also to study the properties of this new phase of matter and it's phase transition. In this chapter is presented brief and simplified overview of our current understanding of the heavy-ion collisions - it's evolution and subset of observables and results that are relevant to the topic of this thesis.

2.1 Collision evolution

Compared to the "ordinary" scattering experiments conducted with elementary particles the unique aspect of the collisions of heavy ions are the typical time and space scales involved. In the collisions of nuclei the created system undergoes non trivial evolution that in the case of central events spans over scales of the order $\sim 10 - 20$ fm in time and space.

A schematic drawing of space-time evolution of the collision of the heavy ions is shown in Figure 2.1. The evolution comprises of multiple stages each of which can be described by different driving physics principle and influences different observables. Different measurements in the final state are thus sensitive to different stages of the collisions. In order to assess whether the QGP phase was created it is necessary to understand the whole evolution of the heavy ions collisions including initial conditions and final hadronization.

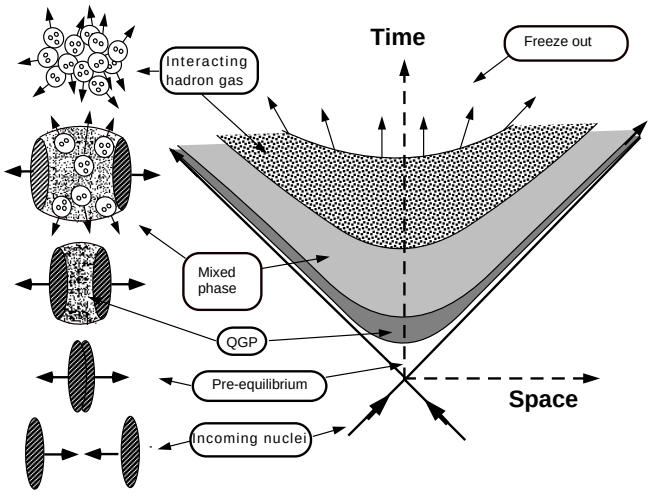

Figure 2.1: Schematic diagram of time-space evolution of the heavy ion collisions with depicted main stages. Figure from [45].

2.1.1 Initial geometry and preequilibrium

As in every experiment, control over initial conditions is crucial for interpretation of final results. If the size of the system in the most central collisions leads to creation of a matter with significantly different behavior, such as QGP, we can study the onset of such physics by varying centrality as naturally the physics of the most peripheral collisions has to be close to proton-proton collisions.

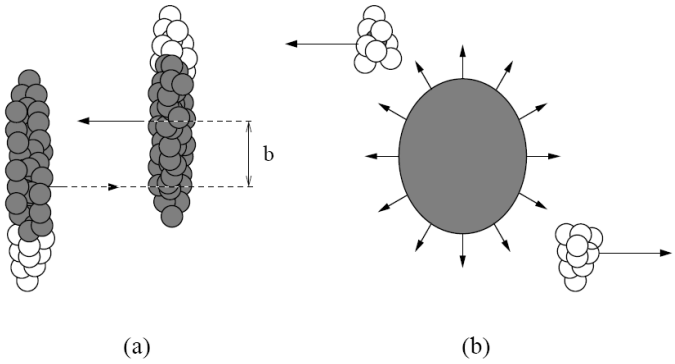

Figure 2.2: Two nuclei colliding with impact parameter b. The overlap region with *participants* is shown in dark while non-interaction *spectators* are in white. Figure from [46].

The properties and evolution of the system is largely determined by initial geometry given by the centrality of the collision. When two nuclei collide the nucleons in the region of the interacting overlap, as shown in the Figure 2.2, are called "participants" while remaining non-interacting nucleons are called "spectators". During the initial stage of the collision part of the energy of incoming nuclei is deposited and large amount of entropy is produced.

The mechanism of the parton production at early stage is not well understood at this point. Multiple models that describe this pre-equilibrium phase exist that connect the geometry of the collision with initial energy and baryon distribution. Although there exist other models, such as pQCD mini-jet production, two most common approaches to the initial stage are the Glauber model[47, 48] of incoherent parton scattering and Color Glass Condensate(CGC) saturation model[49, 50, 51].

Glauber model

Glauber model[47, 48] treats semi-classically nucleus-nucleus collision as multiple nucleon-nucleon interactions. It is used to relate the impact parameter b to other variables which quantify the collision centrality, such as the number of participant N_{part}, and number of binary collisions N_{coll}. In the Glauber model the initial particle production is controlled by combination of N_{part} and N_{coll} distributions. It is assumed that hard pQCD processes occur at the very early times of the collision and scale with binary collisions N_{coll}, while soft non-perturbative processes depend on the volume of the system thus scale with N_{part}. The centrality of the collision can be determined either directly by detecting the remaining spectators or indirectly by measurements of observables depending on the volume of the system and hence centrality such as final multiplicity.

Color Glass Condensate

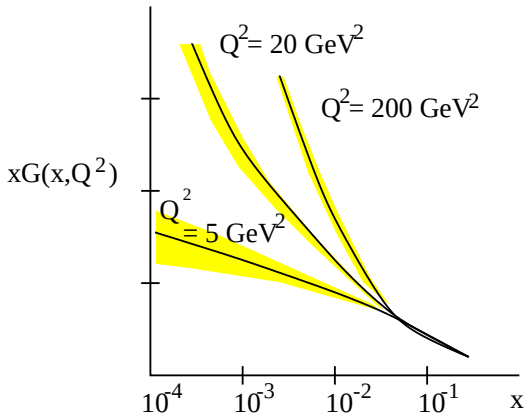

Figure 2.3: Gluon distribution as a function of x as measured by HERA experiment[52, 53]. Figure from [54].

Another way of describing initial stage of nucleus-nucleus collisions is based on Color Glass Condensate model and Glasma[49, 50, 51, 54]. As measured by deep inelastic scattering experiments the number of sea quarks and gluons which carry a certain momentum fraction x of the nucleus increases with decreasing x and increasing momentum transfer Q^2(Figure 2.3).

The typical momentum of theses partons is on the order of $\Lambda_{QCD} \sim 200$ MeV. From uncertainty principle their longitudinal size is $1/p \sim 1$ fm, while the wave function of valence quarks is contained within $\sim 2R/\gamma$. Therefore in ultra-relativistic collision where $\gamma > \frac{2R}{1fm}$ the low-x partons, namely gluons, will play dominant role. However the increase of the number of low-x gluons $xg(x, Q^2)$ does not grow forever. The gluons with typical transverse size of $1/Q$ start to overlap at certain density and interaction in which two gluons fuse to one ($g + g \rightarrow g$) leads to a saturation of gluon density. The gluons then form a classical Yang-Mills field called "color glass condensate" and the nucleus-nucleus collision is described as a collision of two classical field with fast partons acting as sources[54].

2.1.2 Fireball expansion

After the dense hadronic matter is produced in the initial phase of the collisions the whole region is expected to expand before it reaches final break-up. The rate of the expansion depends on the underlying constituents and their interactions inside of the "fireball".

For a description of such a dense, strongly interacting matter is most convenient to use hydrodynamic framework, as it was first proposed by Landau in 1953[55]. It should be stressed that for applicability of hydrodynamics approach to the heavy ions collision basics prerequisites must be satisfied. The hydrodynamics requires local thermal equilibrium to be established. While this is automatically assumed in some of the theoretical calculation ,such as those on lattice, it's not obvious that it is true in reality for such a small and short-lived system. Thus answering the question of thermalization itself is important for heavy-ion collisions, as macroscopic properties such as temperature, pressure and entropy are not well defined otherwise.

It's expected that if the QGP is to be formed it has to be immediately after the collision when the energy density is highest and the temperature of the matter is above the critical value of T_c. The system will thereafter expand and cool till it reaches the T_c where a phase transition into hadronic matter occurs. The exact nature of the phase transition and hadronization is not yet known, although the data suggest that at conditions at RHIC it is a crossover transition - mixed phase of partonic and hadronic matter. Even in the hadronic phase the system interacts and keeps expanding and cooling. Individual particles can still be created and destroyed in the inelastic collisions until system cools down to a temperature of "*chemical freeze-out*", T_{ch}. After this the inelastic collision cease and particle ratios are fixed. The expansion continues until the "kinetic freeze-out" (T_k). At this point hadrons stop scattering and free-stream out of the system.

2.2 Probes (Observables)

Heavy-ions experiments are designed to measure number of different observables. It's unlikely that the conclusive evidence of a formation of the QGP could be based on a single observable. Instead, simultaneous observation of many signals is required. It is expected that only consistent analysis of many signal can lead to an unambiguous identification of the phase transition. Many of the measured signals are only indirect, because they are related to particles that undergo many reinteractions from the time of the early collision to the time of the final detection.

In the following section are discussed the key measurable signals giving information about different parts of the ultra-relativistic heavy-ions collision and possible QGP phase transition. The experiment at RHIC and experiments at lower energies extracted vast amount of experimental information about heavy-ions collisions. The emphasis of this section is to briefly review those predictions and results that are connected with topic of this thesis and allow to present the physics motivation and frame the obtained results in the wider picture of the current understanding of this field of research.

2.2.1 Energy density

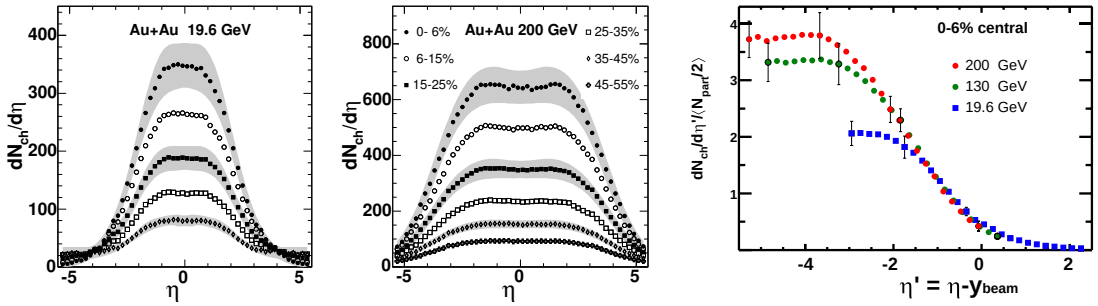

(a) (b)

Figure 2.4: (a)Charged particle pseudo-rapidity distributions and it's centrality dependence, as measured by PHOBOS experiment, at $\sqrt{s_{NN}}$=19.6 and 200 GeV. Figure adapted from [56]. (b)Shifted pseudo-rapidity distribution $dN_{ch}/d\eta'$ where $\eta' = \eta - y_{beam}$ for the 0-6% of most central collisions at three different Au+Au collision energies. Figure from [57].

Pseudo-rapidity distributions of particle production have been meassured at RHIC at various energies and collision systems[59, 60, 57]. It describes general characteristics of the particle production and can be used to estimate energy density in the system. The Figure 2.4a shows example pseudo-rapidity distribution of charged particle, $dN_{ch}/d\eta$, measured by PHOBOS experiment at two different collision energies. As we progress to large energies the distribution gets wider and starts to develop a plateau at the mid rapidity. The tails

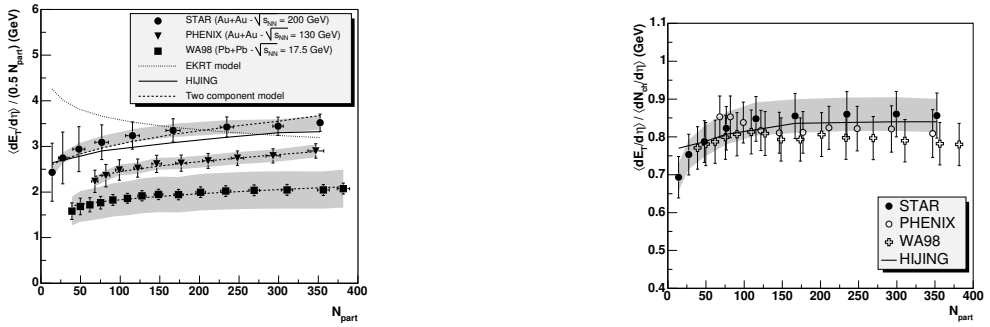

(a) (b)

Figure 2.5: (a) $\langle dE_T/d\eta|_{\eta=0.5}\rangle$ per $N_{part}/2$ vs. N_{part}(from HIJING model) from STAR, PHENIX and WA98 experiments together with model predictions. (b) $\langle dE_T/d\eta\rangle/\langle dN_{ch}/d\eta\rangle$ vs. N_{part} for the same data. Both figures adapted from [58].

of the distribution close to the rapidity of the beam show strong similarity. This is shown by Figure 2.4b where distribution is shifted to the beam rapidity a replotted as a function of $\eta' = \eta - y_{beam}$. The distributions are then similar across different beam energies and also collision systems. This feature is called *limiting fragmentation* and show that at high enough energies the particle production close to the beam rapidity has reached a limiting value. In the mid-rapidity region the number of produced particles depends on collision energy and number of nucleons participating in the collision (ie. the centrality). By measuring at the same time the transverse energy distribution $dE_T/d\eta$ [61, 58], as shown in the Figure 2.5a, we can estimate the average transverse energy per produced particle. The results on $\langle dE_T/d\eta\rangle/\langle dN_{ch}/d\eta\rangle$ in Figure 2.5b tell us that average transverse energy of $\sim 0.8\ GeV$ is only weakly dependent on energy. By combining these measurements we can make a crude estimate of the energy density ϵ_0 achieved in the collision with use of simplified Bjorken scenario of longitudinal expansion [62]:

$$\epsilon_0 = \frac{1}{\pi R^2 \tau_0} \frac{dE_T}{d\eta}\bigg|_{y \backsimeq 0}. \tag{2.1}$$

With the estimate of formation time $\tau_0 = 1$ fm and initial size $R = 1.2A^{1/3}$ we arrive at $\epsilon_0 \sim 4\ GeV/fm^3$ which is more then theoretically estimated critical density $\epsilon_{crit} \sim 1\ GeV/fm^3$ necessary for phase transition to the QGP phase.

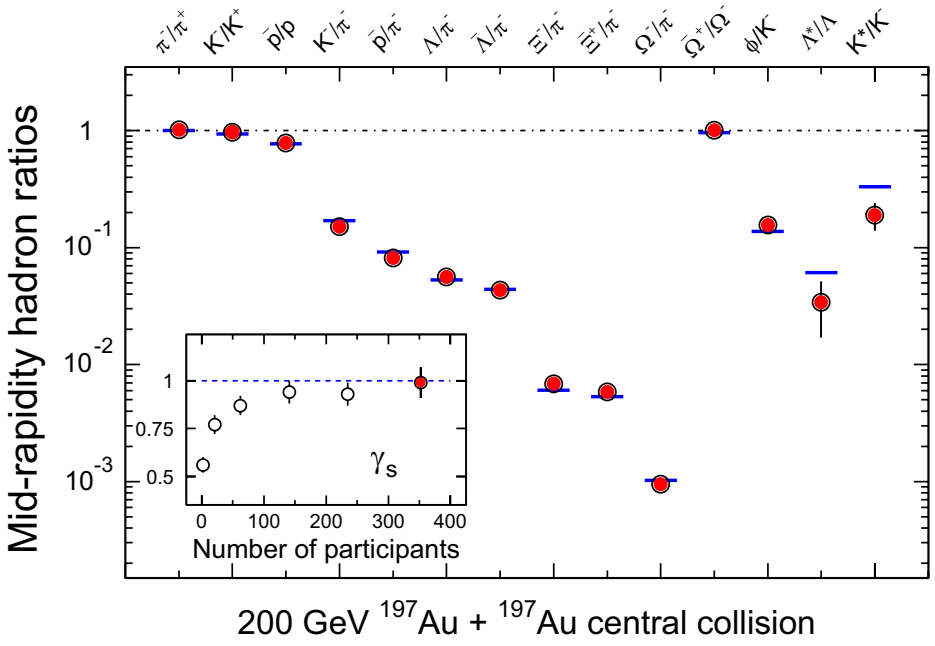

Figure 2.6: Ratios of particle yields at mid-rapidity in the most central Au+Au collisions at $\sqrt{s_{NN}}$=200 GeV, as measured by the STAR experiment. Horizontal bars represent statistical model fits to data with $T_{ch} = 163 \pm 5$ MeV, $\mu_b = 24 \pm 4$ MeV, and $\gamma_S = 0.99 \pm 0.07$. Figure from [63].

2.2.2 Particle ratios and yields

Particle production in a system that has reached a thermal equilibrium can be described by a grand canonical ensemble of statistical physics. The density of particle number n_i is

$$n_i = d_i \gamma_S \int \frac{d^3p}{(2\pi)^3} \frac{1}{\exp\left[(E_i - \mu_i)/T\right] \pm 1}, \tag{2.2}$$

where $\vec{p}$ is momentum, T temperature, and d_i, E_i, μ_i are spin degeneracy factor, total energy and chemical potential of the i-th particle respectively. The $\pm$ depends on whether the particle is boson(+) or fermion(-). In chemical equilibrium $\mu_i = \mu_B B_i - \mu_s S_i - \mu_I I_i^3$, where B_i, S_i, and I_i^3 are baryon number, strangeness and third isospin component of the particle. This means that by analyzing yields of particles produced at mid-rapidity, those mostly not coming from initial stages of the collisions, and their ratios we can access information about the bulk of the matter at the time when the particle production ceased - at the time of *chemical freeze-out* T_{ch}. The question of the thermalization and the temperature of the bulk is important, and crucial role in this analysis plays production and thermalization of strangeness.

Strangeness is not initially present in the system, thus all strange particles must be

created during the collision and the subsequent evolution of the system. In a collision of non-strange particles the strangeness ($s\bar{s}$-pair) is produced via associated production such as $\pi\pi \to K\bar{K}$ with relatively low cross section and higher threshold energy (in the mentioned case of $\pi\pi \to K\bar{K}$ it is $\sim$ 700 MeV). In the case of deconfined QGP the $s\bar{s}$-pairs can be created by gluon fusion $gg \to s\bar{s}$ without the non-strange quarks thus with lower threshold energy of $\sim$ 200 MeV. This energy is of the order of predicted temperature T_c necessary for the creation of QGP. The strange quarks can be easily produced in the QGP by collisions of thermalized partons. It is then predicted that an increased production of strangeness would be a viable sign of QGP [64, 65]. The presence of strangeness in the bulk of created matter does not automatically mean that the system lived long enough for strangeness to reach the chemical equilibrium that justifies the use grand canonical ensemble. For this reason a strangeness suppression factor γ_S is introduced into 2.2 that can be regarded as a measure of equilibration of the strangeness.

Figure 2.6 presents STAR results on statistical model fit wit Au+Au data at $\sqrt{s_{NN}}$=200 GeV[63]. As the inset of the figure shows, as we approach from peripheral to central collisions, the γ_S rises and reaches ~ 1 for the most central collisions. This suggest that the system in central collisions may live long enough to attain chemical equilibrium even for the strange quark. The temperature of chemical freeze-out obtained from such fits is found to be in a vicinity of $T_{ch} = 156 \sim 160$ MeV[63, 66, 67, 68] which is close to the predicted QCD phase transition temperature. The extracted T_{ch} was found to depend only slightly on whether particle species used for fit include strange and multistrange particles and also insensitive to centrality of the collision. This could imply that the system created in Au+Au collisions at RHIC always develops toward the same chemical-freeze-out condition regardless of the initial conditions.

2.2.3 Transverse spectra and Kinetic freeze-out

A characteristic feature of the heavy-ion collisions is a creation of system that strongly interacts for a significantly long time. This is expected to lead not only to the thermalization, but also to development of pressure and subsequent collective transverse expansion of the whole system. To describe single particle transverse momentum spectra at mid-rapidity it's necessary to superimpose such a common flow on the above described thermal emission of particles. The distribution of 2.2 is then modified to

$$\frac{d^6 N_i}{d^3x\, d^3p} = d_i \frac{d^3p}{(2\pi)^3} \frac{1}{\exp\left[(u(x)_\nu p_i^\nu - \mu_i)/T\right] \pm 1}, \tag{2.3}$$

where $u(x)_\nu$ is a 4-velocity field describing the flow of system.

The description of the transverse flow itself is often obtained from hydrodynamicaly

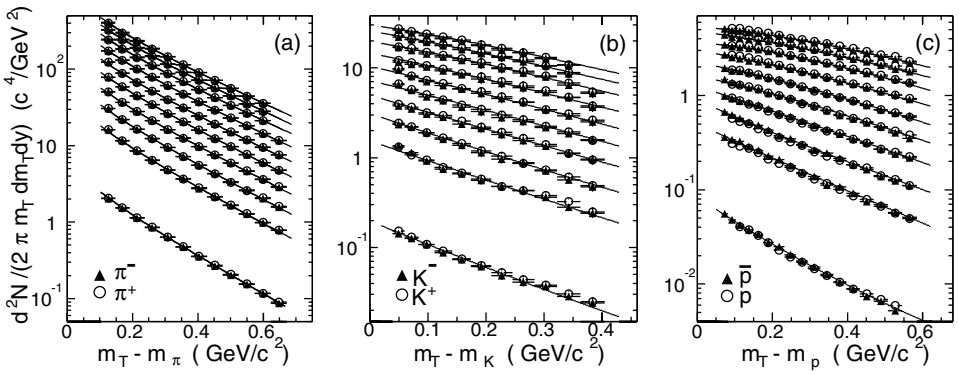

Figure 2.7: Invariant yield at mid rapidity as a function of m_T measured by STAR experiment at $\sqrt{s_{NN}}$=200 GeV collision energy. The data points correspond (from bottom up) to p+p collisions and Au+Au collisions at centrality from 70-80% up to %5 most central collisions. Figure from [67].

motivated parametrization, the so called *blast wave model* [69, 70, 71, 72, 73, 74]. These models allow to describe, under simplified assumptions, the emission of the particles from locally thermalized and transversely expanding source by few parameters only. The two most important parameters are the kinetic freeze-out temperature T_{kin} and average velocity of the transverse flow $\langle\beta\rangle$.

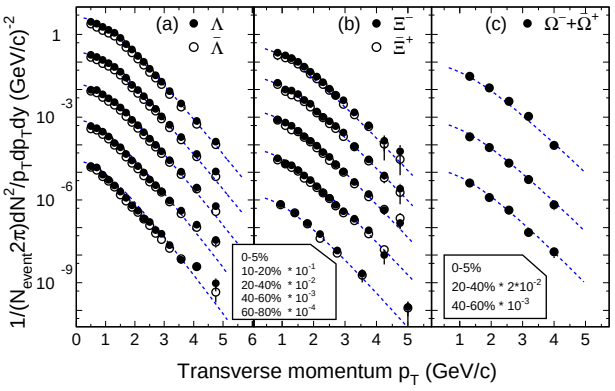

Figure 2.8: Transverse momentum distribution for strange and multistrange-hadrons in Au+Au at $\sqrt{s_{NN}}$=200 GeV. Figure from [75].

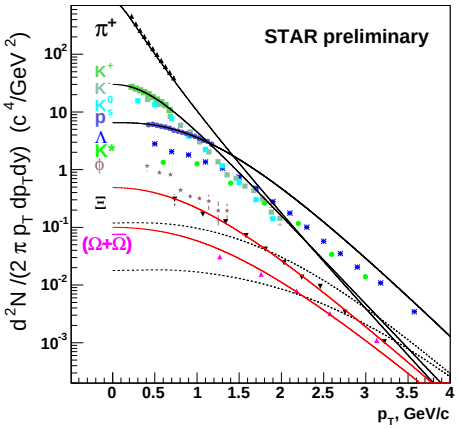

Figure 2.9: Identified particle spectra in %5 most central collisions together with blast wave calculations. Figure from [68].

The identified particle transverse mass $m_T = \sqrt{p_T^2 + m^2}$ spectra has been measured with excellent precision for not only the most common particles (π,p,K - Figure 2.7)[66, 67, 76], but also for multistrange particles(ϕ,Ξ,Ω - Figure 2.8) [77, 75, 78, 79, 80] and resonances[81, 82].

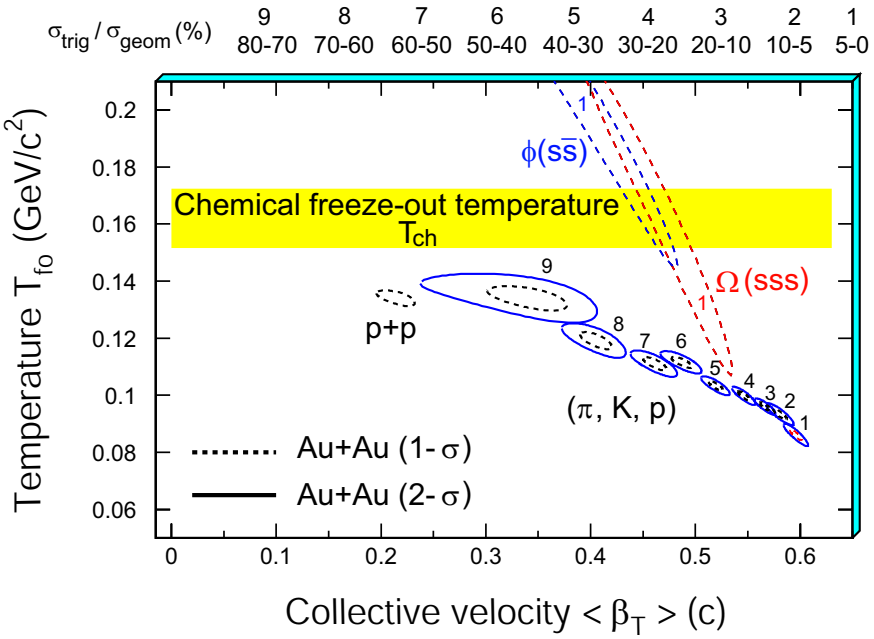

Figure 2.10: χ^2 contour of thermal + radial flow fit from collisions at $\sqrt{s_{NN}}$=200 GeV. The centrality selection is described at the top of the picture except for ϕ and Ω for which only central events are used. Figure from [63].

The effects of the transverse flow are well visible from comparison of the data from most central collisions in Figure 2.9. Going from pions to heavy particles the spectra flatten in low m_T region developing the so called "shoulder-arm" shape. The blast wave fits[69, 83] to the spectra then permit to extract the T_{kin} and $\langle\beta\rangle$ for the individual particle species. The obtained results visualized in Figure 2.10 show that kinetic freeze-out parameters for π,K,p are centrality dependent with decreasing T_{kin} and increasing $\langle\beta\rangle$ as we progress from peripheral to central collision. This shows that in central collisions for the most common particle species there is a significant delay between the chemical and kinetic freeze-out during which the system cools and develops significant radial flow by hadronic reinteraction.

However, as also shown in the Figure 2.10, the kinetic freeze-out parameters from for multi-strange particles[63, 75, 68] coincide with those of chemical freeze-out. This supports the idea that multistrange-particles may kinetically freeze-out earlier, and not participate in the hadronic phase due to their presumed low hadronic cross section[84].

2.2.4 Azimuthal anisotropy

In non-central collisions the overlap region where participants interact and deposit energy is azimuthaly asymmetric. The shape of the region is elongated in the direction out of the reaction plane; often quoted as an "almond shape". The created matter is not homogeneous

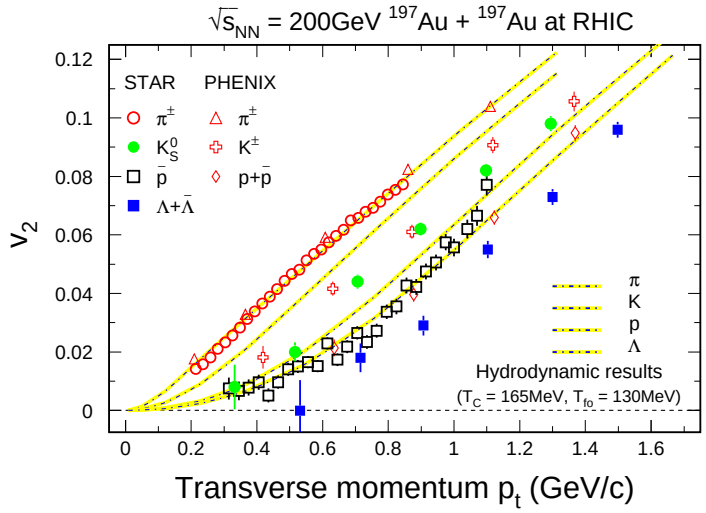

Figure 2.11: Elliptic flow v_2 for different particle species measured by STAR and PHENIX compared to hydrodynamic model predictions. Figure from [85].

and isotropic. This density gradient, if the matter reinteracts and thermalizes, gives rise to a pressure gradient which drives the collective expansion. By this process the initial geometrical asymmetry is transformed into azimuthal asymmetry of observed particle yields[87].

Experimentally the asymmetry is measured as coefficients in Fourier expansion of the azimuthal dependency of the particle spectra with respect to the reaction plane:

$$E\frac{d^3N}{d^3p} = \frac{d^2N}{2\pi\, p_T\, dp_T\, dy}\left(1 + \sum_{n=1}^{\infty} 2v_n \cos\left[n(\phi - \Psi_r)\right] + \dots\right), \tag{2.4}$$

where $\phi - \Psi_r$ is the angle of the particle with respect to the reaction plane Ψ_r. The v_1 and v_2 are called the "*directed*" and "*elliptic*" flow. At mid-rapidity the v_1 by symmetry vanishes, while v_2 can be non-zero. The strength of the v_2 is argued to be sensitive predominately to early times of the expansion and the possible phase transition [87, 88, 89]. One of the most pronounced predictions is a mass ordering of v_2 with the mass of the particle in a system driven by hydrodynamic expansion and it's sensitivity to the equation of state[90].

As shown in the Figure 2.11 measurements at $\sqrt{s_{NN}}$=200 GeV by STAR and PHENIX [91, 92, 93] show clear mass ordering of v_2 in the low p_T up to $p_T \approx 1.5$ GeV/c. The particles with smaller mass show higher v_2 at a given p_T then those with higher mass. The measurements at low p_T are rather well reproduced by hydrodynamics models.

Latest STAR results on elliptic flow[86, 92, 94, 95] (Figure 2.12) give evidence that this flow-induced mass ordering holds even for strange and multi-strange particles such as ϕ,Ξ,

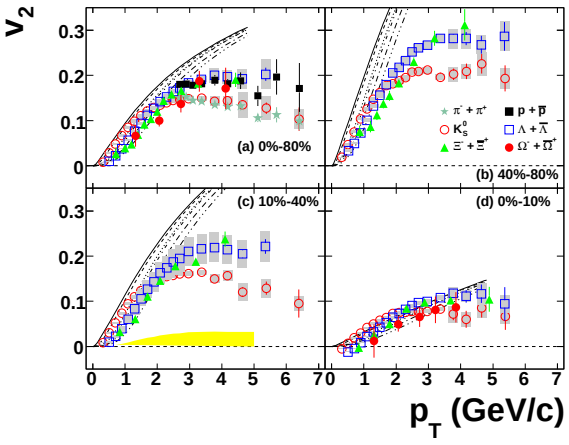

Figure 2.12: Centrality dependence of elliptic flow v_2 for different particle species including strange and multi-strange baryons. For comparison, lines show results from ideal hydrodynamics calculations. Figure from [86].

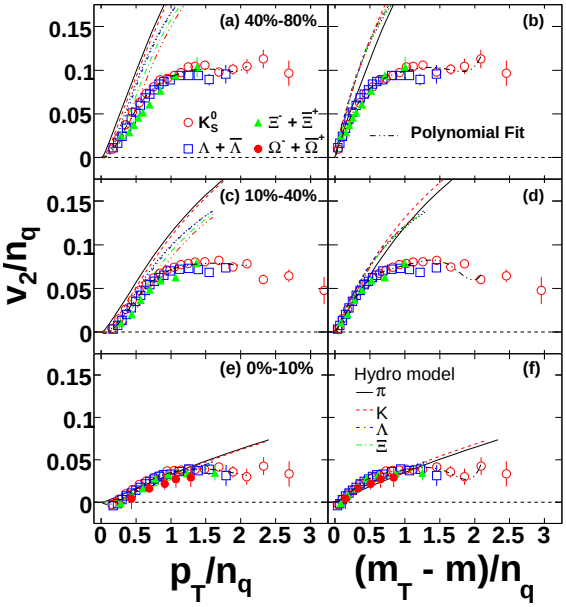

Figure 2.13: Centrality dependence of number-of-quark scaled v_2 (v_2/n_q) of identified particles versus p_T/n_q and $(m_T - m)/n_q$. Figure from [86].

and Ω. However at intermediate $1.5 < p_T < 5$ GeV/c the mass ordering ceases and the v_2 reaches a plateau with different value for baryon and mesons. This baryon-meson splitting can be explained in the framework of coalescence models assuming that all quarks attain the same v_2 throughout the evolution of the system. This is especially important assumption in the case of strange quarks. In the Figure 2.13 is shown v_2 scaled by number of constituent quarks versus similarly scaled p_T and $m_T - m$. In the region $0.6 < p_T/n_q < 2$ GeV/c the v_2/n_q is the basically the same regardless of particle species. This may point to a picture in which the anisotropic flow builds up already at the partonic stage and the hadronic v_2 is mainly a summation of v_2 of the underlying quarks.

2.3 Summary

From the measurements obtained at the RHIC collisions energies we can compose a very interesting picture of the heavy ion collisions. Although there are still many open questions remaining we can summarize some of the findings into a rather self-consistent picture.

The system created in the collision has high initial density and reaches temperature well above the critical temperature of the phase transition. Measurements show that the system undergoes violent evolution. The system exhibits very strong collective behavior in the transverse direction. At the energy of the RHIC collisions it is for the first time

that the development of the system seem can be well described by hydrodynamics. Most interestingly the observed collective behavior can be interpreted as coming predominantly from early partonic rather then later hadronic phase. The chemical composition of the particle species shows that the system evolves toward a common temperature of a chemical freeze-out. In the central collisions the system interacts and exists long enough to even thermally equilibrate the heavier strange quarks.

To study the partonic phase it is best to use observables that are more sensitive to the early stages of the collision and are less affected by the hadronic gas phase. The multistrange baryons could be regarded as good candidates for such a probe. Although they are affected by the partonic collectivity as much as other particles they seem to decouple earlier from the system shortly after the chemical freeze-out. This behavior could be a result of them having small interaction cross section with other non-strange hadrons, mainly pions. This assumption is rather speculative as the $\pi - \Xi$ cross section was never exactly measured. The question of the flow and early freeze-out of the multistrange baryons is interesting and important topic. The information about freeze-out of multistrange baryons is derived from the measurements in momentum space, but the flow and early freeze-out would also mean a very specific space-time configuration at the time of emission. The study of the space-time properties of the source emitting multistrange baryons, namely Ξ, is a main topic of this thesis.

Chapter 3

Two-particle correlation femtoscopy

The technique of particle femtoscopy utilizes measurements of momentum correlations between two particles at small relative momenta in their center of mass frame (CMS). This technique has been widely used over period of more then 25 years to study space-time characteristics of the particle production down to the details on level of 1 fm($= 10^{-15}$ m), therefore gaining the name "*femtoscopy*".

As a beginning of the field of femtoscopy is often regarded an experiment of Robert Hanbury-Brown and Richard Twiss in mid-fifties. For this experiment the Hanbury-Brown and Twiss developed a novel technique of photon intensity interferometry to be used as an alternative to the amplitude interferometry of Michelson[96, 97]. They successfully measured the angular radii of the Sirius star using space-time correlation of photons incoming into their two radio telescopes. As a recognition to their achievement the femtoscopic measurements are usually called HBT. However, we should note that in the above mentioned experiment the correlation comes from the interference of the two classical electromagnetic fields in the detection region. This effect is not of a quantum origin and would persist even under a limit $h \to 0$.

The momentum correlation as we understand femtoscopy throughout this work started by the observation of the so called GGLP effect. In 1959-1960 G.Goldhaber, S.Goldhaber,W.Lee and A.Pais discovered in the annihilation of $\bar{p}-p$ that there is an excess of pairs' of identical pions at small opening angles when compared to the unlike sign pions[98]. The effect was ascribed to the Bose-Einstein statistics of the pions[99]. This effect is of quantum origin, and as pointed out [100, 101] in a sense orthogonal to the correlation analyses of Hanbury-Brown and Twiss.

For historical reasons the term HBT if often used when referring to femtoscopic correlation measurements. Many terms such as 'HBT - radii' and 'HBT-puzzle' are well known in the heavy-ion community. Hence in this work the term HBT will be used when necessary for clarity of the text, but it will always mean momentum correlations similar to GGLP effect.

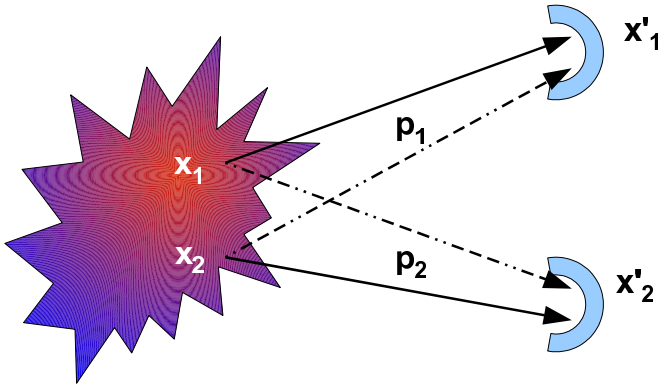

Figure 3.1: Basic principle of femtoscopy: A boson of momentum p_1 is detected at x'_1 and another identical boson with momentum p_2 is detected at x'_2. Since we cannot distinguish the particles from each other, we have to consider a superposition of both trajectories.

3.1 Formalism

In the general formalism of femtoscopy the particles emitted at close relative velocities may be correlated not only due to quantum statistics, but also due to strong or Coulomb interactions. These are called the "*final state interactions*" (FSI) as they can be viewed as an interaction that only slightly modifies momenta of the particles in their final states. The FSI interactions act between identical as well as non-identical particles. The use of the latter with particles of unequal masses can yield additional information about space-time properties of the source which are not accessible by measurement identical particles only. To review the theoretical framework of femtoscopy for the needs of this work we follow the formalism used by Lednicky in [102].

The probability of detecting two particles with 4-momenta $p_1 = (E_1, \boldsymbol{p}_1)$ and $p_2 = (E_2, \boldsymbol{p}_2)$ is related to doubly inclusive cross section determined by production amplitude $T(p_1, p_2\,; \alpha)$:

$$(2\pi)^6 \gamma_1 \gamma_2 \frac{d^6\sigma}{d^3\boldsymbol{p}_1 d^3\boldsymbol{p}_2} = \sum_\alpha |T(p_1, p_2\,; \alpha)|^2\,, \tag{3.1}$$

where$\gamma_i = E_i/m_i$, and $\alpha = \{S, m_S, \alpha'\}$ denotes summation over total spin S of the pair and it's projection m_S as well as summation over quantum numbers α' of other particles and integration over their momenta. For identical particles the amplitude $T(p_1, p_2\,; \alpha)$ must be properly symmetrized or antisymmetrized.

In a case of no FSI the production amplitude $T = T_0(p_1, p_2\,; \alpha)$ in the form of Fourier transform

$$T_0(p_1,p_2\,;\alpha) = \int d^4x_1\, d^4x_2\, e^{-\mathrm{i}p_1x_1} e^{-\mathrm{i}p_2x_2} \mathrm{T}(x_1,x_2\,;\alpha)$$
$$= \int d^4X\, d^4r\, e^{-\mathrm{i}PX} e^{-\mathrm{i}\tilde{q}r/2} \mathrm{T}(X,r\,;\alpha) = \int d^4r e^{-\mathrm{i}\tilde{q}r/2} \tau_P(r\,;\alpha) \quad (3.2)$$

allows to separate four-coordinates of the 2-particle center of mass of the system (CMS) $X = [(p_1P)x_1 + (p_2P)x_2]/P^2$, $P = p_1 + p_2$, and integrate over them. What remains are relative four-coordinates $r = (t, \boldsymbol{r})$ and generalized relative 4-momentum $\tilde{q} = q - P(qP)/P^2$,$q = p_1 - p_2$. Since $qP = m_1^2 - m_2^2$ then for identical particles $\tilde{q} = q$. Femtoscopy with non-identical particles is most often done in CMS system of the pair where $\boldsymbol{q}/2 = \boldsymbol{p}_1 = -\boldsymbol{p}_2 = \boldsymbol{k}^*$. If FSI is present between the emitted particles the $T(p_1,p_2\,;\alpha)$ is modified by an additional term $\Delta T(p_1,p_2\,;\alpha)$ originating from the FSI:

$$T(p_1,p_2\,;\alpha) = T_0(p_1,p_2\,;\alpha) + \Delta T(p_1,p_2\,;\alpha), \quad (3.3)$$

$$\Delta T(p_1,p_2\,;\alpha) = \frac{\mathrm{i}\sqrt{P^2}}{2\pi^3} \int d^4k \frac{T_0(k,P-k\,;\alpha) f^{S*}(p_1,p_2\,;k,P-k)}{(k^2 - m_1^2 - \mathrm{i}\epsilon)((P-k)^2 - m_2^2 - \mathrm{i}\epsilon)}. \quad (3.4)$$

The $f^{S*}(p_1,p_2\,;k,P-k)$ is a scattering amplitude, which in a case of small relative momenta $\boldsymbol{k}^*$, is diagonal in total spin S and does not depend on its projection. Inserting 3.2 and 3.4 into 3.3 gives

$$T(p_1,p_2\,;\alpha) = \int d^4x_1\, d^4x_2\, \psi^{S(-)}_{p_1,p_2}(x_1,x_2) \mathrm{T}(x_1,x_2\,;\alpha)$$
$$= \int d^4r\, \psi^{S(-)}_{\tilde{q}}(r) \tau_P(r\,;\alpha), \quad (3.5)$$

where

$$\psi^{S(-)}_{p_1,p_2}(x_1,x_2) = e^{-\mathrm{i}Pr} \psi^{S(-)}_{\tilde{q}}(r) = \left[e^{\mathrm{i}Pr} \psi^{S(+)}_{\tilde{q}}(r) \right]^* \quad (3.6)$$

is Bethe-Salpeter amplitude [103, 104] describing system of interacting particles and reduced Bethe-Salpeter amplitude $\psi^{S(-)}_{\tilde{q}}(r)$ which depends only on the relative r and $\tilde{q}$. Thus, as a result of FSI the plane waves in 3.2 are replaced by $\psi^{S(-)}_{\tilde{q}}(r)$ in 3.5. The two-particle inclusive cross section is obtained by substituting 3.5 into 3.1:

$$(2\pi)^6 \gamma_1\gamma_2 \frac{d^6\sigma}{d^3\boldsymbol{p}_1 d^3\boldsymbol{p}_2}$$
$$= \sum_S \int d^4x_1\, d^4x_2\, d^4x_1'\, d^4x_2'\, \rho_S(x_1,x_2\,;x_1',x_2') \psi^{S(-)}_{p_1,p_2}(x_1,x_2) \psi^{S(-)*}_{p_1,p_2}(x_1',x_2') \quad (3.7)$$
$$= \sum_S \int d^4r\, d^4r'\, \rho_{PS}(r,r') \psi^{S(-)}_{\tilde{q}}(r) \psi^{S(-)*}_{\tilde{q}}(r'),$$

where

$$\begin{aligned}\rho_S(x_1,x_2\,;x_1',x_2') &= \sum_{M,\alpha'} \mathrm{T}(x_1,x_2\,;S,M,\alpha')\mathrm{T}^*(x_1',x_2'\,;S,M,\alpha'),\\ \rho_{PS}(r,r') &= \int d^4X\, d^4X'\, e^{-\mathrm{i}P(X-X')} \\ &\quad \rho_S(X+\frac{p_2P}{P^2}x, X-\frac{p_1P}{P^2}x, X'+\frac{p_2P}{P^2}x', X'-\frac{p_1P}{P^2}x')\end{aligned} \tag{3.8}$$

represents a space-time density matrices.

The space-time density matrix is easily shown to be related to two particle emission function by considering the particles to be without FSI in 3.7. Replacing the wave function by a plane wave $\psi^{S(-)}_{p_1,p_2} = e^{-\mathrm{i}p_1x_1-\mathrm{i}p_2x_2}$ and performing partial Fourier transform in coordinates

$$\bar{x}_i = \frac{1}{2}(x_i+x_i') \quad \epsilon_i = x_i - x_i' \tag{3.9}$$

in 3.7 yields

$$\begin{aligned}&(2\pi)^6\gamma_1\gamma_2\frac{d^6\sigma_0}{d^3\boldsymbol{p}_1 d^3\boldsymbol{p}_2}\\ &= \sum_S \int d^4x_1\, d^4x_2\, d^4x_1'\, d^4x_2'\, \rho_S(x_1,x_2\,;x_1',x_2') e^{-\mathrm{i}p_1(x_1-x_1')-\mathrm{i}p_2(x_2-x_2')}\\ &= \sum_S \int d^4\bar{x}_1\, d^4\bar{x}_2\, G_S(\bar{x}_1,p_1\,;\bar{x}_2,p_2) = \sum_S \int d^4\bar{r}\, g_{PS}(\bar{r},\tilde{q})\,,\end{aligned} \tag{3.10}$$

where

$$\begin{aligned}G_S(\bar{x}_1,p_1\,;\bar{x}_2,p_2) &= \int d^4\epsilon_1\, d^4\epsilon_2\, e^{-\mathrm{i}p_1\epsilon_1-\mathrm{i}p_2\epsilon_2}\rho_S(\bar{x}_1+\frac{\epsilon_1}{2},\bar{x}_2+\frac{\epsilon_2}{2},\bar{x}_1-\frac{\epsilon_1}{2},\bar{x}_2-\frac{\epsilon_2}{2})\\ g_{PS}(\bar{r},\tilde{q}) &= \int d^4\bar{X}\, G_S(\bar{X}+\frac{p_2P}{P^2}\bar{r},p_1\,;\bar{X}-\frac{p_1P}{P^2}\bar{r},p_2).\end{aligned} \tag{3.11}$$

The $G_S(\bar{x}_1,p_1\,;\bar{x}_2,p_2)$ is then a two-particle emission function, partial Fourier transform of the density matrix, closely related to Wigner density and $g_S(\bar{r},\tilde{q})$ depends only on relative distances.

3.1.1 Identical non-interacting particles

The formalism of classical femtoscopic measurements(the GGLP effect) that deals only with identical non-interacting particles can be obtained from the above general case. First for identical particles the Bethe-Salpeter amplitude $\psi^{S(-)}_{p_1,p_2}(x_1,x_2)$ must be replaced by a

properly symmetrized one:

$$\psi^{S(-)}_{p_1,p_2}(x_1,x_2) \to \frac{1}{\sqrt{2}}\left[\psi^{S(-)}_{p_1,p_2}(x_1,x_2)+(-1)^S\psi^{S(-)}_{p_2,p_1}(x_1,x_2)\right]. \tag{3.12}$$

Although in a case of measurements with identical pions and kaons, the particles interact also by Coulomb and the strong force the formalism for non-interacting can be used to a good extent. In these systems the effects of the strong interaction at low q are negligible and correlation due to Coulombic force can be subtracted in a first order of approximation. Under such circumstances we can replace $\psi^{S(-)}$ with plane waves

$$\psi^{S(-)}_{p_1,p_2}(x_1,x_2) = \frac{1}{\sqrt{2}}\left[e^{-\mathrm{i}p_1x_1-\mathrm{i}p_2x_2}+(-1)^S e^{-\mathrm{i}p_1x_2-\mathrm{i}p_2x_1}\right]. \tag{3.13}$$

Inserting the symmetrized wave function 3.13 into 3.7 gives the two particle inclusive cross-section

$$\begin{aligned}(2\pi)^6\gamma_1\gamma_2\frac{d^6\sigma}{d^3p_1d^3p_2} &= \sum_S\int d^4x_1\,d^4x_2\,d^4x_1'\,d^4x_2'\,\rho_S(x_1,x_2\,;x_1',x_2')\\ \frac{1}{2}\left[e^{-\mathrm{i}p_1\epsilon_1-\mathrm{i}p_2\epsilon_2}+e^{-\mathrm{i}p_1\epsilon_2-\mathrm{i}p_2\epsilon_1}+(-1)^S e^{\mathrm{i}p\epsilon_1-\mathrm{i}p\epsilon_2}\left(e^{-\mathrm{i}(\bar{x}_1-\bar{x}_2)}+e^{+\mathrm{i}(\bar{x}_1-\bar{x}_2)}\right)\right] &\\ = \sum_S\int d^4\bar{x}_1\,d^4\bar{x}_2\left[G_S(\bar{x}_1,p_1\,;\bar{x}_2,p_2)+G_S(\bar{x}_1,p\,;\bar{x}_2,p)(-1)^S cos(q\bar{r})\right],&\end{aligned} \tag{3.14}$$

where substitutions similar to 3.9 was done:

$$\bar{x}_i = \frac{1}{2}(x_i+x_i') \quad \epsilon_i = x_i - x_i' \quad p = \frac{1}{2}(p_1+p_2) \quad \bar{r} = \bar{x}_1-\bar{x}_2 \tag{3.15}$$

The actual correlation function is usually defined with respect to the uncorrelated two-particle distribution 3.10:

$$R(p_1,p_2) = \frac{d^6\sigma(p_1,p_2)}{d^6\sigma_0(p_1,p_2)}. \tag{3.16}$$

To experimentally obtain such a fully uncorrelated "*background*" distribution is a matter of rather subtle technique that will be explained later. Using the above definition of the correlation function with 3.14 and 3.10 we arrive at

$$R(p_1,p_2) = 1+\frac{\sum_S\int d^4\bar{x}_1d^4\bar{x}_2\,G_S(\bar{x}_1,p\,;\bar{x}_2,p)(-1)^S cos(q\bar{r})}{\sum_S\int d^4\bar{x}_1d^4\bar{x}_2\,G_S(\bar{x}_1,p_1\,;\bar{x}_2,p_2)}. \tag{3.17}$$

The numerator of 3.17 depends on two-particle emission function enumerated at off-mass shell momentum p:

$$G_S(x_1,p\,;x_2,p) = G_S(x_1,p_1-\tfrac{q}{2}\,;x_2,p_2+\tfrac{q}{2}) \tag{3.18}$$

If the emission function G_S varies only slowly with momentum we can use the so called "*smoothness approximation*" and do , for small values of q, replacement

$$G_S(x_1, p_1 - \tfrac{q}{2}\,; x_2, p_2 + \tfrac{q}{2}) \longrightarrow G_S(x_1, p_1\,; x_2, p_2) \tag{3.19}$$

The correlation function 3.17 then reduces into

$$\begin{aligned} R(p_1, p_2) &= 1 + \frac{\sum_S (-1)^S \int d^4x_1 d^4x_2\, G_S(x_1, p_1\,; x_2, p_2) cos(q\bar{r})}{\sum_S \int d^4x_1 d^4x_2\, G_S(x_1, p_1\,; x_2, p_2)} \\ &= 1 + \frac{\sum_S (-1)^S \int d^4r\, g_{PS}(x, q) cos(qr)}{\sum_S \int d^4r\, g_{PS}(r, q)} \end{aligned} \tag{3.20}$$

Although the 3.20 seems to give a one to one relation between emission function describing the source and the correlation function as its 4-dimensional Fourier transform we are in reality not able to fully reconstruct the emission function $g_{PS}(r, q)$ from the correlation function $R(p_1, p_2)$. The reason for it is the *mass-shell constrain* of the 4-vector $q = p_1 - p_2$. Since both p_1 and p_2 are 4-momenta of real particles the q is also on the mass shell. This can be expressed by $q_0 = \boldsymbol{\beta q}$ with $\boldsymbol{\beta} = \boldsymbol{P}/|\boldsymbol{P}|$. Introducing this constrain into 3.20 we obtain

$$\begin{aligned} R(p_1, p_2) &= 1 + \frac{\sum_S (-1)^S \int d^3\boldsymbol{r}\, cos(\boldsymbol{qr}) \int dt\, g_{PS}(\boldsymbol{r} + \boldsymbol{\beta} t, \boldsymbol{q})}{\sum_S \int d^4r\, g_{PS}(rq)} \\ &= 1 + \frac{\sum_S (-1)^S \int d^3\boldsymbol{r}\, S_{PS}(\boldsymbol{r}, \boldsymbol{q}) cos(\boldsymbol{qr})}{\sum_S \int d^3\boldsymbol{r}\, S_{PS}(\boldsymbol{r}, \boldsymbol{q})}. \end{aligned} \tag{3.21}$$

The information that can be obtained from the correlation function is then only about *relative emission function*

$$S_{PS}(\boldsymbol{r}, \boldsymbol{q}) = \int dt\, g_{PS}(\boldsymbol{r} + \boldsymbol{\beta} t, \boldsymbol{q}). \tag{3.22}$$

The deconvolution of the $\boldsymbol{r}$ and $\boldsymbol{t}$ can be done employing some external model of the emission function $G_S(x_1, p_1\,; x_2, p_2)$.

3.1.2 Bertsch-Pratt coordinate system

In the femtoscopic analyses of the correlation function $R(p_1, p_2) = R(P, q)$ the standard global Cartesian system *x-y-z* is not optimal. The most common and also the only one used throughout this work is a Bertsch-Pratt (*out-side-long*) coordinate system[105, 106, 107, 108, 109]. The system is connected to the geometry of the emitted pair and takes advantage of the prominent directions of the heavy ion-collisions, beam and transverse direction. The three main Cartesian axis are defined, as shown in the Figure 3.2, in the following way: The longitudinal (*long*) axis is parallel to the beam direction (in the laboratory frame usually denoted *z*). The *out* axis is chosen parallel to the pairs transverse momentum $\boldsymbol{P}$, thus is

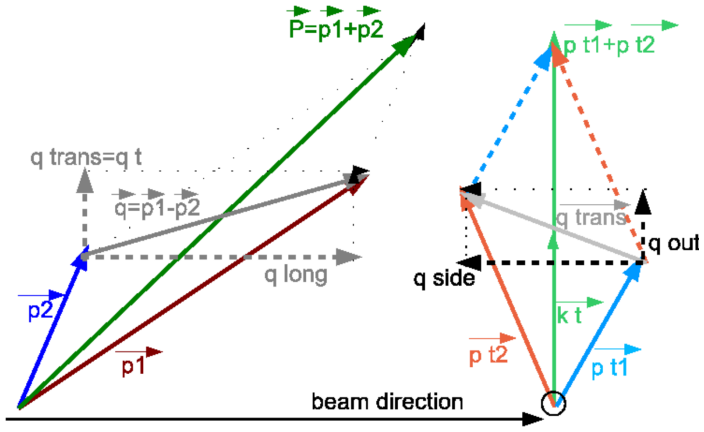

Figure 3.2: Bertch-Pratt coordinate system of the pair. Decomposition of $\boldsymbol{q}$ vector of the pair into the *out-side-long* coordinate system used in the femtoscopic measurements.

specific for every pair. The *side* axis is the remaining perpendicular direction. Any spacial vector $\boldsymbol{v}$ is decomposed as

$$\begin{aligned} v_{long} &= v_z \\ v_{out} &= (P_x v_x + P_y v_y)/P_T \\ v_{side} &= (P_x v_y - P_y v_x)/P_T, \end{aligned} \tag{3.23}$$

where $P_T = \sqrt{P_x^2 + P_y^2}$.

A most common reference frame for femtoscopic analyses of identical particles is the *longitudinally co-moving system (LCMS)* of the pair. This frame is boosted from the laboratory rest frame along the beam (long) direction so that the P_{long} of the pair vanishes. In a case of correlation of interacting particles, as is the case of this study, the two particle wave function, which describes their interaction, is defined in the *pair's rest frame* (CMS). The CMS frame is obtained from LCMS by an additional boost in the *out* direction so that also the $P_{out} = 0$.

3.1.3 Gaussian parametrization

The correlation function $R(P, q)$ carries information about the 3-dimensional shape of the relative emission function $S_{PS}(\boldsymbol{r}, \boldsymbol{q})$. In practical analyses the emission function as well as the correlation function are parametrized to characterize its main spacio-temporal features. The easiest way is to describe a single-particle emission function $G_S(x, p)$ in a Wigner rep-

resentation by a Gaussian approximation[110, 109]. In the most general case:

$$G_S(x,p) = N\exp\left[-\frac{1}{2}A_{\mu\nu}(p)(x^\mu - \bar{x}^\mu(p))(x^\nu - \bar{x}^\nu(p))\right]. \tag{3.24}$$

The two-particle emission function is then

$$G_S(p_1,x_1,p_2,x_2) = G_S^a(x_1,p_1)G_S^b(x_2,p_2). \tag{3.25}$$

Such a parametrization has multiple advantages. As the equation 3.21 shows a Gaussian source function leads, for identical non-interacting particles,to a Gaussian correlation function which greatly simplifies analyses. Also, any fluctuations in collision parameters and particle production will naturally, via central limit theorem, lead to Gaussian shapes. Although it's know that real sources deviate from Gaussian[111] the obtained parameters characterize well the main features of the source using minimal number of parameters.

As shown in [109] due to symmetries of the system most of the cross terms are forbidden with the exception of a cross term between x_{out} and time. For radially symmetrical system also offsets in the *side* and *long* direction are zero. We are then left with four RMS radii($\sigma_{out}, \sigma_{side}, \sigma_{long}, \Delta\tau$) and only two offsets ($\bar{x}_{out}, \bar{t}$) to characterize the single-particle emission function:

$$G_S(x,p) \sim \exp\left[-\frac{(x_{out} - \bar{x}_{out} - V_{out}(t-\bar{t}))^2}{2\sigma_{out}^2} - \frac{(x_{side})^2}{2\sigma_{side}^2} - \frac{(x_{long})^2}{2\sigma_{long}^2} - \frac{(t-\bar{t})^2}{2(\Delta\tau)^2}\right], \tag{3.26}$$

where V_{out} is a transverse velocity of the source. The relative emission function $S_{PS}(\boldsymbol{r},\boldsymbol{k})$, according to 3.22, is then

$$\begin{aligned} S_{PS}(\boldsymbol{r},\boldsymbol{k}) &\sim \exp\left[-\frac{[r_{out} - \langle r\rangle_{out}]^2}{4\gamma_\perp R_{out}^2} - \frac{r_{side}^2}{4R_{side}^2} - \frac{r_{long}^2}{4R_{long}^2}\right] \\ R^2{}_{out} &= \frac{1}{2}\left[\sigma_{a,out}^2 + \sigma_{b,out}^2 + (V_{a,out} - V_\perp)^2(\Delta\tau_a)^2 + (V_{b,out} - V_\perp)^2(\Delta\tau_b)^2\right], \\ R^2{}_{side} &= \frac{1}{2}\left[\sigma_{a,side}^2 + \sigma_{b,side}^2\right], \qquad R^2{}_{long} = \frac{1}{2}\left[\sigma_{a,long}^2 + \sigma_{b,long}^2\right], \\ \langle r\rangle_{out} &= \bar{x}_{a,out} - \bar{x}_{b,out} - V_\perp(\bar{t}_a - \bar{t}_b) \end{aligned} \tag{3.27}$$

where $V_\perp$ is a transverse velocity of the pair in LCMS frame and $\gamma_\perp \equiv (1 - V_\perp)^{-1/2}$. Naturally, for identical particles the mean values of the relative shift in the *out* direction will be $\langle r\rangle_{out} = 0$. In 3.27 the information about lifetime $\Delta\tau$ of the source is folded into the measured R_{out} radii. If the two single particle radii σ_{out} and σ_{side} are approximately the

same we can estimate the life time of the source from difference between measured R_{out} and R_{side}

$$R_{out}^2 - R_{side}^2 \approx (V_{out} - V_\perp)^2 (\Delta\tau)^2. \tag{3.28}$$

For non-interacting identical particles whose correlation function is determined solely by quantum symmetrization effects, ie. the correlation function is Fourier transform of the emission function, the final correlation function(in the LCMS frame) resulting from distribution 3.27 according to 3.21 is then:

$$R(\boldsymbol{q}) = 1 + \exp\left[-q_{out}^2 R_{out}^2 - q_{side}^2 R_{side}^2 - q_{long}^2 R_{long}^2\right]. \tag{3.29}$$

3.1.4 Non-identical interacting particles

If a final state interaction is present the Bethe-Salpeter amplitude 3.6 is

$$\psi_{\tilde{q}}^{S(+)}(r) = e^{\mathrm{i}\tilde{q}r/2} + \Delta\psi_{\tilde{q}}^{S(+)}(r), \tag{3.30}$$

with the correction $\Delta\psi_{\tilde{q}}^{S(+)}(r)$ derived from 3.4:

$$\Delta\psi_{\tilde{q}}^{S(+)}(r) = \frac{\sqrt{P}}{2\pi^3 \mathrm{i}} e^{-\mathrm{i}Px(1+Pq/P^2)/2} \int d^4k \frac{e^{\mathrm{i}kx} f^S(p_1, p_2\,; k, P-k)}{(k^2 - m_1^2 + \mathrm{i}\epsilon)((P-k)^2 - m_2^2 + \mathrm{i}\epsilon)} \tag{3.31}$$

Similarly as in section 3.1.1 we can separate the motion of the center of mass in 3.7 into a factor $\exp[\mathrm{i}P(X - X')]$ and using the *smoothness* approximation we can neglect all $\tilde{q}$ with regard to p_1, p_2. This allows to rewrite 3.7 in terms of the emission function G_S 3.10:

$$\begin{aligned}(2\pi)^6 \gamma_1\gamma_2 \frac{d^6\sigma}{d^3p_1 d^3p_2} &= \sum_S \int d^4x_1\, d^4x_2\, G_S(x_1, p_1\,; x_2, p_2) \left|\psi_{\tilde{q}}^{S(+)}(r)\right|^2 \\ &= \sum_S \int d^4r\, g_{PS}(r, \tilde{q}) \left|\psi_{\tilde{q}}^{S(+)}(r)\right|^2.\end{aligned} \tag{3.32}$$

In the CMS of the pair ($P = 0$, $\tilde{q} = \{0, \boldsymbol{k}^*\}$, $r = \{t^*, \boldsymbol{r}^*\}$) the two-particle wave function $\psi_{\tilde{q}}^{S(+)}(r)$ can be, at low q, replaced with a stationary solution of the scattering problem $\psi_{-\boldsymbol{k}^*}^S(\boldsymbol{r}^*)$:

$$(2\pi)^6 \gamma_1\gamma_2 \frac{d^6\sigma}{d^3p_1 d^3p_2} = \sum_S \int d^3\boldsymbol{r}^*\, S_{PS}(\boldsymbol{r}^*, \boldsymbol{k}^*) \left|\psi_{-\boldsymbol{k}^*}^S(\boldsymbol{r}^*)\right|^2. \tag{3.33}$$

For a short range interaction this solution asymptotically approaches at large $r^* = |\boldsymbol{r}^*|$ a superposition of the plane and outgoing spherical wave.

$$\psi^S_{-\boldsymbol{k}^*}(\boldsymbol{r}^*) = e^{\mathrm{i}\boldsymbol{k}^*\boldsymbol{r}^*} + f^S(k^*)\frac{e^{\mathrm{i}k^*r^*}}{r^*}, \tag{3.34}$$

considering that the interaction is dominated by the s-wave at sufficiently low $k^* = |\boldsymbol{k}^*|$.

If a long-range Coulomb interaction is present it modifies both, the incoming plane and the outgoing spherical wave [112, 113]:

$$\psi_{-\boldsymbol{k}^*}(\boldsymbol{r}^*) = e^{\mathrm{i}\delta_c}\sqrt{A_c(\eta)}\left[e^{\mathrm{i}\boldsymbol{k}^*\boldsymbol{r}^*}F(-\mathrm{i}\eta, 1, \mathrm{i}\xi) + f_c(k^*)\frac{\tilde{G}(\rho,\eta)}{r^*}\right]. \tag{3.35}$$

Here $\rho = k^*r^*, \xi = \boldsymbol{k}^*\boldsymbol{r} + k^*r^* = \rho(1 + cos\theta^*)$, $\eta = (k^*a)^{-1}$, a is a two-particles Bohr radius, and $f_c(k^*) = f(k^*)/A_c(\eta)$. The $\delta_c = \mathrm{arg}\Gamma(1 + \mathrm{i}\eta)$ is a Coulomb s-wave shift and

$$A_c(\eta) = \left|\psi^{Coul}_{-\boldsymbol{k}^*}(0)\right|^2 = 2\pi\eta\left[e^{2\pi\eta} - 1\right]^{-1} \tag{3.36}$$

is the Gamow factor; square of the non-relativistic Coulomb wave function at $r^* = 0$. $F(\alpha, 1, z)$ is confluent hypergeometric function and $\tilde{G}(\rho, \eta)$ is a combination of regular and singular s-wave functions (see [113] for details).

The equation 3.35 shows a very important features which is a corner stone of the analysis in this thesis. The information about the space-time shift $\boldsymbol{r}^*$ between the emitted particles enters through terms odd in $\boldsymbol{k}^*\boldsymbol{r}$. The correlation function is then sensitive to the angle θ^* between $\boldsymbol{k}^*$ and $\boldsymbol{r}^*$. As an example, in a case of a dominant Coulomb FSI interaction in the 3.35 the correlation function can be evaluated according to 3.32 and 3.16:

$$R(p_1, p_2) = A_c(\eta)\left[1 + 2\langle r^*(1 + \cos\theta^*)/a\rangle + \dots\right]. \tag{3.37}$$

The average $\langle\rangle$ is meant in a sense of integration over relative emission function $g_{PS}(\boldsymbol{r}^*, \boldsymbol{k}^*)$ and summation over spins states S, as in 3.32. It has been first pointed out in [114] that this can be used to access information about asymmetry $\langle r^*\rangle$ in the particle emission between two particle species. In a case of radially symmetric system, as considered before in 3.27, the shift $\boldsymbol{r}^*$ in the CMS is:

$$\langle r^*\rangle_{out} = \gamma_\perp\langle r\rangle_{out} = \gamma_\perp(\Delta\bar{x}_{out} - V_\perp\Delta\bar{t}), \quad \langle r^*\rangle_{side} = 0, \quad \langle r^*\rangle_{long} = 0, \tag{3.38}$$

with average shift possible only in the *out* direction. The sensitivity of the correlation function on the product $\boldsymbol{k}^*\boldsymbol{r}^*$ can be imagined in a classical analogy. If the vector $\boldsymbol{k^*}$ has the same direction as $\boldsymbol{r}^*$ the two particles move away from each other in the center of mass frame

of the pair. On the other hand if the vectors $\boldsymbol{k^*}$ and $\boldsymbol{r}^*$ have opposite direction they move initially toward each other after they are emitted. The second case gives the two particles, under classical considerations, effectively more time to interact, thus making the correlation stronger.

Experimentally we cannot measure the sign of $\boldsymbol{k}^*\boldsymbol{r}^*$ directly since we cannot directly observe the direction of $\boldsymbol{r}^*$. Only $\boldsymbol{k}^*$ is directly measurable. What we can do is to use other measurable vector such as the total momentum of the pair P and test if the strength of the correlation function varies with direction of such vector. If it does this means that there exists a relation between the vectors direction and direction of the $\boldsymbol{r}^*$. A straightforward method to test if there exists a shift in the average emission point between particle-species in a given direction was proposed in [114]. The the data is split into to two parts depending on a sign of product $\boldsymbol{k}^*\boldsymbol{P}$ and two correlation functions are created: $C_+(k^*)$ for pairs with $\boldsymbol{k}^*\boldsymbol{P} > 0$ and $C_-(k^*)$ for those with $\boldsymbol{k}^*\boldsymbol{P} < 0$. The ratio of the two correlation functions C_+/C_- is then sensitive to the average shift $\langle r^* \rangle$. Since in heavy-ion collisions the symmetry constrains usually allow only shift in the *out* direction(3.38) the two correlation function C_+,C_- are usually constructed with respect to the vector P_{out}.

3.2 Experimental correlation function

The two-particle correlation function $R(p_1, p_2)$ 3.16 is defined as a ratio two-particle inclusive spectra - one including the FSI and one without the FSI. The experimental correlation function $C_{\boldsymbol{K}}(\boldsymbol{q})$, where $K = P/2$, is constructed as a normalized ratio of two-particle distributions as function of their relative momentum $\boldsymbol{q}$:

$$C_{\boldsymbol{K}}(\boldsymbol{q}) = N\frac{A(\boldsymbol{q})}{B(\boldsymbol{q})}. \tag{3.39}$$

Here $A(\boldsymbol{q})$ is two-particle distribution obtained from individual single events, and $B(\boldsymbol{q})$ is a two-particle distribution obtained by the so called "*event mixing procedure*". In the event mixing procedure, pairs for the distribution in the denominator are created so that each particle in the pair comes from different event. In this way the obtained two-particle distribution should be similar to $A(\boldsymbol{q})$ less the FSI effects, assuming that FSI correlation effects are the only thing in which two events differ (at least in the region of low q). This is rather strong assumption and more on this will be discussed in the Section 6.2.3.

The correlation function can be arbitrarily normalized, but usually N is chosen so that the correlation function $C_{\boldsymbol{K}}(\boldsymbol{q})$ approaches 1 for a large q. However since the experimentally constructed correlation function according to 3.39 usually contains not only correlation of FSI origin, but often also other correlations(such v_2 correlation of dynamic origin), it's a common practice to select a limited normalization region where the effects of FSI are negligible, and

yet with q low enough not to contain the dynamic correlations. This normalization region is usually at $q \sim 100 - 500$ MeV/c.

3.2.1 The λ parameter

The experimentally measured correlation functions 3.39 is in most cases by a significant factor smaller then the theoretical prediction 3.16. This leads to introduction of a λ factor so that

$$C_{\boldsymbol{K}}(\boldsymbol{q}) = 1 + \lambda[R(p_1, p_2) - 1]. \tag{3.40}$$

The λ then regulates the absolute magnitude of the correlation function. In the case of the Gaussian source such as in 3.29 the measured correlation function will change into:

$$C_{\boldsymbol{K}}(\boldsymbol{q}) = 1 + \lambda \exp\left[-q_{out}^2 R_{out}^2 - q_{side}^2 R_{side}^2 - q_{long}^2 R_{long}^2\right]. \tag{3.41}$$

The λ parameter may be of multiple origins. Initially the λ was called the "*incoherence factor*" as a coherent emission of fraction λ of pions would cause corresponding decrease in the correlations function [110]. Other cause of $\lambda < 1$ in experimental correlation function is a contamination of used pairs with misidentified particles and admixture of particles coming from long-lived resonances and weak decays which occur close to primary vertex and their decay products are hence misidentified for primary particles. These *purity effects* can be either included into the λ parameter during fitting, such as in 3.41, or the correlation function can be corrected for it by extracting the purity separately prior the construction of the correlation function.

The predictions of coherent emission of pions was tested separately via three particle correlations [115, 116] and obtained results point to fully chaotic source of pions [117]. The value $\lambda \neq 1$ in pion-pion HBT then can be taken as a measure impurities of the used pionic sample .

3.2.2 Spherical harmonics decomposition

The measured 3-dimensional correlation function $C(p_1, p_2) = C_{\boldsymbol{K}}(\boldsymbol{k}^*)$ cannot be viewed directly. To visualize the results it's usual to present only 1-dimensional projections along one of the Cartesian (*out,side,long*) coordinates with the remaining two direction integrated out over the correlation region. In the case of measurements of emission asymmetries between non-identical particles the the most common approach is to use the C_+/C_- ratio as explained in Section 3.1.4. This representation of data has its limitation as it doesn't allow full visual inspection of the data. Important features, such as the degree of non-Gaussianess can missed out or significantly distorted. In the case C_+/C_- the strength of the signal depends on the actual shape of the distribution of $\cos\theta^*$ in the $\boldsymbol{k}^*\boldsymbol{r}^*$ product which is

affected by the acceptance of the detector.

A novel technique of representing the correlation function via only few 1-dimensional plots has been suggested in [118]. This method relies on a decommission of the angular part of the correlation function into spherical harmonics. The Cartesian components of the $\boldsymbol{k}^*$ vector are related to the spherical coordinates by

$$k^*_{out} = k^* \sin\theta \cos\varphi, \quad k^*_{side} = k^* \sin\theta \sin\varphi, \quad k^*_{long} = k^* \cos\theta, \tag{3.42}$$

with $k^* = |\boldsymbol{k}^*|$. The measured correlation $C(k^*, \theta, \varphi)$ is represented as a series of the k^*-dependent $A_{l,m}(k^*)$ coefficients of the decomposition

$$C(k^*, \theta, \varphi) = \sqrt{4\pi} \sum_{l=0}^{\infty} \sum_{m=-l}^{l} A_{l,m}(k^*) Y^*_{l,m}(\theta, \varphi), \tag{3.43}$$

where $Y_{l,m}$ are the spherical harmonics. The individual coefficients are obtained as

$$A_{l,m}(k^*) \equiv \frac{1}{\sqrt{4\pi}} \int d\varphi \, d(\cos\theta) \, C(k^*, \theta, \varphi) Y_{l,m}(\theta, \varphi). \tag{3.44}$$

The equation 3.43 deals with continuous correlation function. Experimentally we construct the correlation function in finite bins with their size depending on available statistics. For the use of spherical decomposition we usually use bins in $\cos\theta$,and φ. To account for the effect of the finite binning the formula 3.43 has to be modified:

$$C(k^*, \cos\theta_i, \varphi_j) = \sqrt{4\pi} \sum_{l=0}^{\infty} \sum_{m=-l}^{l} F_{l,m}(\Delta_\varphi, \Delta_{\cos\theta}, \cos\theta_i) A_{l,m}(k^*) Y^*_{l,m}(\cos\theta_i, \varphi_j). \tag{3.45}$$

The $F_{l,m}(\Delta_\varphi, \Delta_{\cos\theta}, \cos\theta_i)$ is the correction factor for finite binning for the $\{i, j\}$-th bin of the angular part of the correlation function with the bins' width $\Delta_{\cos\theta}$ and Δ_φ. As shown in [119] the correction factor is then

$$\begin{aligned} F_{l,m}(\Delta_\varphi, \Delta_{\cos\theta}, \cos\theta_i) &= \frac{\sin(m\Delta\varphi/2)}{m\Delta\varphi/2} \\ &\frac{1}{\Delta_{\cos\theta} P_{l,m}(\cos\theta_i)} \int_{\cos\theta_i - \Delta_{\cos\theta}/2}^{\cos\theta_i + \Delta_{\cos\theta}/2} P_{l,m}(\cos\theta) d(\cos\theta), \end{aligned} \tag{3.46}$$

and the 3.44 for calculating the $A_{l,m}(k^*)$ can be approximated by

$$A_{l,m}(k^*) \approx \frac{\Delta_\varphi \Delta_{\cos\theta}}{\sqrt{4\pi}} \sum_{i,j} \frac{C(k^*, \cos\theta_i, \varphi_j) Y_{l,m}(\cos\theta_i, \varphi_j)}{F_{l,m}(\Delta_\varphi, \Delta_{\cos\theta}, \cos\theta_i)}. \tag{3.47}$$

The representation 3.45 of the correlation function may not seem to be of a big advantage

as, at first sight, wee would visualize the correlation function instead of multitude of the 1D Cartesian slice by a multitude of complex spherical projections $A_{l,,m}(k^*)$. The major advantage of the spherical projections shows up when we consider symmetries and restrictions constraining the measured correlation function. Extensive study of the symmetries of the correlation function for both identical and non-identical particles can be found in [119]. For the scope of the analyses in this thesis it important to realize that we expect basically only two coefficients to carry relevant information about the particle-emitting source. First we expect that with increasing l the coefficients are statistically diminishing if the expansion 3.45 is to have a sense at all. For a correlation function of non-identical particles measured symmetrically at mid-rapidity region we expect all $\mathrm{Im}[A_{l,m}]$ and all terms with $(l+m)$ odd to vanish due to the symmetries. From all the terms with $l = 0, 1$ which will be statistically accessible in this thesis we are left with only two: $A_{0,0}$, and $A_{1,1}$. While $A_{0,0}$ is the angle-averaged correlation function $C(k^*)$ is sensitive to the overall size of the source, the $A_{1,1}$ is sensitive to the shift of the average emission points of the two particles $\langle r^* \rangle_{out}$, as discussed in the Section 3.1.4.

3.3 Heavy ions collision models and femtoscopy

Although the Gaussian parametrization 3.27 seems to give a simple description of the source in terms of only few radii that, especially in the case of identical non-interacting particles 3.29, the physics interpretation may not be so straightforward. The measured R_{out}, R_{side}, R_{long} can not be simply identified as the sizes of the whole source. From the equation 3.32 we see that the correlation function is determined by the two particle emission function $g_{PS}(r, q)$ 3.11 which reduces due to the mass-shell constrain into $S_{PS}(\boldsymbol{r}, \boldsymbol{q})$ of 3.22. As this relative emission function depends only on $\boldsymbol{r}$ we see that what we measure is the size of region in the source that can produce two particles with close velocities at a given pair momentum P. This region is often called the "*homogeneity region*" and it's sized the "*homogeneity length*". In a scenarios with strong correlation between the particles momenta and their emission coordinates, such as the case of strong collective expansions, the size of the actually measured homogeneity region can be significantly smaller that the size of the whole source. The change(decrease) of the measured source size with the P_T, or more commonly m_T of the pair, is typical for the source undergoing rapid expansion.

For this reason it is important not only to measure the femtoscopic sizes of the source, but also to compare to models of the heavy-ion collisions that are able to produce the momenta of particles together with their freeze-out space-time coordinates. For the scope of this thesis two models are of main interest: Blast wave [74] and HYDJET++ [120]. With these models we can study effects of the underlying dynamics of the system on the measured homogeneity regions.

3.3.1 Blast wave parametrization

We know, and partly have also shown in Section 2, that many features of the heavy-ion collisions can be reproduced with the help of models based interacting bulk of matter described by hydrodynamics. However so far no model(hydrodynamic or transport) was able to fully describe all the observed features, including femtoscopic results, at the same time with physically reasonable initial conditions [109]. To circumvent this problem and facilitate the study of the freeze-out conditions of system the so called "*Blast wave model*" was developed.

Although called "model" the blast wave is a parametrization that aims to describe with a minimal set of parameters the configuration of bulk of the system at the freeze-out, providing both the four-momenta and four-coordinates of the particles. Such a parametrization allows to calculate bulk properties such as spectra, v_2 and HBT radii at the same time and also from the measured values of these observables quickly infer parameters of the model. Although the functional form of he model, as will be described later, is based on the hydrodynamic calculation, it must be stressed that the blast wave model merely tells us what the final state configuration, or one of the possible ones, of the source is in order to explain the measured data. However this model does not tell us whether this configuration is physical in the sense of initial conditions, evolution of the system and hadronization. Compared to full hydrodynamics or transport simulation this model is fast to calculate and can thus be efficiently used for fitting and study of the main features of the soft sector of the produced particles.

There are more blast wave parametrization available, but in this work by "blast wave" is meant parametrization developed by Lisa and Retiere in [74] based on hydrodynamical calculations [90]. This parametrization utilizes eight independent parameters: T, ρ_0, ρ_2, R_y, R_x, a_s, τ_0, and $\Delta\tau$. The source is described as a longitudinally boost invariant cylinder with a ellipsoidal transverse shape. The longitudinal boost invariance is represented by assumption of freeze-out occurring with a Gaussian distribution in longitudinal proper time $\tau = \sqrt{t^2 - z^2}$:

$$\frac{dN}{d\tau} \sim \exp\left(-\frac{(\tau - \tau_0)^2}{2\Delta\tau^2}\right). \tag{3.48}$$

The τ_0 parameter then corresponds to a proper average emission time, and $\Delta\tau$ sets the emission duration.

In the transverse plane the source is considered to consist of individual particle-emitting cells weighted according to

$$\Omega(r, \phi) = \Omega(\tilde{r}) = \frac{1}{1 + e^{(\tilde{r}-1)/a_s}}, \tag{3.49}$$

where

$$\tilde{r} = \sqrt{\frac{(r\cos(\phi_s))^2}{R_x^2} + \frac{(r\sin(\phi_s))^2}{R_y^2}}. \tag{3.50}$$

is a "normalized elliptical radius" defining one elliptical sub-shell of emitters. Each of the of cells is emitting particles with a thermal distribution given by the global temperature T. To describe the collective behavior of the system the cells are boosted in the direction perpendicular to the surface (under angle ϕ_b). Based on the hydrodynamical calculations this version of blast wave uses a linear flow profile where strength of the flow increases linearly with the elliptical radius $\tilde{r}$. To describe the measured values of v_2 the strength of the flow must depend also on the angle ϕ_b so that the final flow rapidity is

$$\rho(r, \phi_s) = \tilde{r}\left(\rho_0 + \rho_2 \cos(2\phi_b)\right). \tag{3.51}$$

Combining 3.48-3.51 with the assumption of local thermal emission and longitudinal boost invariance ($v_L = z/t$) gives a single particle emission function, analogous to the one used in 3.25:

$$G_S(x, P) = m_T \cosh(\eta - Y)\Omega(r, \phi_s) e^{\frac{-(\tau-\tau_0)^2}{2\Delta\tau^2}} \frac{1}{e^{P\cdot u/T} \pm 1}. \tag{3.52}$$

Here the $\frac{1}{e^{P\cdot u/T}\pm 1}$ is a Boltzmann factor describing emission of the particle with four-momentum P from a local thermalized source moving with four-velocity u. The source four-velocity is given by the transverse rapidity profile 3.51 and longitudinal boost invariance by which $\eta = \frac{1}{2}\ln\left[(t+z)/(t-z)\right]$. In cylindrical coordinate:

$$\begin{aligned} u_\mu(x) = (&\cosh\eta\cosh\rho(r,\phi_s), \sinh\rho(r,\phi_s)\cos\phi_b, \\ &\sinh\rho(r,\phi_s)\sin\phi_b, \sinh\eta\cosh\rho(r,\phi_s)) \end{aligned} \tag{3.53}$$

and

$$P_\mu = \left(m_T\cosh Y, p_T\cos\phi_p, p_T\sin\phi_p, m_T\sinh Y\right), \tag{3.54}$$

where p_T is transverse momentum, Y - rapidity, and ϕ_p - azimuthal angle of the emitted particle.

The blast wave model is quite simplistic and it has been pointed out that it misses some important features such as a relation between the time of emission and position $\tilde{r}$ [122] which is present in full hydrodynamic calculations. Despite these shortcomings the model is able to quite well describe simultaneously measurements of spectra, v_2, and HBT radii at different centralities and collisions energies. Example of such fit to the data is shown in Figure 3.3. In the case of femtoscopic measurements we can use the model to understand how the dynamically induced correlations between particles momentum and emission coordinates influence the observed homogeneity lengths. In the Figure 3.4 is shown calculation of the

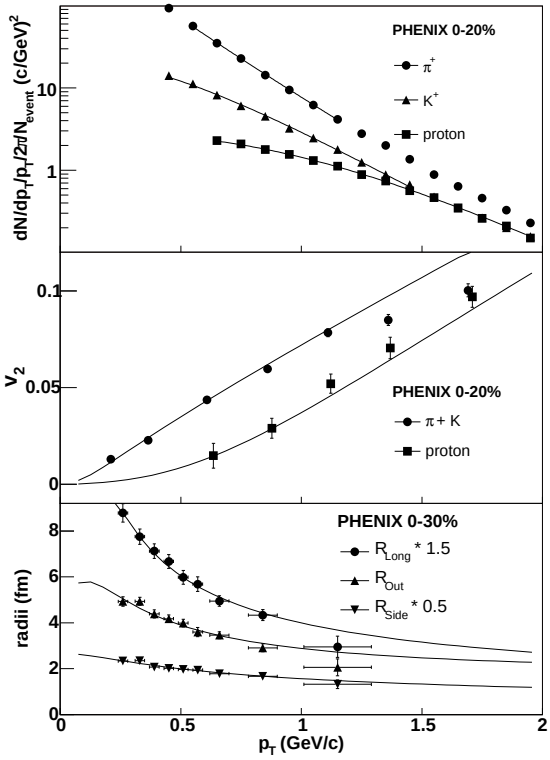

Figure 3.3: Application of the blast wave model. Simultaneous blast wave fit to PHENIX spectra, v2, and HBT data. Figure from [121].

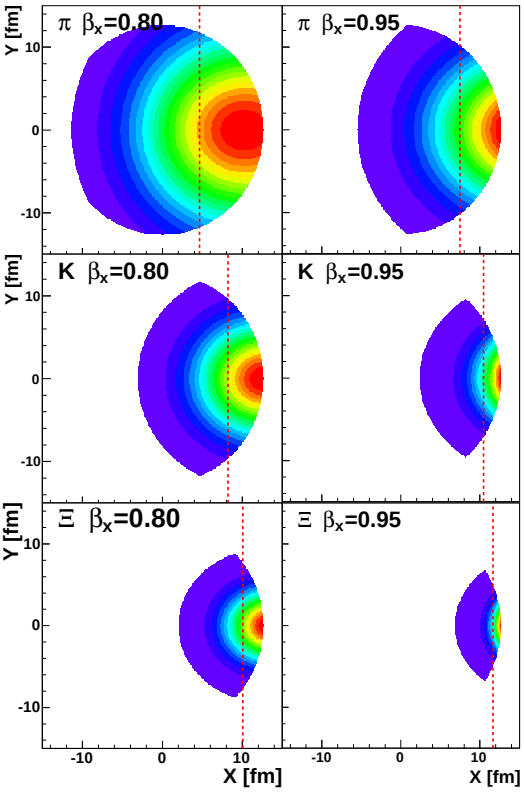

Figure 3.4: Distribution of the emission points in the transverse plane, for different particle species emitted at the same velocity, $\beta_y = 0$ and $\beta_x = 0.80$ on the left-hand side and $\beta_x = 0.95$ on the right hand side. From top: pions, kaons and Ξ. The red dashed lines shows the average emission point.

distribution of the emission points for three particle species: pions, protons and kaons emitted with the same velocity. This means $q = 0$ if the particles are paired. As can be seen due to the radial flow the particles emission point and momenta are correlated so that particles with higher momenta (mass) are emitted more on the outside of the source. The transverse expansion included in the model hence leads to a decrease of the homogeneity region and also, as shown in the Figure 3.4 by the dashed line, to the shift of the mean position of homogeneity region in the *out* direction. The one to one connection between the emission point and momentum is smeared by the thermal part of the emission function. The thermal smearing leads to a an increase of the source as the thermal motion competes with the radial flow. The effect is more pronounced for low m_T particles such as pions. Hence with the help of blast wave model we can use the measured femtoscopic radii and shifts in the emission to study the different dynamic scenarios of the system.

3.3.2 HYDJET++

HYDJET++ [120] is a further development of its predecessors: the HYDJET [123] and FASTMC [124, 125] Monte Carlo generators. It simulates Au+Au collisions as a superposition of soft, hydro-type state, and hard multi-parton fragmentation. For the work presented in this thesis we neglect the hard processes option implemented in the model because of a small influence of the high-p_t part processes on the femtoscopy data at RHIC energies and use the soft part only. Later is based on a hydrodynamical parametrization of the initial state providing the thermal hadronic state generated on the chemical and thermal freeze-out hyper-surfaces represented by a parametrization of relativistic hydrodynamics with given freeze-out conditions [124, 125]. This parametrization is in principally similar to the one described in the section above. The mean multiplicity of hadron species crossing the space-like freeze-out hyper-surface is calculated using effective thermal volume approximation. Let us note that unlike FASTMC in HYDJET++ the value of effective volume of the fireball V_{eff} is generated for each event separately. V_{eff} is proportional to the mean number of participating nucleons at the considered centrality (impact parameter b) which is calculated from the generalization of Glauber multiple scattering model to the case of independent inelastic nucleon-nucleon collisions.

The model includes not only longitudinal, radial and elliptic flow effects, but also the decays of hadronic resonances. The two- and three-body decays of the resonances with branching ratios are taken from the SHARE particle decay table [126]. This model allows to study the effects of residual correlations coming from particle decays, and resonances or to study influence of the decays on the relative space-time shift in the emission function of non-identical particles.

3.4 Femtoscopic results in heavy-ion collisions

As mentioned in the Section 2.1 the system created in the relativistic collisions of nuclei undergoes multi-staged evolution. The complex dynamics of the system imprints in the nontrivial space-time structure of the final source at the kinetic freeze-out. The extent and duration of the source carries information about the underlying physics governing the dynamics of the system and the femtoscopic measurements are the most direct way to measure such space-time characteristics.

Early theoretical predictions[107, 127, 128], which considered first order transition between the deconfined colored medium and hadronic gas stage, sparked even greater interest in the HBT measurements. It was predicted that the increased entropy associated with deconfined color degrees of freedom will lead to increased spacial extent of the source and prolonged duration of the particle emission. This is expected to manifests in a significant

increase of the R_{out}/R_{side} ratio. The HBT measurements are therefore considered to be a good candidate for diagnosing the creation of the quark-gluon plasma and its phase transition. The measurements of spacio-temporal characteristics of the heavy-ion collisions via

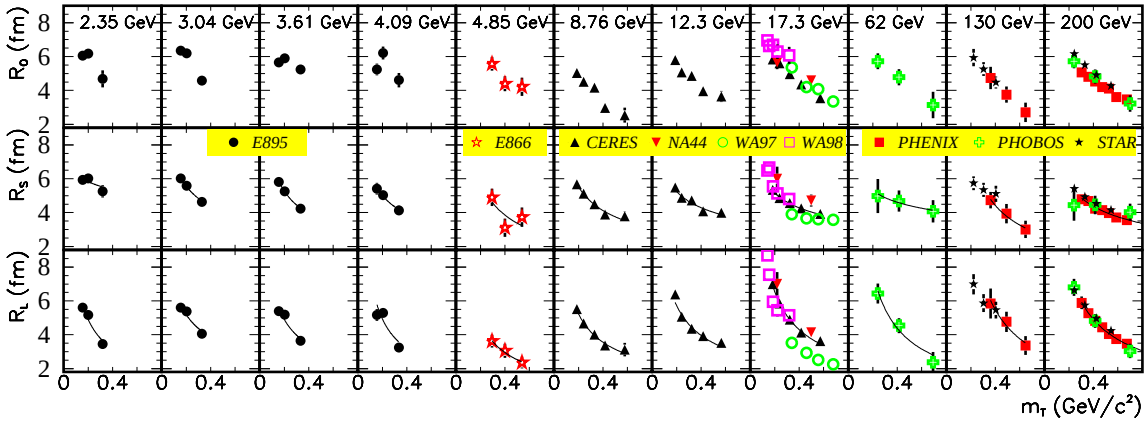

Figure 3.5: Collected data set of published m_T dependencies of pion HBT radii near mid-rapidity from Au+Au (Pb+Pb) collisions. Centrality selection is roughly top 10% most central collisions. Figure from compilation [109].

two-particle correlations has been an integral part of the heavy-ion physics program and has developed throughout experiments at AGS[129, 130, 131], SPS[132, 133, 134, 135, 136, 137], and RHIC[111, 138, 139, 140, 141] into a high precision tool.

In Figure 3.5 is shown a compilation of results from [109] on measured Gaussian radii of pion sources by different experiments for their largest colliding system and for the most central collisions. It is noticeable that systems at all collision energies show similarity in m_T evolution of the radii. The high statistics data of RHIC experiments allow to measure the m_T dependence of HBT radii with high precision for different centralities, as shown in Figure 3.6. The data of Figure 3.6 show similar m_T dependence for all centralities. The falling of HBT radii with m_T is a result of correlation in $x - p$ space of the emitted particles. A most plausible explanation for such a behavior comes from flow dominated models[142, 74, 143] where expansion creates correlations in both transverse and longitudinal direction.

It should be also noted that in the shown centrality dependence in Figure 3.6 and energy dependence in Figure 3.7 we do not observe any sudden change of behavior which would signalize an onset of different physics that could be associated with a first order phase transition from QGP. If HBT measurements are to disclose a phase transition into a new form of matter it is natural to expect same change of behavior of femtoscopic observables when collision energy at which the QGP is formed. Figure 3.7 present the excitation function of HBT radii and R_{out}/R_{side} for central collisions at low k_T bin of $\langle k_T \rangle$ $0.2 - 0.3$ GeV/c. This

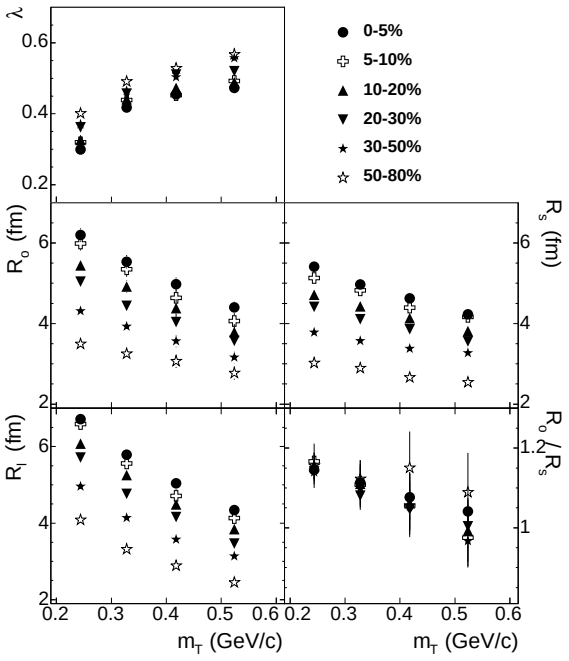

Figure 3.6: Dependence of extracted HBT parameters on m_T for different centrality bins of Au+Au collisions at $\sqrt{s_{NN}}$=200 GeVas measured by the STAR experiment at RHIC. Figure from [111].

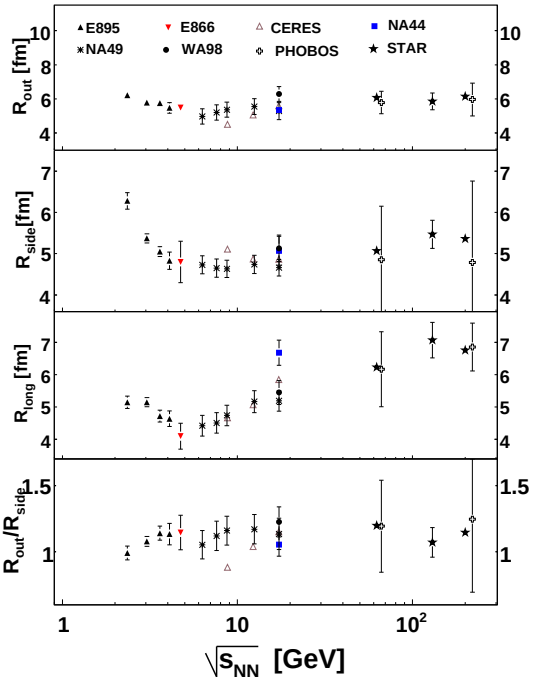

Figure 3.7: Compilation of energy dependence of femtoscopic π–πparameters for AGS, SPS and RHIC from [139]. The data are from central collisions of Au+Au and Pb+Pb at mid-rapidity and $\langle k_T \rangle \sim 0.2 - 0.3$ GeV/c.

low k_T bin contains the least amount of the dynamic $x - p$ correlations and the measured homogeneity length can be taken as a measure of the whole source. As wee can see the R_{out} in which is convoluted information about source emission duration shows almost no change with energy while R_{side} and R_{long} show an initial decrease at small collision energies with small increase later. Mainly, the closely watched R_{out}/R_{side} ratio shows only very little variation with energy of the collision as well as with centrality without any sudden increase.

3.4.1 RHIC HBT "puzzle"

For the first time, at RHIC collision energy, a substantial part of obtained results can be explained by ideal hydrodynamics models[144]. This even led to term a "perfect liquid" for the state of matter created at RHIC. The ideal hydrodynamic calculations are extremely successful in reproducing spectra and elliptic flow, but they fail in reproducing fully the available high precisions femtoscopic measurements. The data shown in Figure 3.6 show a decrease of the radii with m_T and the same behavior is expected from hydrodynamic calculation which contain collective expansion. Although, as shown in Figure 3.8, the actual

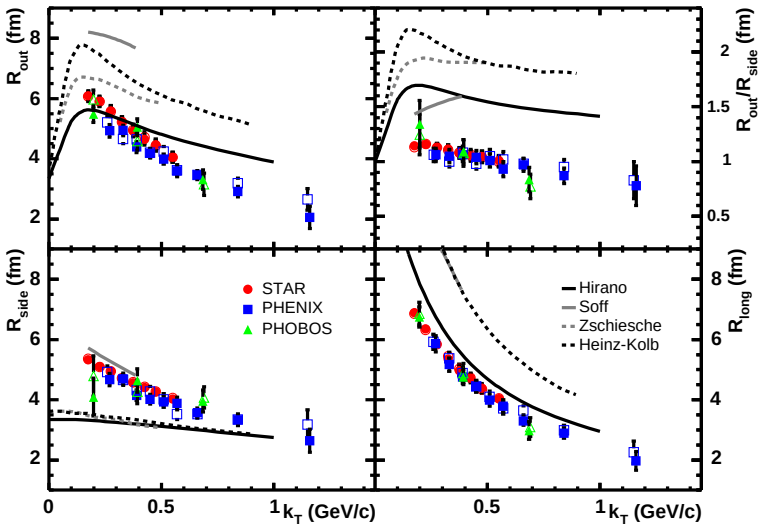

Figure 3.8: Comparison of the k_T dependence of $\pi-\pi$HBT radii and R_{out}/R_{side} ratio measured by STAR, PHENIX, and PHOBOS in Au+Au collisions at $\sqrt{s_{NN}}$=200 GeV, to the hydrodynamical and hybrid model calculations. Compilation from [109].

hydro calculations can predict the general behavior of the radii they are unable to reproduce at the same time all the radii and the R_{out}/R_{side} ratio. The measured radii are smaller than those predicted by ideal hydrodynamics. In particular, the R_{long} is abut 50% smaller than the calculated one. Also, the ratio R_{out}/R_{side} is observed to be ~ 1 while hydrodynamics gives $R_{out}/R_{side} \approx 1.3 - 1.5$. This, together with previously mentioned almost constant behavior of R_{out}/R_{side} with the collision energy, is often called the "HBT puzzle" [145, 146, 109].

Resolving of the HBT puzzle has been an ongoing task. The latest theoretical results and simulations suggested that the explanation could be an interplay of multiple components [122, 147] in which important role is played by viscous hydrodynamics[73], and proper initial conditions. Calculations where hydrodynamic evolution with thermalization is initialized very early, at about $0.5 - 1.0$ fm/c and with initial flow, achieve better description of the measured data[122].

3.4.2 Non-identical particle correlations

The above picture of the system undergoing collective expansion in longitudinal and transverse direction has been drawn from femtoscopic measurements of identical pions only, using their bosonic quantum statistics. The apparatus of correlation measurements in Section 3.1.4 allows to utilize not only identical pions, but also pairs of particles of different species. It is important to know whether similar conclusions about collective behavior of the system

can be reached from other particle species as well. Femtoscopic measurements with different species can be used to complement the measurement with pions and give a more complete and detailed picture of the dynamics of the heavy-ions collisions. Recent high statistics data

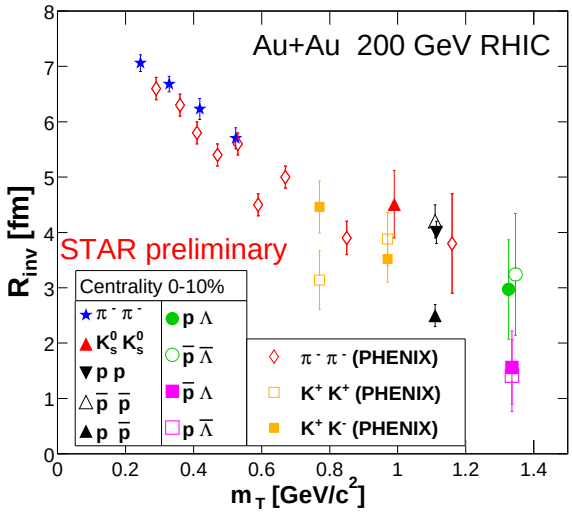

Figure 3.9: m_T dependence of R_{inv} for different particles. Figure from [148].

collected at RHIC has allowed to carry out femtoscopic analyses with precision that was unreachable before and for particle pair types that were measured for the first time. In Figure 3.9 is presented m_T dependence of 1-dimensional radii (R_{inv}=R_{out}=R_{side}=R_{long}) for different measured pairs of particles with close mass. The data shows a similar m_T fall of radii as for identical pions. It is of particular importance to note that these measurements include systems with different final state interaction and different systematical uncertainties. Using different particle species one can "turn on/off" Coulomb FSI and/or quantum statistics effects. For example, in the case of $K^0_S - K^0_S$ and $p(\bar{p})-\Lambda(\bar{\Lambda})$ the Coulomb interaction is absent and in the latter case there is also no quantum statistics. The message from common scaling in Figure 3.9 is strengthened when considering different systematics involved in each of these measurement.

Femtoscopic measurements with non-identical particles are not only sensitive to the size of the system, but also to the relative difference in the space-time position of the emission of the two particle species, as described in Section 3.1.4. Models that include collective expansion predict a relation between the average emission position and the mass of the particle such as that particles with higher m_T are emitted more on the outside of the expanding fireball [74]. This effect hence increases with a mass difference within the measured particle pair. Figure 3.10 shows that in heavy-ion collisions the average emission points of particles with different mass, such as pions, kaons and protons, are significantly shifted with respect to each other [150, 149]. The species-independence of the m_T scaling of HBT radii together with

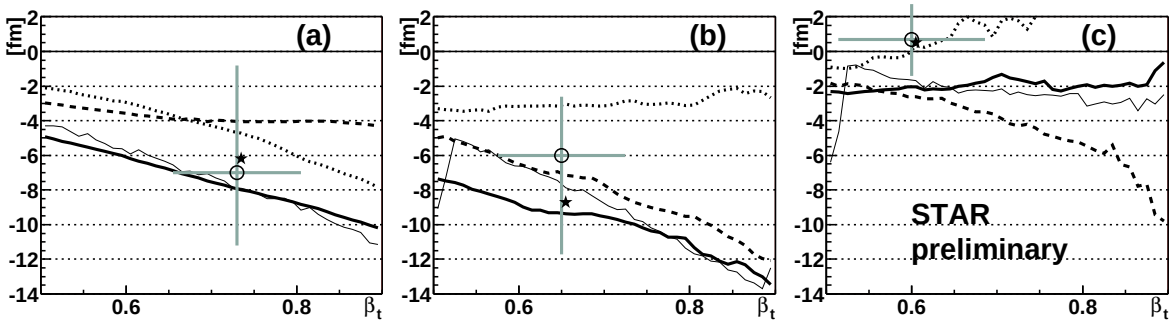

Figure 3.10: Comparison of the shift of the average emission point between (a) pion-kaon, (b) pion-proton and (c) kaon-proton. The real data (○) are compared with model predictions: blast wave parametrization [74](thin solid line) and RQMD(thick solid line). A space $\langle \Delta r_{out} \rangle$ and time $\langle \Delta t \rangle$ component of the shift are presented by dotted and dashed line respectively. The results of the fit to the RQMD simulations are shown as $\star$ symbols. Figure from [149].

extracted emission asymmetries among the particles provide an independent confirmation of a transversely expanding particle source in heavy-ion collisions.

Chapter 4

The STAR experiment at Relativistic Heavy-Ion Collider

Brookhaven National Laboratory (BNL) at Long Island has been for six decades on a forefront of nuclear and particle research. Many important discoveries were achieved at BNL and five of them have actually been awarded a Nobel Prize. Out of these five, three were earned for a research conducted at an Alternating Gradient Synchrotron (AGS). The AGS is an accelerator build at BNL in 1960 and it is a first machine that employs a strong focusing of the particle beam. This concept [151] allows to focus the beam in both the horizontal and vertical plane at the same time by successively alternating inward and outward magnetic field gradients. This breakthrough concept helped to overcome limitations of the previous Cosmotron accelerator and the AGS became until 1968 the highest energy accelerator in the world.

Since in experiments with single beam and fixed target most of the energy stored in the beam is carried away in a form of the kinetic energy of the whole colliding system, it is of advantage to use two intersecting storage rings to accelerate and collide particles. A project called Relativistic Heavy Ion Collider(RHIC) to build such an accelerator for colliding two beams of heavy nuclei was proposed in 1984 for which the older AGS would serves as an injector. The construction was started in 1991 and first Au+Au collisions were delivered in summer of 2000 at energy of $\sqrt{s_{NN}}$=62 GeV. In 2001 RHIC has reached its designed nominal energy of $\sqrt{s_{NN}}$=200 GeV. Since then the RHIC is the only accelerator facility in the world which is fully dedicated to high-energy heavy ion research and continues in the legacy of the AGS as one of the worlds prime nuclear physics experimental facilities.

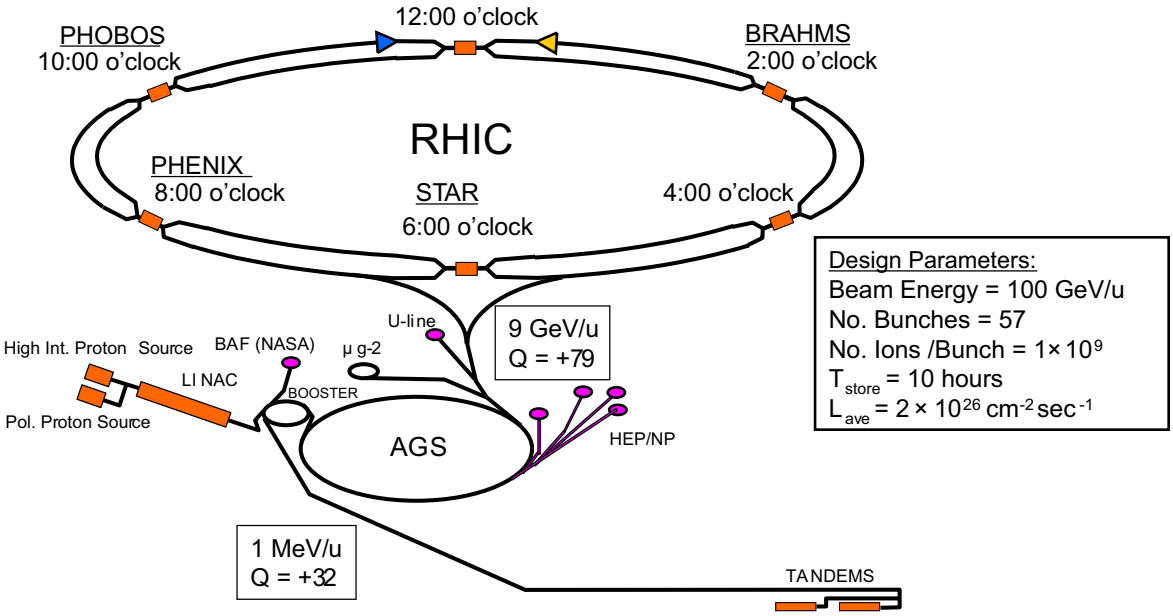

Figure 4.1: Layout of the RHIC complex at BNL - schematic drawing.

4.1 The Relativistic Heavy Ion Collider

The first registered Au+Au interaction in the summer of 2000 has been a result of two decades of scientific and engineering effort that can be approximately traced back to year 1983 [152] when U.S. Nuclear Science Advisory Committee (NSAC) suggested that the highest priority goal for the field of heavy-ion physics is to build an ultra-relativistic heavy ion collider with energy of $E/A \gtrsim 30$ GeV in the center of mass with a broad range of accelerated nuclei from light species up to uranium. A unique opportunity arose at the same time when an ill fated Colliding Beam Accelerator (ISABELLE/CBA) project, the 400 GeV on 400 GeV proton collider at Brookhaven, was abandoned in 1981 due to technical problems with superconducting magnets in favor of, later also canceled, SSC collider (at that time actually called Desertron). It was proposed to reuse much of the already existing civil engineering structures and ^{4}He refrigeration system for superconducting magnets, for the new heavy-ion machines. The Relativistic Heavy Ion Collider (RHIC) was designed [153] to accelerate nuclei to top energy of 100 GeV/A for $A \gtrsim 200$ where a fully developed mid-rapidity net-baryon free region was expected, and at the same time being able to go continuously as low as 5 GeV/A with species from almost full periodic table. This design allows to run p+p and d+A collisions, as well as A+A, and be able to study the onset of new collective physics with increasing size of the projectiles and collision energy with the same detectors. Also, the capability of colliding protons has enabled the development of polarized proton beams for the RHIC spin program.

Figure 4.2: top: Magnets of the AGS accelerator. bottom: Inside of the RHIC tunnel.

The design of the RHIC facility builds on existing accelerator architecture at BNL. It utilizes previously build Tandem Van de Graaff (TVDG) Facility, Booster Synchrotron and the AGS, which already run a heavy ion program of their own since 1986 [154]. The nuclei undergo multiple stages of acceleration as they pass through the RHIC complex, as shown in Figure 4.1:

Tandem Van de Graaff was build in he mid 1960s by High Voltage Engineering Corporation (HVEC), a company founded by J. Van de Graaff himself. It was for many years the world's largest electrostatic accelerator. The facility consist of two end-to-end aligned accelerators that use Pelletron charging system [155]. The Tandems can provide beams of different types of ions ranging from Hydrogen to Uranium [156]. After upgrades of both of them and addition of a bypass line [157] each of them can operate at a maximum terminal voltage of 14 MV and serve as a source of ions for RHIC, while the other acts as spare or delivers beam to local target rooms for an outside user program. This setup is key when collisions of unequal species in RHIC are required, such as d+Au physics program in years 2003 and 2008 [158, 159, 160] when not only good beam is needed but the whole system has to quickly switch between different setups.

In the case of Au nuclei [161], the negative ions (Au^{-1}) are produced by a pulsed

sputter source [162] and accelerated from ground potential to +14MV at the center terminal of the Tandem. At this point they pass through a thin stripping foil which predominantly removes 13 electrons creating Au^{+12}. The beam is then accelerated back to the ground potential and passes through a second stripper foil which removes electrons to Au^{+32} or Au^{+31} charge state before it enters the transfer line.

Heavy Ion Transfer Line (HITL) was completed in 1986 to allow the Tandem Van de Graaff to serve as a heavy ion source for high energy collisions. Beam with energy of ∼1 MeV/nucleon and typical intensity of 5×10^9 per pulse is transported via ∼840 meters long tunnel from the Tandem to further stage of acceleration that takes place in AGS Booster. Transport efficiency of the entire line ranges from 80 to 90%.

The Alternating Gradient Synchrotron Booster was begun in 1986 and completed in 1991 with the aim to allow acceleration of ions heavier than Silicon in the AGS [163]. The Booster is 202 m long - less than one quarter the size of the AGS. Because of high rates of electron pick-up and loss for partially stripped ions in the residual gas of AGS only fully or almost fully stripped ions can be accelerated in the AGS ring. Without the Booster only nuclei up to the Silicon can be fully stripped before being injected to the AGS. Higher energy is needed to strip heavier nuclei with sufficient efficiency. Booster, because of its superior vacuum, is able to further preaccelerate the partially stripped nuclei. In the Booster nuclei are accelerated to 101 MeV/nucleon. After extraction from the booster the beam is passed through a stripper in the Booster to AGS (BTA) transport line where approximately 60% emerge in charge state Au^{+77} - state with only two remaining K-shell electrons.

Linear Accelerator (Linac) was build 1960 and is used as a source of protons for the study of p+p collisions at the experiments. It consists of hydrogen gas ion sources, radio-frequency quadrupole pre-injector, and nine accelerator radio-frequency cavities which accelerate the protons along total length of a 150 m. The Linac is capable of producing up to a 35 milliampere proton beam at energies up to 200 MeV which is injected into the AGS Booster.

AGS The AGS is filled with bunches of Au^{+77} ions from the Booster. Four cycles of Booster with 6 bunches per fill are needed to fill the AGS [161] (note that the circumference of the Booster is $\sim 1/4$ of the AGS). To satisfy the beam intensity requirements of the RHIC the beam in the AGS has to be rebunched from 24 to only 4 bunches [161]. Each of the these bunches holds number of ions equivalent to one Booster filling and the bunch then exists throughout the whole RHIC cycle. The four bunches in the AGS are accelerated to the RHIC injection energy 8.86 GeV/nucleon ($\gamma = 10.52$) with an intensity $\sim 1.5 \times 10^9$ ions per bunch.

ATR After extraction from AGS, the bunches are transported to the RHIC via AGS-to-RHIC Transfer Line (ATR). Final stripping of the last two remaining electrons to Au^{+79} state occurs during the transfer. At the end of this line the beam is split and injected into two counter-rotating beams of the RHIC.

RHIC

The proposal [153] and design [164, 165] of the RHIC was driven by physics objectives of the heavy-ion experimental program as well as the requirement of utilizing already existing accelerator infrastructure at the BNL site. The primary requirement, by which RHIC differs from "typical" hadron collider, is to operate with beams of different energies in order to connect with previous heavy-ion experiments. Another major requirement non-existent in other colliders is to provide collisions for non-identical particles species ranging in the mass from proton to Uranium. For such a task the complexity of magnetic optics dictates a design based on two essentially separate rings capable of operating at different settings.

The collider consists of two concentric rings of super conducting magnets. Each of the rings has circumference of 3.8 km. The main component of the collider are 9.7 meters long superconducting dipole magnets that provide a magnetic field up to 3.5 Tesla. There is total of 288 such dipoles plus large number of additional magnets used for steering of the beam, totaling 1740 magnets. The magnets are enclosed in vacuum vessel's separately for each ring. These magnets are cooled to a temperature of 4.6 K by liquid Helium. The price of cooling and keeping the magnets at such a low temperature is the main cost associated with operation of the RHIC since the cooling system consumes 21 MW of electricity.

As shown in Figure 4.1 the two rings are identified as yellow and blue. The beam in the blue ring travels in the clockwise direction and counter clockwise in the yellow ring. The two beams are steered to intersect at 6 crossing points along the ring. Four of these crossing are actually used for physics experiments . The adoption of the beam transfer from the AGS to RHIC in the single bunch mode allows considerable freedom in the filling pattern. The minimum number of bunches is six, if collisions at all interaction points are wanted. The fewer buckets that are filled, the easier it is to accelerate and keep the beam stable as there are less intra-beam effects. RHIC can handle a maximum of 360 buckets in each ring, although it usually runs a factor 3 or 6 fewer. The nominal case with 60 bunches corresponds to a bunch spacing of 63.9 m. The stored beam lifetime for gold in the energy range of 30 to 100 GeV/nucleon is approximately 10 hours. The top kinetic energy is 100+100 GeV/nucleon for gold ions. The operational momentum increases with the charge-to-mass ratio, resulting in kinetic energy of 125 GeV/nucleon for lighter ions and 250 GeV for protons. The collider is designed for a Au+Au luminosity of about $2 \times 10^{26} cm^{-2} s^{-1}$ at top energy. The luminosity is energy dependent and decreases with the operating energy. For lighter ions it is significantly

higher reaching $1 \times 10^{31} cm^{-2} s^{-1}$ for p+p collisions.

4.2 STAR experiment

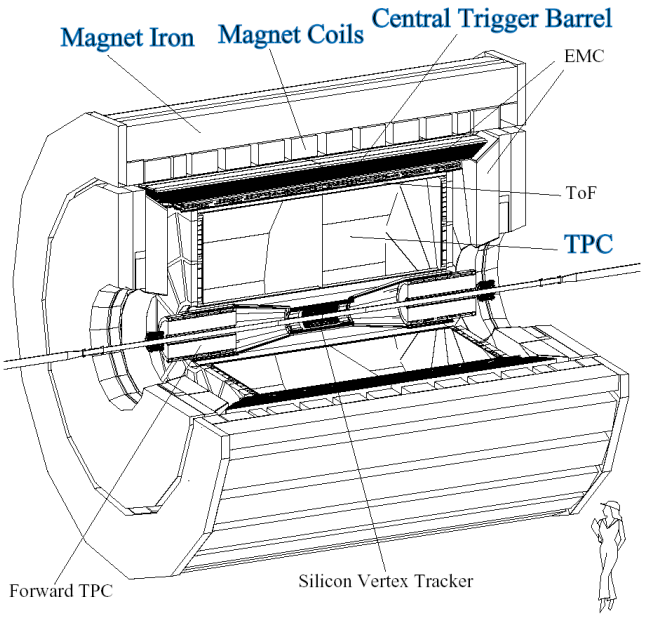

Figure 4.3: Schematic view of the STAR detector.

The STAR stands for **S***olenoidal* **T***racker* **A***t* **R**HIC [166, 167]. It is one the two large detector systems (together with PHENIX) constructed at the RHIC collider facility. It was designed [168] as a multi-purpose detector with the aim to measure hadronic observables over a large solid angle and to study global observables on an event-by-event basis. The versatility of the STAR detector is of a great importance as it is unlikely that there is any single definitive signature for the QGP. It is essential to measure multiple observable signals and build a self-consistent description of the matter created at RHIC; it's properties, signatures of the phase transition and space-time evolution of ultra-relativistic heavy ion collisions.

The baseline configuration of the STAR detector as it was set up for Run-4 (2004) is shown in Figure 4.3. It is a system of concentric subdetectors inside of a large room-temperature solenoidal magnet [169]. The magnet creates uniform field of 0.5 T that allows to measure particle momenta from the curvature of the tracks.

For collisions that occur at the center of the detector the particles first pass trough the Silicon Vertex Tracker (SVT) [170]. It is a tracking device for low p_T particles and reconstruction of secondary vertexes close to the collision vertex. It is composed of three

layers of silicon drift detectors. Upgrades after year 2004 include currently installed SSD detector [171] which provides a fourth layer of the inner tracking system. The SSD is double-sided strip detector which main aim is to improve extrapolation of tracks from the main detector towards the SVT. The inner detectors cover a pseudo-rapidity range $|\eta| \leq 1$ with full azimuthal coverage.

The main tracking detector of STAR is a Time Projection Chamber (TPC) [172, 173]. It provides tracking for charged particles at mid-rapidity $|\eta| \leq 1.8$. It is also the main detector used for identification of particles via ionization energy loss (dE/dx). As this is the single most important detector for the analysis of this thesis it is described in more detail in the following section. To extend tracking of particles to forward rapidities STAR has installed radial-drift Forward TPCs (FTPC) [174]. They cover the region of $2.5 < |\eta| < 4$ in pseudo-rapidity with full azimuthal coverage as well. Since particle identification by dE/dx in drift chambers is limited to low p_T in order to extend the identification to higher p_T STAR has installed in 2009 full barrel Time Of Flight (TOF) detector [175].

STAR also possesses calorimetric capabilities. At present time STAR has two electromagnetic calorimeters that are used to detect photons and electrons and are also used for triggering. The Barrel Electromagnetic Calorimeter (BEMC) surrounds the TPC and covers $|\eta| < 1$ in pseudo-rapidity. In forward section of the detector is positioned The Endcap Electromagnetic Calorimeter (EEMC). It has full azimuthal coverage and $1 < \eta < 2$ in pseudo-rapidity. Both of these detectors include high granularity shower-maximum detectors to distinguish high momentum single photons from photon pairs coming from π^0 and η meson decays. The fast response of the calorimeters can be utilized against pileup of tracks in TPC coming from untriggered events in the high luminosity $p + p$ collision.

STAR as a multi-purpose detector has a wide range of triggering options given by its range of fast response detectors [176]. The data used in this work were collected using trigger signal from three subdetectors. These detectors are Central Trigger Barrel (CTB), Zero-Degree Calorimeters (ZDC), and Beam-Beam Counter (BBC).

The Central Trigger Barrel (CTB) is an array of 240 scintillator slats which is arranged around the TPC with coverage $|\eta| < 1$. The CTB is used for measuring the multiplicity of charged particles at mid-rapidity. The Zero-Degree Calorimeter ZDC [177] is a hadronic calorimeter sensitive to the fragmentation neutrons from the collision. There are two ZDCs located at $\pm 18m$ from the detector center with angular acceptance of $|\sin\theta| < 0.002$. The signal from ZDCs is used in the coincidence with the CTB for triggering. Both the ZDC and CTB can be used for computing the centrality of the event. In p+p collisions the ZDC cannot be used for its small acceptance. Instead, an addition detector, Beam-Beam Counter (BBC), is used. The BBC comprises of two scintillator detectors positioned at each side of the detector at 3.5 m distance from the interaction point covering $3.3 < |\eta| < 5.0$. The coincidence of the BBC signals is used in Au+Au trigger to better constrain the position of

the collision vertex.

4.2.1 TPC

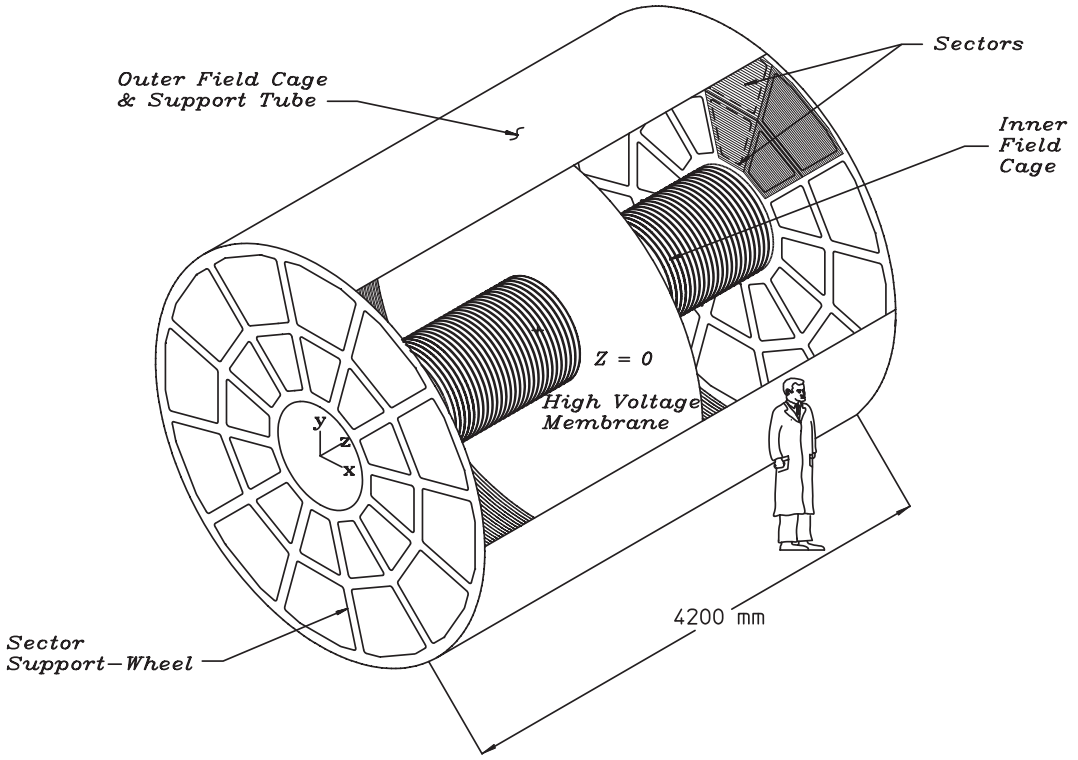

Figure 4.4: Diagram of the TPC field cage. Figure from [173].

The STAR TPC [172, 173] is one of the largest detectors of its kind ever built. The active volume of TPC is a 4.2 m long barrel with 0.5 m inner and 4 m outer diameter. For collision occurring at the center of the detector TPC covers pseudorapidity interval of $|\eta| < 1.8$ with full azimuthal coverage. The TPC is filled with P10 gas (10% Methane, 90% Argon) in which traversing particles leave ionization trail. The tracking volume is split in two, along the beam direction, with a high voltage cathode located at the center of the TPC. The cathode membrane is held at 28 kV and divides the detector into two separate drift regions. The electric potential is gradually decreased toward the end cap via chain of 183 precision 2 MΩ resistors on the inner and outer field cage. This ensures the uniformity of the electric field of 135 V/m in which the ionization electrons drift toward one of the sides with a velocity of 5.45 cm/μs. The maximum drift time is hence ~ 40 μs.

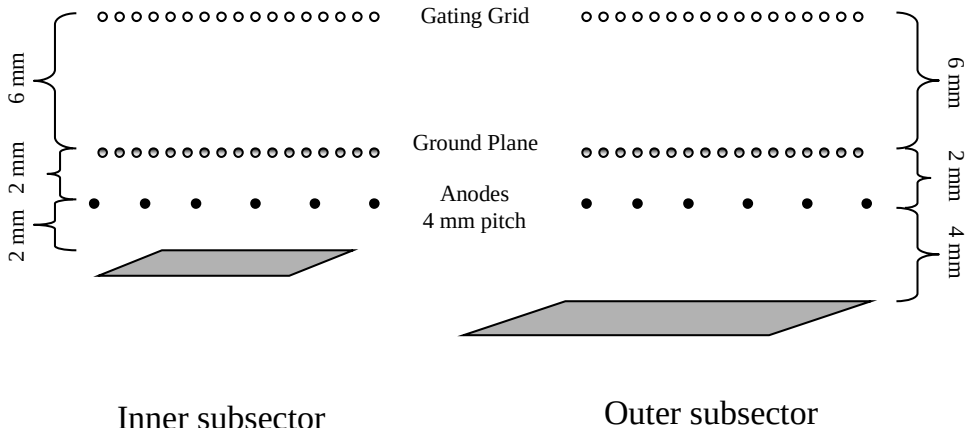

Figure 4.5: Schematics of the read-out part of the TPC endcaps. Figure from [178].

At both ends of the TPC are amplification/readout regions which work on the principle of Multi Wire Proportional Chambers (MWPC). As shown in the Figure 4.5 there are tree sets of wires called the *gating grid*, the *ground plane* and the *anode plane* plus an array of readout pads positioned behind the anode wires. The purpose of the gating grid is to prevent electrons from untriggered events from entering the amplification region as well as not to allow any created positive ions to enter the drift region. The wires of gating grid are positioned 6 mm in front of anode MWPC anode wires and separated by 1 mm. When an event is triggered the gating grid is set to potential of the surrounding material by do so it allows the drifting electrons to pass to MWPC. When the grid is in the closed state, the wires are alternately held at $+75$ V and -75 V from the equipotential value. The ground plate terminates the drift region of the TPC and collects the positive ions created in the amplification region. Once the drifting electrons pass ground plate they continue toward the anode wires which are held at highest positive potential (over 1 kV). The anode wires are spaced 4 mm apart and create region with a high gradient electric field. This causes the electrons to accelerate toward the anode wires and further ionize the surrounding gas developing a avalanche of electrons reaching the wire. The avalanche at the MWPC anode wires amplifies the signal $1000 - 3000$ times. The positive ions created in the avalanche induce signal on the readout pads, which then passes through preamplifier/shaper/digitizer system. Since the signal is induced not only on the closest readout pad, but also on the

neighboring pads the position of the hit can be reconstructed with higher precision then size of the pad.

Each end-cap of the TPC is divide into 12 pie-shaped sectors and each of theses sectors has a different layout in inner and outer part in order to cope with a higher track density at the inner region. The STAR TPC was specifically designed with the high track density of the heavy-ion collisions in mind. The total number of readout pads ($\sim 137,000$ channels) is a lot higher that in TPCs used in elementary particle collision experiments allowing to do efficient tracking and dE/dx identification in an environment of ~ 2000 tracks.

Particle Identification (dE/dx) and tracking

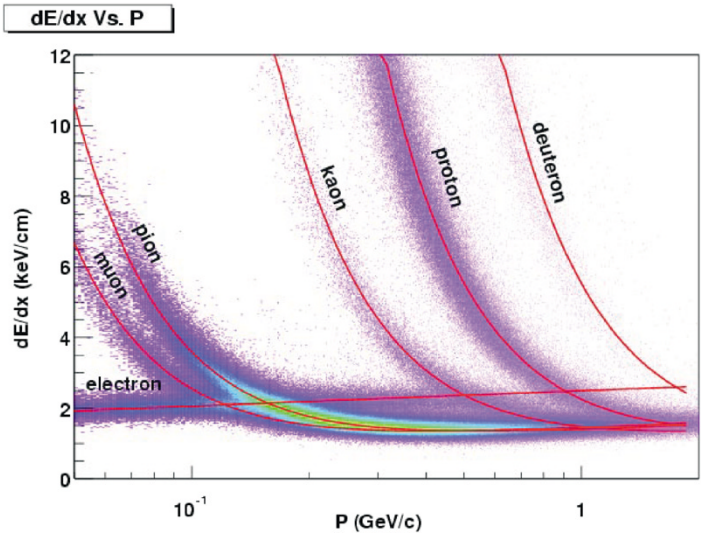

Figure 4.6: Measured specific ionization (dE/dx) in the STAR TPC. Figure from [173].

When charged particle passes through the active volume of the TPC the energy that it looses by ionization per the path length dE/dx is characteristic for a particle of given mass, charge and velocity. The mean energy loss of a particle traversing a matter is described by the Bethe-Bloch equation:

$$-\frac{dE}{dx} = \frac{4\pi}{m_e c^2}\frac{nz^2}{\beta^2}\left(\frac{e^2}{4\pi\epsilon_0}\right)^2\left[\ln\left(\frac{2m_e c^2\beta^2}{I(1-\beta^2)}\right) - \beta^2\right]. \tag{4.1}$$

Here z is the charge of the particle, β its velocity, n is the electron density of the target and I is a mean excitation potential of the target. The energy loss measured by the STAR TPC together with the theoretical calculations is in Figure 4.6. As can be seen the dependence of the dE/dx on the velocity of the particle is such that it allows to distinguish particles, at certain ranges of p, once their momentum has been measured.

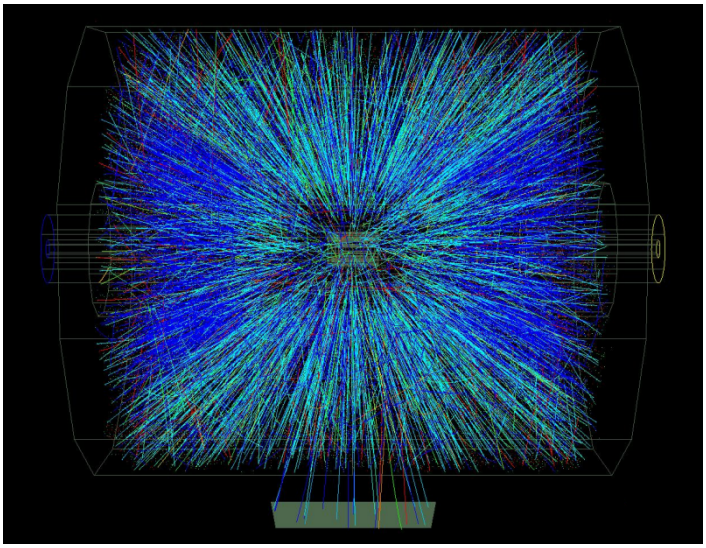

Figure 4.7: Tracks of charged particles from a central collision of two gold atoms at $\sqrt{s_{NN}} = 200\ GeV$ that were recorded by the Time Projection Chamber of STAR.

In the event of Au+Au central collision, such as the one shown in Figure 4.7, over 1000 charged particles leaves ionization hits in the TPC. The individual hits are recorder and later, during reconstruction, the paths of individual particles must be deduced and separated from each other by grouping the hits into the respective tracks. The momentum of the passing particles is calculated from the curvature of the tracks in the magnetic field of the magnet. The precision of the momentum measurement depends on the transverse momentum of the track. The higher is the p_T of the particle the straighter is the track in the TPC and it is hence harder to measure the curvature of the track. On the other hand the low p_T particles have higher ionization loss and loose significant part of their energy as they pass through the TPC gas which significantly distorts the helical shape of the track. The low p_T particles also traverse only small part of the volume of TPC thus leaving smaller number of hits from which the track can be reconstructed. Typical resolution for majority of detected particles is $\Delta p_T/p_T \sim\ 2-4\%$.

Chapter 5

STAR Silicon Vertex Tracker

To extend STARs capabilities to the low p_T region a Silicon Vertex Tracker (SVT) [179, 180, 181] is installed as the innermost detector in the mid-rapidity region. The SVT detector not only extends the detectors acceptance for low p_T phenomena, but it also enhances the capabilities of STAR detector in areas where the TPC performance is improved by combining the SVT and TPC measurements. It improves the main vertex position resolution which is especially useful in low multiplicity events. It should also enhance the ability to reject multi-vertex events.

At high p_T the momentum resolution of TPC is restricted by its position resolution ($\approx 700\mu m$), which limits the determination of the curvature of these nearly straight tracks. SVT provides accurate position information near the main vertex, thus may be used for improving the resolution of high p_T tracks.

The improved accuracy of the combined TPC-SVT tracks allows searching for short-lived particles with cτ decay lengths of several hundred microns, such as the B (cτ = 122.9 μm) and D (cτ = 311.8 μm) mesons [182].

The femtoscopic analyses in this thesis was expected to benefit from the improved reconstruction of secondary Ξ vertexes as well as from extending the pion sample to lower p_T region which would results in higher number of $\pi-\Xi$ pairs in the region of low k^*. In the end the information from SVT was not used for this work due to calibration and alignment problems of its first data run which we use. These problems were successfully solved in the following runs and the SVT is now utilized in measurements, such as those in [182].

5.1 SVT setup

The SVT consists of 216 silicon drift detectors (SDD) mounted on the three concentric barrels; see schematic layout of the SVT is shown in Figure 5.1. The detector is designed to cover pseudorapidity region $-1 < \eta < 1$ while minimizing the number of used silicon wafers.

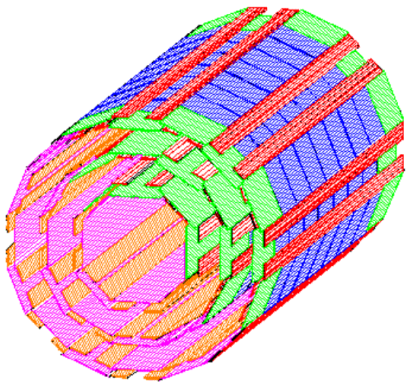

Figure 5.1: The schematic layout of the SVT.

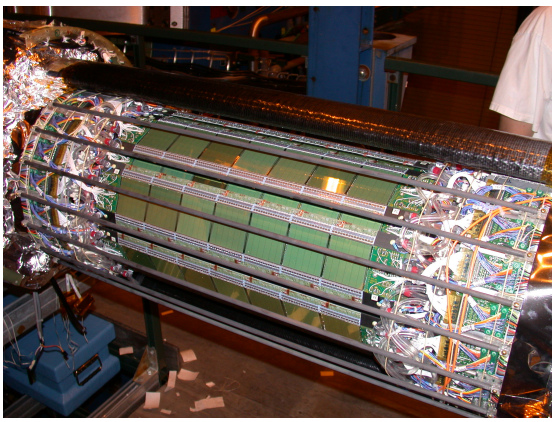

Figure 5.2: Photo of the STAR Silicon Vertex Tracker.

Barrels consist of 6,12 and 16 ladders which carry different number of the SDDs. The inner layer ladders carry 4 SDDs, the middle ones 6, and the outer ones carry 7 SDDs. Each barrel consist of two "sub-layers" which are tiled with respect to each other to minimize dead areas. The detector has an active length of 42 *cm* and a diameter of 30 *cm*. The geometrical specifications are listed in Table 5.1.

length of active area	42 cm (max.)
inner barrel radii	5.97 cm
middle barrel radii	10.16 cm
outer barrel radii	14.91 cm
number of wafers	216
inner barrel	32 (8 × 4)
middle barrel	72 (12 × 6)
outer barrel	112 (16 × 7)

Table 5.1: Geometrical specifications of the SVT.

The ladders are made of Beryllium frame to which are epoxied the silicon wafers. The front-end electronics for each ladder are epoxied on carbon-fiber electronic carrier that contains small channel trough which flows water in order to sink the heat created from the electronics. The ladders and electronic carriers are supported at each end by two Beryllium end-caps.

5.2 General principles of silicon drift detectors

Silicon drift detector (SDD) could very shortly be described as "solid state TCP". These detectors combine some of the main advantages of the normal gas drift chambers - small

number of readout channels and the advantages of solid state detector ,such as the excellent position and energy resolution. They operate in a fashion similar to conventional drift chambers, but the gas is replaced by n-type silicon, as first proposed by Rehak and Gatti[183].

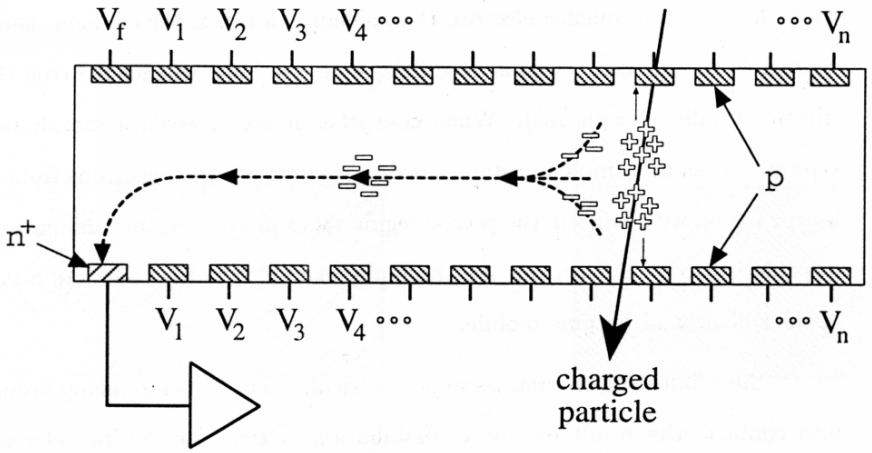

Figure 5.3: Schematic principle of the silicon drift detector. Figure from [184].

Schematic drawing of the silicon drift detector is shown in Figure 5.3. The detector is made of thin n-type semiconductor wafer of a thickness of $\sim 300\ \mu m$. There are $P+$ cathode strips implanted symmetrically on both sides of the wafer. At the end of the wafer there are placed segmented $N+$ read-out anodes.

The detector can be seen as two back-to-back p-n junctions operated at a reverse bias. This creates a region depleted of mobile charge carriers which is the active region of the detector. If there is no voltage applied the depleted region is only under the p-type cathodes leaving the rest of the n-type bulk conductive. This conductive area can carry thermally generated electrons that create a noise in the detector. By increasing the negative potential at both p-type sides the depleted region can be extended further to the n-type bulk. With a sufficiently large potential the whole detector can be fully depleted with a maximal potential of the electric field in the middle of the wafer. With this potential, any electrons created by incident particles inside of the depleted region will be confined in the middle of the n-type silicon bulk.

In order to read the signal, the excited electrons have to be brought to the collecting anodes at the end of the wafer. It is done by superimposing a linear potential parallel to the surface with the parabolic potential that holds the electrons in the bulk. The linear potential is created by gradual increase in the bias potential on the cathodes on both sides of the wafer. This creates the linear electric field in the drift direction. Typical field strengths used for drift detectors are from 200 V/cm to 800 V/cm.

In the focusing region of the detector the drifting cloud of the electrons has to be brought

to the surface to the collecting anodes. This is done by applying different bias potentials at opposite sides of the wafer. The minimum of the potential valley is this way gradually shifted from the center of the bulk toward the anode. The shape of the potential inside of the detector in the drift region and in the focusing region is shown in the Figure 5.4.

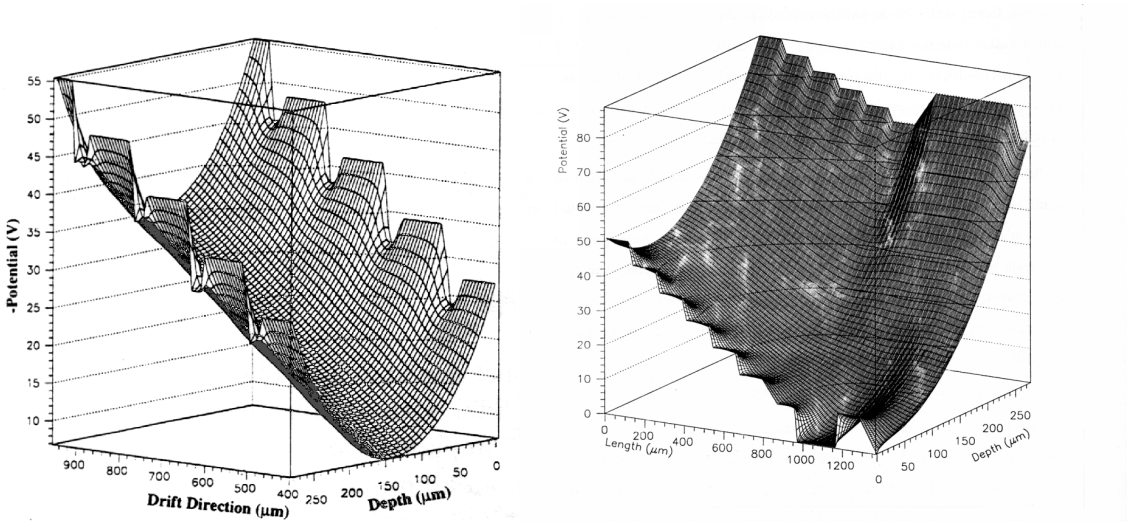

Figure 5.4: The electric potential in left: drift region and right: focusing region of the silicon drift detector.

The *drift velocity* v_{drift} with which the free electrons drift inside of the n-type bulk

$$v_{drift} = \mu E, \tag{5.1}$$

depends on the applied electric field E and on the the *electron mobility* μ. If the bulk of the silicon is without non-uniformities in doping, the electron mobility is constant. For an applied constant electric field the drift velocity is constant as well. Hence from measuring the drift time it is easy to obtain the drift distance. The position of the hit on the axis perpendicular to the drift is measured by the position of the anode that collected the drifting charge. As the cloud of the electrons drifts toward the anodes it spreads due to diffusion and Coulomb repulsion. This causes the signals to appear on more that one anode. The exact position of the hit can then be calculated with better precision than is the pitch of the anodes.

5.3 STAR-SVT SDD design

The SDD detectors used in STAR-SVT are made of 280 μm thick silicon. The detector's size is 63 $mm \times 63$ mm. It's divided into two half-detectors with opposite direction of drift by the so called "continental divide", the central cathode that receives the maximum voltage

bias. This design allows the detector to work with smaller maximum voltage which helps to keep the drift speed constant, because in the used electric field the electron mobility is well independent of E. Also the spread of the drifting electron cloud is smaller due to the shorter drift distance. This increase of precision is at the cost of doubling the number of readout channels and electronics.

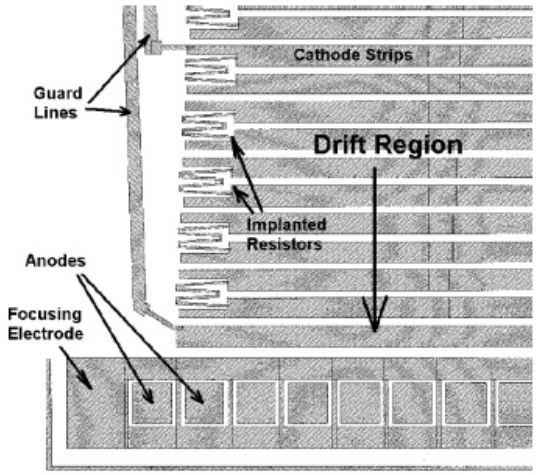

Figure 5.5: Detail view of the corner of the SDD used in STAR. Figure from [179].

At the ends of both drift directions are the readout anodes of a size 200 $\mu m \times 200 \mu m$ at a pitch of 250 μm. In each drift direction, there are 220 p^+ cathode strips implanted on both surfaces with a spatial pitch of 135 μm to maintain the linear drift field inside the bulk. The adjacent cathode strips are connected with the "M" shaped resistors to create the gradual decrease of the bias potential. On the lateral side the *guard lines* connect to every 10th cathode of each half-detector. These lines connect each 10th cathode of one half-detector to that of the other half. It means that only one half of the detector needs external bias and the other half is biased automatically. The guard lines also create the necessary *guard area* that controls the voltage gradient from the high-voltage center of the detector to the sides of the silicon wafer. The guard area is minimized so that the active area of the detector covers 94.5% of the detector. A detailed view of a corner of the SDD showing the above mentioned features is in Figure 5.5.

5.4 SVT Slow Simulator

Correction of the measured data for the effects connected with the behavior of the used detectors are integral part of almost every analyses. Understanding the detector and its response to the passing particles is hence crucial. In this chapter is presented results of

development of the so called *Slow Simulator* of the STAR Silicone Vertex Tracker. This simulator is based on the physics principles of behavior of exited electrons in the drift detector and it sequentially simulates individual components of the detector.

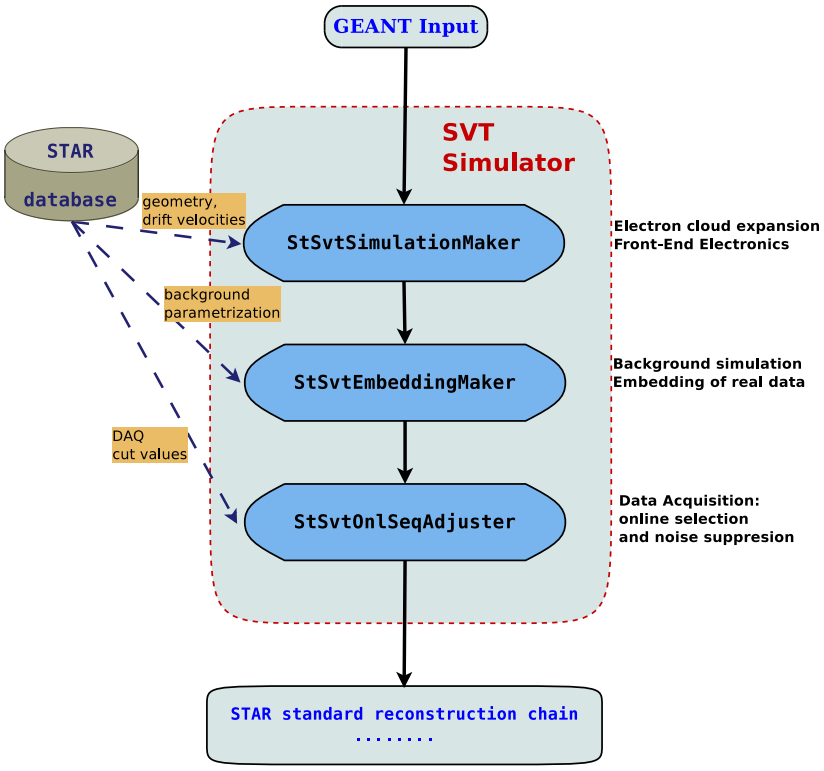

Figure 5.6: Schematic diagram of the STAR SVT Slow Simulator.

A block schema of the simulator is shown in Figure 5.6. The simulator consist of three main components (so called "*Makers*" in STAR software terminology). They will be described in more detail later on, but their functions can be summarized in a following way. The first part is responsible for simulation of the drift and expansion of the electron cloud inside of the silicon wafer based on the information from GEANT. It also simulates response of the readout electronics for the incoming signal. The second part generates background under the simulated hits. By background we mean that it either generates random noise with realistic amplitudes or, if the simulator is run inside of embedding, it mixes the simulated data with real data at the level of detector signal. Since, before the data are saved, the SVT detector uses online data selection and noise reduction, the third part simulates the appropriate behavior of the online Data Acquisition System (DAQ).

Hence initially the system obtains information from GEANT about position of the hits and energy deposited by the particle and the final results of the simulation are data similar in

the format to a raw data that are saved during data-taking. On these data from simulation can then be run standard STAR reconstruction system as it is done with real data.

5.4.1 Electron cloud simulation

A charged particle passing through silicon creates cloud of excited electrons which expands as it drift toward the readout anodes. The expansion is caused by a Coulomb repulsion and diffusion of the electrons [185]. A detailed simulation of such processes for each hit in the SVT would take an extremely long time. Instead in this work we use an approximation of the cloud by two dimensional Gaussian proposed by V.Rykov [186].

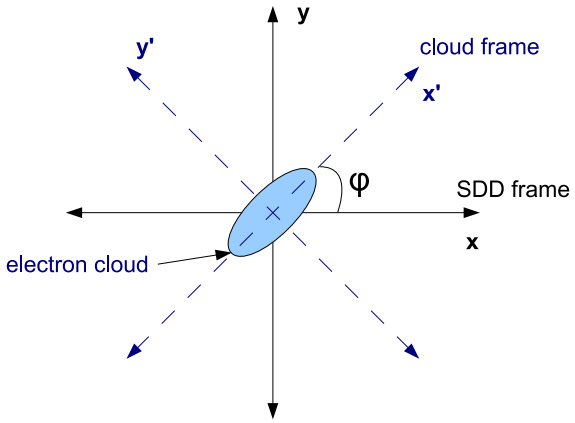

Figure 5.7: Schematic drawing of the 2D Gaussian parametrization of the electron cloud created by the ionizing particle crossing the silicon wafer under angle φ - angle between direction of the drift and projection of the particles velocity on to the wafer. Figure adapted from [187].

In this approximation the expansion of the cloud is then calculated as the change of the two main axes of the Gaussian distribution(Figure 5.7).

$$f(x', y') = \frac{1}{2\pi\sigma_{x'}\sigma_{y'}} \exp\left(-\frac{(x')^2}{2\sigma_{x'}^2} - \frac{(y')^2}{2\sigma_{y'}^2}\right), \tag{5.2}$$

where $\sigma_{x'}(t)$, and $\sigma_{y'}(t)$ are the major and minor axis that change with the time as:

$$\frac{d\sigma_{x'}^2}{dt} = 2D_{x'} + f_{x'}(\sigma_{x'}^2, \sigma_{y'}^2), \quad \frac{d\sigma_{y'}^2}{dt} = 2D_{y'} + f_{y'}(\sigma_{x'}^2, \sigma_{y'}^2). \tag{5.3}$$

The $D_{x'}$, and $D_{y'}$ are diffusion constants in the frame of the electron cloud. The functions

$f_{x',y'}(\sigma^2_{x'},\sigma^2_{y'})$ describe expansion of the electron cloud via Coulomb repulsion [186]:

$$f_{x'}(\sigma^2_{x'},\sigma^2_{y'}) = \left(\frac{\mu Q}{4\pi\epsilon_0\epsilon}\right)\frac{K_1(\frac{\sigma_{y'}}{\sigma_{x'}})^\alpha - \frac{K_3}{\beta}\ln\left\{(\frac{\sigma_{y'}}{\sigma_{x'}})^\beta + [1+(\frac{d}{\sigma_{y'}})^2]^{-2}\right\}}{\sigma_{x'}\left[1+\left(\frac{K_1\sigma_{y'}}{K_2 d}\right)^\gamma\right]^{1/\gamma}},$$

$$f_{y'}(\sigma^2_{x'},\sigma^2_{y'}) = \left(\frac{\mu Q}{4\pi\epsilon_0\epsilon}\right)\frac{K_3-(K_3-K_1)(\frac{\sigma_{x'}}{\sigma_{y'}})^\delta}{\sigma_{x'}\left[1+\left(\frac{K_1\sigma_{y'}}{K_2 d}\right)^\gamma\right]^{1/\gamma}}, \tag{5.4}$$

$$\sigma_{x'} \geq \sigma_{y'},$$

where μ is the electron cloud mobility; ϵ is the dielectric constant of the silicon; d is the thickness of the SDD wafer and Q is the total charge of the electron cloud. The constant $K_{1,2,3}$ are defined from asymptotic behavior of the Coulomb repulsion term[186]: $K_1 = 0.43$, $K_2 = 0.25$, $K_3 = 0.58$. The values of the phenomenological constant $\alpha = 2/3$, $\beta = 4$, $\gamma = 3/2$ and $\delta = 1/2$ were chosen [186] to provide agreement with corresponding numerical solution of full continuity equation. More details on regarding the theoretical equations can be found in [187].

One can notice that appearance of the $\sigma_{x'}$ in the denominator of 5.4 can cause a difficulty when numerically computing 5.3 for small (initial) values of $\sigma_{x'}$. For this reason it is better to use the 5.3 in terms of

$$\frac{d\sigma^3_{x',y'}}{dt} = \frac{3}{2}\sigma_{x',y'}\frac{d\sigma^2_{x',y'}}{dt}. \tag{5.5}$$

An additional effect that has influence on the electron cloud expansion is the so called *trapping/detrapping* effect. It is caused by impurities in the silicon which can capture the excited electrons for a short time and hence slowing them down during the drift. In our calculation this effect is accounted for by having different effective diffusion constants in the drift and anode direction:

$$\begin{aligned} D_x &= D + \tau_{trap} * v^2_{drift} \\ D_y &= D, \end{aligned} \tag{5.6}$$

where the $D = 0.0035\ mm^2/\mu s$ is electron diffusion constant in silicon, the v_{drift} is electron drift velocity, and $\tau_{trap} \sim 5\cdot 10^{-5}\mu s$ is the electron trapping constant. The inclusion of the trapping/detrapping into diffusion constant causes effectively the electron cloud to rotate the major axis towards the drift direction as the cloud expands over the time. Results of calculations with different initial angle φ can be found in [187].

After the electron cloud reaches the readout anodes the signal is amplified and shaped in

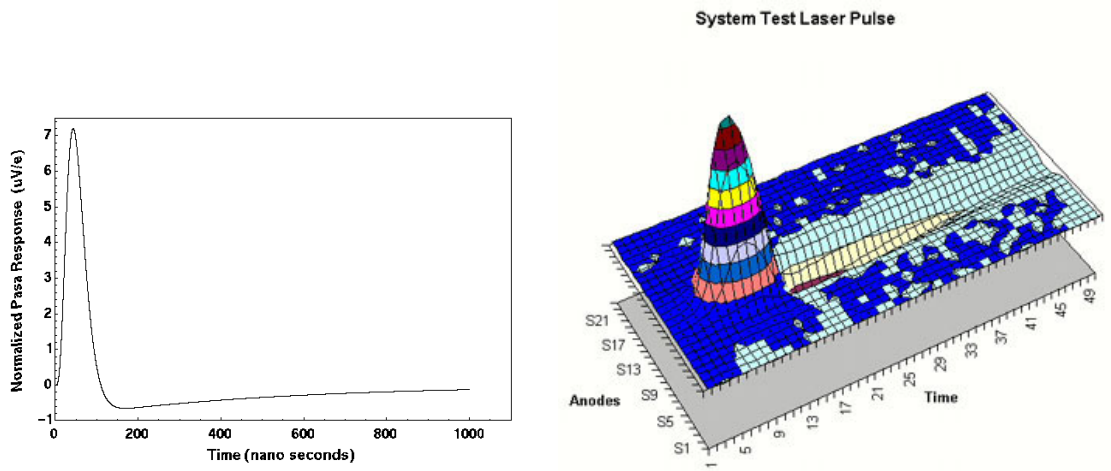

(a) (b)

Figure 5.8: (a) Shape of the Preamplifier and Shaper(PASA) response. (b) Measured response to laser hit in SDD.Figure from [181].

the Front-End Electronics(FEE). First the incoming signal is shaped by the the PreAmplifier ShAper (PASA). Signal from a simulation of the PASA response is shown in Figure 5.8. Extended discussion about PASA simulation is in [187]. Following the amplification the signal is stored in a Switch Capacitor Array (SCA) which samples the signal with frequency of $\sim$ 25 MHz giving 128 bins in the drift direction.

After simulation of the hits it is necessary to include realistic simulation of the background. Proper simulation of the noise is necessary as it can significantly alter properties of the reconstructed hits. High noise can not only create fake hist, but it can also smear signal of real hits an they may not get reconstructed properly. The noise of the detector can vary in time and also wafer by wafer. For this reason the simulator allows to retrieve information about noise levels for individual wafers for the given date that the simulation is run for. If the simulator is only run in simple simulation without embedding the whole wafer is covered by the generated signal. However if the simulator is run for the purpose of embedding the simulation into real data their generated noise is superimposed only on the simulated hits as the real data already include its own noise. The simulated data are then mixed with the real data and passed further to the simulation of DAQ.

Before saving to the storage the volume of the data has to be significantly reduced. The Data Acquisition System (DAQ) contains algorithm for online selection of hits as well as for noise reduction. In the DAQ only hits with succession of pixels that pass selection criteria are kept. These criteria are chosen so that a random noise and occasional signal spikes do not pass. These criteria vary between individual runs and are hence loaded from database for every simulation. An example of the simulated signal from the SVT detector after the

three stage is shown in Figure 5.9.

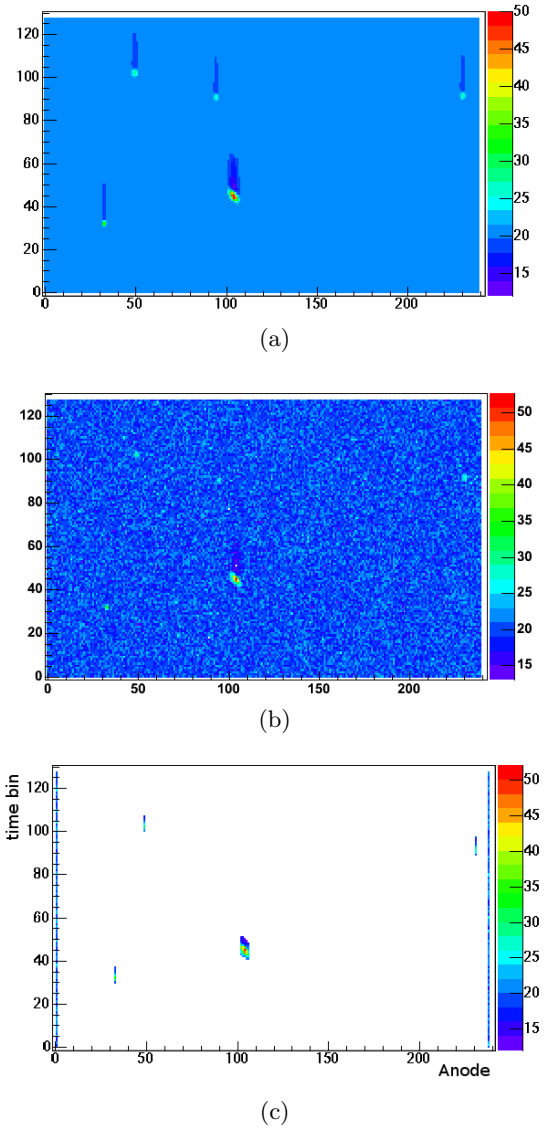

(a)

(b)

(c)

Figure 5.9: Output of the SVT slow Simulator at different stages of the simulation from top to bottom: (a) simulated hits and PASA response (b) addition of the simulated background (c) final simulated event after passing DAQ simulation.

5.4.2 Simulation to real data comparison

The expansion of the electron cloud causes the properties of hits to change with the time and hence with the drift distance. To test the functionality of the simulator we compare basic properties of the reconstructed hits from simulator to those from real data.

By the simple nature of the cloud expansion we should expect to to see that as we go

from short to long drift times the hits should be larger and their height (peak ADC) should decrease. During initial tests of the SVT detector the expansion of the electron cloud in anode direction was measured using laser induced ionization [188]. The results of the measurements are compared in Figure 5.10 with the theoretical predictions for the cloud expansion. One can observe that in the initial stages of the expansion when the electron cloud is dense the Coulomb repulsion plays dominant role while later the the expansion is driven mainly by the diffusion.

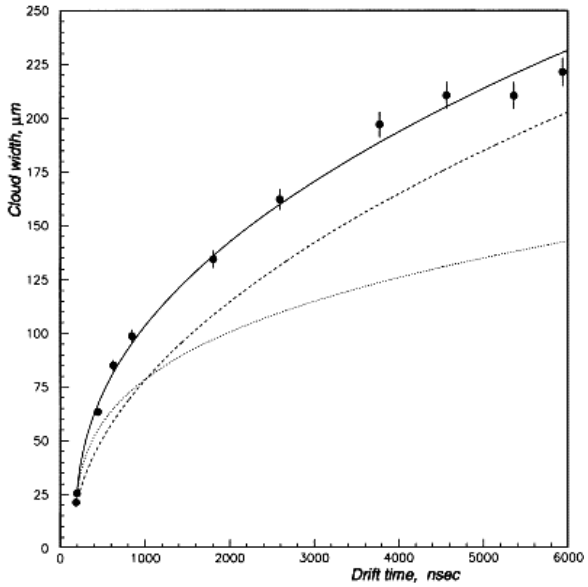

Figure 5.10: Dependence of the cloud size in anode direction on drift time. Points are data, solid line shows theoretical calculations with diffusion and Coulomb repulsion. Dashed line shows the diffusion only. Dotted line shows Coulomb repulsion only. Figure from [188].

A similar comparison has to be done between the simulator and the real data. A comparison of four basics properties of the reconstructed hits is shown in Figure 5.11. In Figure 5.11(a) is spectrum of heights of hits, shown as maximum of Analog-To-Digital converted signal (ADC) of the hit. In Figure 5.11(b) is dependence of the average height of hits as a function of the drift time. In Figure 5.11(c) is shown dependence of an average width of hits in the time direction also as function of time. By the width of the hit is meant the ADC weighted RMS of reconstructed hit. One can clearly observe significant change in the height and size of the hits as function of the time it takes the electron cloud to reach the readout anodes. With the time the cloud gets significantly more spread out and the density of the electrons decreases. One can expect that as the signal gets weaker some parts of the hits will "sink" into the background and will not get reconstructed as part of the hit. This is indeed observed in the Figure 5.11(d) where the average total reconstructed charge of the hits is

shown as a function of the drift time.

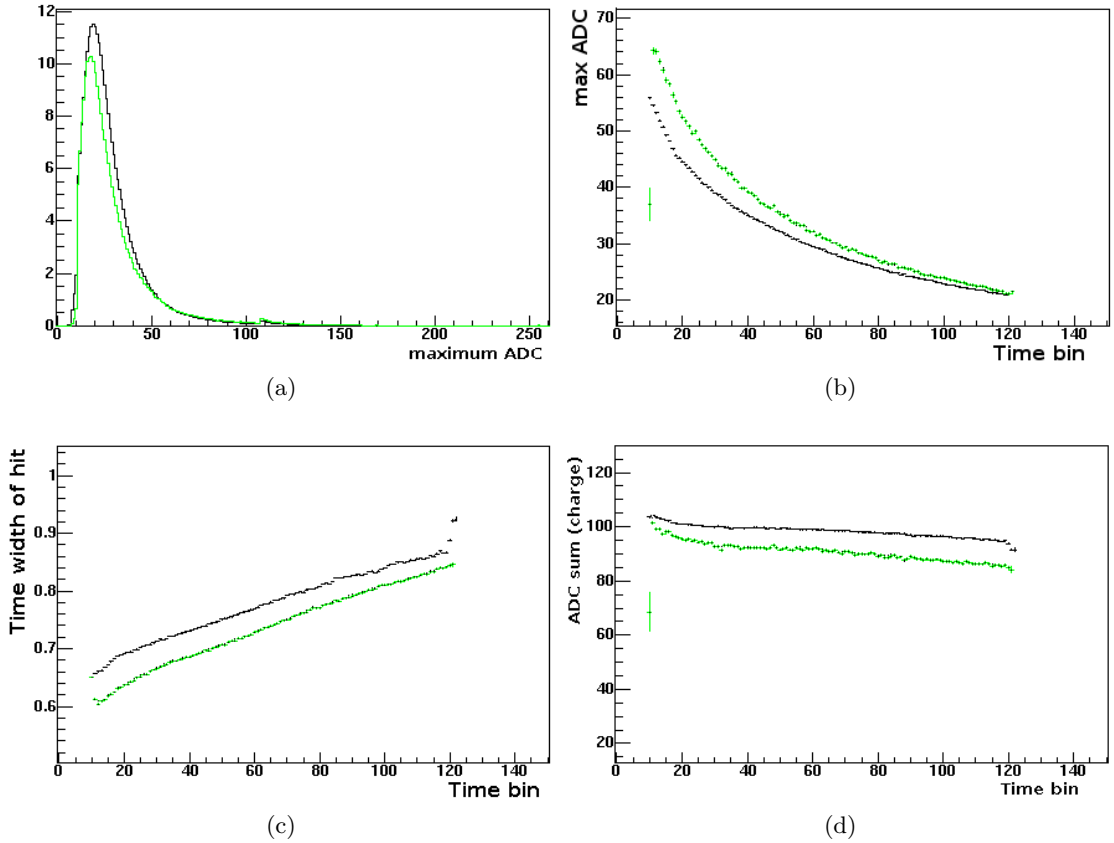

(a) (b)

(c) (d)

Figure 5.11: Comparison of properties of reconstructed hits in the SVT between real data in Black and simulation in green. (a) Spectrum of maximal ADC values in the hits. (b) dependence of the average maximum ADC value in the hits as function of the drift time. (c) dependence of the average RMS(width) in time direction of the hit as function of the drift time. (d) time dependence of the average reconstructed charge of the hit.

We observe that while general shape of presented hit distributions is in good agreement with the data there is a discrepancy in the absolute scales. This can be attributed to different initial conditions of the simulation, such as the initial sizes of the hits. The initial conditions can be fine-tuned by comparison of the simulation and real data at short drift times. This indeed was performed in [182] and together with refining of the gain of the electronics brought excellent agreement between the simulation and the data, as shown in Figure 5.12. Complete detail on the fine-tuning procedure can be found in [182].

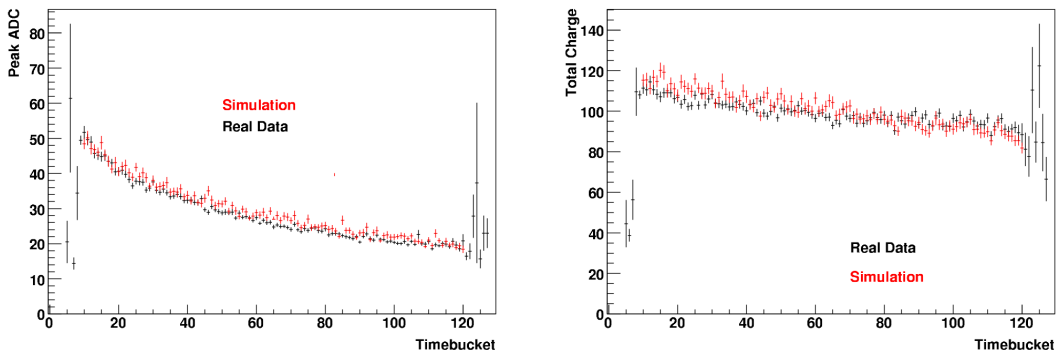

(a) (b)

Figure 5.12: Comparison between SVT simulation and real data after fine-tuning of initial sizes of the electron cloud. Left: peak ADC versus time. Right:total charge versus time. Figure from [182].

Chapter 6

Femtoscopy of $\pi - \Xi$ system

6.1 Physics motivation

From measurements presented in Section 2 some general conclusions can be drawn which frame and motivate the main theme of this thesis, the $\pi - \Xi$ correlations, in the context of ultra-relativistic heavy ion physics.

The matter created in collisions of heavy ions exhibits properties suggesting that a state of deconfined partonic degrees of freedom was reached [63]. Current data on spectra and elliptic flow from Au+Au collisions at RHIC energies demonstrate that hot and dense system created in the collision builds up substantial collectivity leading to rapid transverse expansion. Moreover, properties of the induced flow strongly depend on whether the collectivity is achieved at partonic or hadronic level. It's clear that multi-strange baryons, including Ξ, obtain throughout the evolution of the system substantial elliptic flow [92] comparable in magnitude to other particle species. Because of their presumably small hadronic cross-section multi-strange baryons are expected to undergo few interactions in the hadronic phase [84], and hence provide more direct probe into the early partonic stage. The study of multi-strange baryon flow is the of high importance since the collective behavior of these particles, suggested by large values of observed elliptic flow together with its observed constituent quark scaling, suggests that collective motion was already achieved prior to hadronization - already at the partonic level.

As discussed in the Section 3.4 the space-time structure of the particle emitting source is strongly affected by a collective expansion. It exhibits as an effective decrease of measured HBT radii and a difference between average emission points for particle species with non-equal masses. The non-identical particle correlations can be used as an independent cross-check of flow measurements in heavy-ion collisions by measuring this flow-induced emission asymmetry.

It was already shown that in heavy-ion collisions average emission points of pions, kaons,

and protons are not the same [150] (Figure 3.10). Hydrodynamically inspired models [74] predict a mass-ordering of average space-time emission points with the effect increasing with a mass difference of the measured particle pair. Since this effect is predicted to increase with a mass difference between the particles, studying correlations in system, such as $\pi-\Xi$, where the mass difference is large, should provide important test of transverse expansion of the matter and flow of multi-strange baryons.

6.2 Data selection

In this femtoscopic analyses we aim to extract rather subtle correlation signal out of, in total, four tracks left by $\pi-\Xi$ pair in the STAR detector. Proper selection of data, on the level of event, track, and pair cuts is crucial for removing any unwanted detector effects yet not to hinder available statistics. The data selection and cuts are described in the text in the order similar to the flow of data during the actual analysis itself - starting with selection of dataset and following with event level cuts, track cuts, Ξ reconstruction, and pair cuts.

6.2.1 Event selection

Two data sets of Au-Au collisions at energies $\sqrt{s_{NN}}$=200 GeV and $\sqrt{s_{NN}}$=62 GeV recorded by the STAR experiment during a Run IV has been used in the following analysis. The dataset at $\sqrt{s_{NN}}$=200 GeV consists of two parts: a minimum bias sample covering 80% of the most central to peripheral events ($16 \cdot 10^6$ events). In addition a sample of central events ($10 \cdot 10^6$ events) at $\sqrt{s_{NN}}$=200 GeV was taken to enhance the statistics of the data in 10% most central collisions. In the case of $\sqrt{s_{NN}}$=62 GeV collisions a minimum bias dataset consisting of events with centrality between 0%-80% most central collisions has been used. All the data were taken with a maximum magnetic field of 0.5 Tesla generated by the main STAR magnet.

In all the datasets the main cuts applied at the level of the whole events are cuts on the main vertex position and centrality of the event. Only events with reconstructed collision vertex positioned within ±25cm from center of the main TPC were selected in order to ensure the same acceptance across the pseudorapidity region $|\eta| \lesssim 1$ used for the π and Ξ. The STAR experiment employs centrality selection based on uncorrected charged multiplicity in the mid-rapidity region $|\eta| < 0.5$ as described in [66]. The available statistics of data samples (minimum bias plus the central-triggered data) together with Ξ reconstruction efficiency, which will be described later, dictates the use of only three centrality bins corresponding to a fraction of total hadronic cross section of 0-10%, 10-40%, and 40-80% from central to peripheral collisions. The remaining 80-100% most peripheral bin cannot be used because of trigger bias at low multiplicities. .

6.2.2 Particle selection

This analyses was performed using information obtained from tracks left by charged particles in the main TPC. The available particle statistics and their distribution in momentum and rapidity is hence driven by acceptance, and resolution of the TPC combined with detection and reconstruction efficiency. Since only charged particles leave and ionization track in the TPC gas the analysis can be done only for pairs with both π and Ξ charged, as the $\pi^{\pm}$ and the decay products of $\Xi^{\pm}$ leave an ionization signal in the TPC.

Primary pion selection

As first particle in the studied pair are selected primary pions. We use tracks which, with pion mass assumption, fall in rapidity window $|y| < 0.8$. To ensure a good quality of the used tracks we require that the track has a minimum number of 15 hits in the TPC. For the track to be considered as a primary we require that it points toward the reconstructed primary vertex of the collision. This requirement is defined by a cut on DCA (Distance of Closest Approach of the extrapolated track to the primary vertex) to be less then 3 cm.

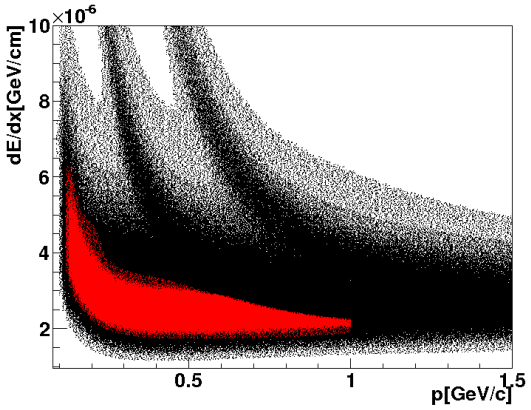

Figure 6.1: Pions selected according to their energy loss dE/dx in the TPC.

To identify the track as originating from pion we use the information about energy loss dE/dx in the TPC gas, as discussed in Section 4.2.1. For the track to be selected for this analysis as a pion its measured dE/dx must be within 2σ (standard deviations) from the value predicted by 4.1 for a pion of a given momentum. The widths of the dE/dx bands around the mean of 4.1 are momentum and multiplicity dependent property of TPC and are deduced from experimental data. As shown in the Figure 4.6 the dE/dx band of pions crosses at low p_T with signal coming from electrons and at $p_T \gtrsim 1GeV$ becomes indistinguishable from kaons sand protons. In order to remove significant contamination from protons and kaons we also require that the dE/dx signal lies at least 2σ away from the dE/dx band of kaons and protons. This , as shown in the Figure 6.1, together with p_T-

acceptance of TPC limits reachable pion p_T range to be effectively $0.08 < p_T < 0.6$ GeV/c event though and additional cut on $p < 1$ GeV/c is introduced. In the low p_T region remains the contamination from electrons. Because of the huge mass difference between the pions and electrons the misidentified tracks from electrons will not influence the final correlation function. The electron contamination will only show up in the increase of the λ parameter.

Ξ reconstruction and selection

The multi-strange baryons Ξ are often called the "cascades" because of their characteristic main decay channel. Multi-strange baryons were for the first time observed in experiments in which cosmic rays or beams of accelerated particles interacted in bubble chambers. In experiments, such as the one in which Barnes discovered Ω^- baryon [189], typical pattern of tracks from charged particles from subsequent decays is seen. Because of its lifetime the Ξ cannot be detected directly as it decays close to the collision region outside of the active volume of the detector. However this decay length is sufficient for topological reconstruction which means that we are able to distinguish between the main collision vertex and secondary decay vertexes of Ξ. The geometry of the main decay channel, as shown in Figure 6.2, is used to reconstruct individual particles undergoing the decay via $\Xi \to \Lambda + \pi$, and subsequently $\Lambda \to \pi + p$. In Table 6.1 are shown properties of the concerned particles.

particle	quark content	mass[MeV]	$c\tau$[cm]	decay mode	$\simeq$B.R.
Ξ^-	dss	1321.31 ± 0.13	4.91	$\Lambda\pi^-$	99.9
Ξ^0	uss	1314.83 ± 0.20	8.71	$\Lambda\pi^0$	99.5
Λ	uds	1115.683 ± 0.006	7.89	$p\pi^-$	63.9

Table 6.1: Particle properties according to the Particle Data Group [13].

We are not able to topologically reconstruct the neutral Ξ^0 since it decays into a Λ and neutral pion which does not leave ionization information in the TPC. For this reason only the charged Ξ^- and Ξ^+ are used in this analysis.

In the topological reconstruction of Ξ we are looking for a particular configuration of three tracks in an environment of high track multiplicity. The combinatorial background, ie. the number of rejected candidates, is huge and performing such a selection for every analysis pass on the data would take an unreasonably long time. In order to significantly speed up the analysis the data selection was done in two passes. In the first "prefilter" pass most of the Ξ candidates were rejected using looser cuts which removed most of the combinatorial background and only events with suitable candidates were saved. Final cuts are used then used later during physics analysis.

The, so called *bachelor pion* pion from Ξ decay, proton and pion from Λ decay are selected according to their specific ionization dE/dx in the TPC on the level of 3σ around the mean

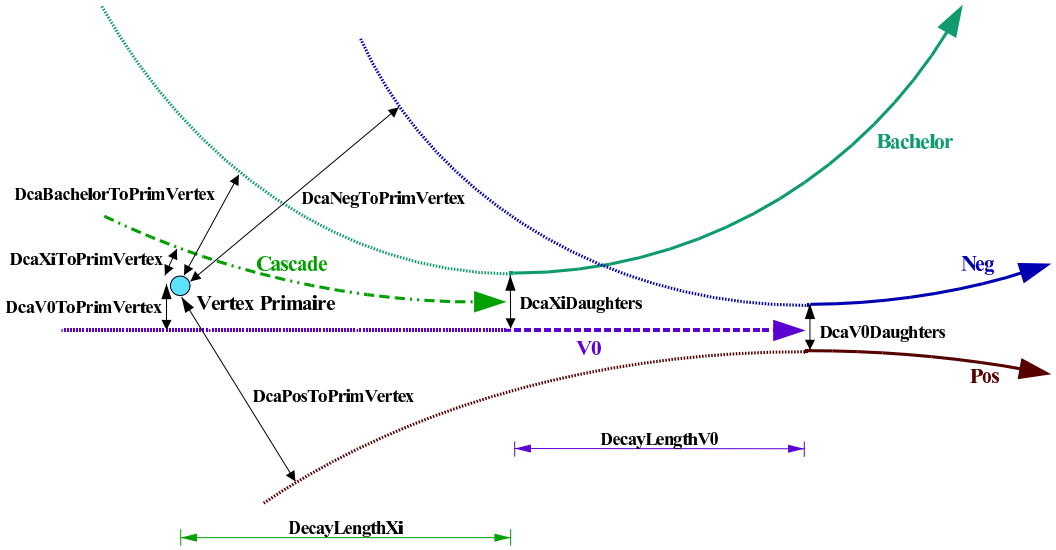

Figure 6.2: Schematic drawing of the cuts used in the topological reconstruction of Ξ. Figure from [190].

value predicted by 4.1. After that the topological cuts depicted in Figure 6.2 are employed to select Ξ candidates, according to values in Table 6.2 and 6.3, The procedure of reconstruction of multi-strange baryons and cut optimization has been extensively studied within the STAR collaboration. Complete study of Ξ reconstruction can be found in [191, 190, 192]. The last two rows in the Tables 6.2 and 6.3 define cut based on the relation between DCA of Ξ and DCA of the subsequent Λ to the primary vertex. Two types of the functional - p_T dependent relations are used (denoted as **DcaV0ToPrimVtxCorrType**).
For **DcaV0ToPrimVtxCorrType**=1:

$$\begin{aligned}\text{DcaV0ToPrimVertex} > &\sqrt{\text{DcaXiToPrimVertex}} + \text{DcaV0ToPrimVtxCorrOffset} \\ &+ 0.4 \left[1. - \left(1 + e^{(-4.p_T + 6.)}\right)^{-1}\right],\end{aligned} \tag{6.1}$$

and for **DcaV0ToPrimVtxCorrType**=2:

$$\begin{aligned}\text{DcaV0ToPrimVertex} > &\sqrt{\text{DcaXiToPrimVertex}} + \text{DcaV0ToPrimVtxCorrOffset} \\ &+ 0.05 \left[1. - \left(1 + e^{(-4.p_T + 3.)}\right)^{-1}\right].\end{aligned}$$

6.2.3 Background construction - event mixing

In the process of obtaining the experimental correlation function according to 3.39 the two-particle distribution for the denominator must be created. The goal is to obtain a distribution

	$0-10\%$ prefilter	$0-10\%$ final	$10-40\%$ prefilter	$10-40\%$ final	$40-80\%$ prefilter	$40-80\%$ final
track $\sigma_{dE/dx}$	3	3	3	3	3	3
m_Ξ range[GeV/c^2]	0.025	0.007	0.025	0.007	0.025	0.007
m_λ range[GeV/c^2]	0.030	0.007	0.030	0.007	0.030	0.007
min p_T [GeV/c]	>0.5	0.6	0.5	0.6	0.5	0.6
Rapidity range	<1.5	0.8	1.5	0.8	1.5	0.8
TpcHitsBac	>8	15	7	10	7	10
TpcHitsV0Baryon	>10	20	10	15	10	10
TpcHitsV0Meson	>10	10	10	10	10	10
DecayLengthXi	>3	5	2	3	1.3	2
DecayLengthV0	>0	0	0	0	0	0
DcaXiToPrimVtx	<0.70	0.55	0.70	0.55	0.70	0.55
DcaV0ToPrimVtx	>0.09	0.10	0.09	0.10	0.09	0.10
DcaBacToPrimVtx	>1.20	1.50	0.80	1.00	0.60	0.90
DcaXiDaughters	<0.80	0.70	0.80	0.70	0.80	0.70
DcaV0Daughters	<0.80	0.70	0.80	0.70	0.80	0.70
DcaV0ToPrimVtx CorrType	1	1	1	1	2	2
DcaV0ToPrimVtx CorrOffset	-0.08	0.00	-0.15	-0.10	-0.35	-0.20

Table 6.2: Values of the cuts used for topological reconstruction of the Ξ in the Au+Au collisions at $\sqrt{s_{NN}}$=200 GeV. All distance values are in centimeters.

of pairs similar to the distribution of real pairs, but without any femtoscopic correlations. In this analyses we use an "on-the-fly" mixing of events. As the individual events pass through the analyses they are divided into "similarity classes" according to a chosen set of physics and detector characteristics. Then spectrum of pairs is created by taking a first particle(pion) from one event and pairing it with a second particle(Ξ) from a different event. Only events withing the same class are mixed in order not to introduce artificial correlations into the created two-particle spectra by mixing up two "too" different single-particle spectra.

In this analyses three parameters according to which we divide the events into the different classes (bins) are used. Two of them are physics observables: event multiplicity and orientation of the event plane. The binning in the event plane orientation helps to remove correlations at large values of k^* which come mainly from elliptic flow. This helps to flatten the normalization region of correlation function where no two-particle effects should be present. Proper normalization is crucial for fitting the experimental correlation function with theoretical predictions. The effect of the binning in the event plane orientation is shown in Figure 6.16. The third binning parameter is detector-related and it is the position of the collision vertex along the beam direction. This is used to eliminate effects of changing acceptance as a function of position of the vertex. In addition one more parameter is used for

	$0-10\%$ prefilter	$0-10\%$ final	$10-40\%$ prefilter	$10-40\%$ final	$40-80\%$ prefilter	$40-80\%$ final
track $\sigma_{dE/dx}$	3	3	3	3	3	3
m_{Ξ} range[GeV/c^2]	0.020	0.007	0.020	0.007	0.020	0.007
m_{λ} range[GeV/c^2]	0.010	0.007	0.010	0.007	0.010	0.007
min p_T[GeV/c]	>0.5	0.6	0.5	0.6	0.5	0.6
Rapidity range	<1.5	0.8	1.5	0.8	1.5	0.8
TpcHitsBaclo	>15	15	10	10	10	10
TpcHitsV0Baryonlo	>20	20	15	15	10	10
TpcHitsV0Mesonlo	>10	10	10	10	10	10
decayLengthXi	>3	5	1.5	3	1.3	1.5
decayLengthV0	>0	0	0	0	0	0
DcaXiToPrimVtx	<0.60	0.55	0.60	0.55	0.60	0.55
DcaV0ToPrimVtx	>0.10	0.10	0.10	0.10	0.10	0.10
DcaBacToPrimVtx	>1.30	1.50	0.90	1.00	0.80	0.90
DcaXiDaughters	<0.70	0.70	0.70	0.70	0.70	0.70
DcaV0Daughters	<0.70	0.70	0.70	0.70	0.70	0.70
DcaV0ToPrimVtx CorrType	1	1	1	1	1	1
DcaV0ToPrimVtx CorrOffset	-0.10	0.00	-0.15	-0.10	-0.20	-0.20

Table 6.3: Values of the cuts used for topological reconstruction of the Ξ in the Au+Au collisions at $\sqrt{s_{NN}}$=62 GeV. All distance values are in centimeters.

binning implicitly which is the time at which the events were recorder. This is important and should not be overlooked as the acceptance of detector may significantly change over the whole period of data taking. This condition is satisfied automatically as the data coming to the analysis from prefilter are automatically stored in files according to a day at which they were taken. For this analysis we use binning of 5 bins in multiplicity, 5 in event plane angle and 10 cm wide bins in vertex position.

One has to be careful when combining the data from different mixing bins. Simple summing of the pair spectra for numerators $A_i(\vec{q})$ and denominators $B_i(\vec{q})$ of 3.39

$$C(\vec{q}) = N\frac{\sum\limits_i A_i(\vec{q})}{\sum\limits_i B_i(\vec{q})}, \tag{6.2}$$

where i =(multiplicity,event plane, vertex position) runs over all event-class bins, may lead to an introduction of fake correlations effects. In each mixing bin the real correlation function should be the same:

$$C_i(\vec{q}) = N_i\frac{A_i(\vec{q})}{B_i(\vec{q})} = C(\vec{q}), \tag{6.3}$$

but the two-particle spectra and normalization constant will differ from bin to bin: $A_i(\vec{q}) \neq A_j(\vec{q})$, $B_i(\vec{q}) \neq B_j(\vec{q})$, $N_i \neq N_j$. Altering 6.2 to include 6.3

$$C(\vec{q}) = N\frac{\sum_i B_i(\vec{q})\frac{A_i(\vec{q})}{B_i(\vec{q})}}{\sum_i B_i(\vec{q})} = N\frac{\sum_i B_i(\vec{q})\frac{C(\vec{q})}{N_i}}{\sum_i B_i(\vec{q})} = NC(\vec{q})\frac{\sum_i \frac{B_i(\vec{q})}{N_i}}{\sum_i B_i(\vec{q})} \tag{6.4}$$

we see that to have the right-hand side equal $C(\vec{q})$ only up to a normalization constant the last sum must not depend on $\vec{q}$. This can be done only if $B_i(\vec{q}) = B_j(\vec{q})$, which is not - that's why we do the mixing, or if the two-particle distributions are added with the same weight $N_i = N_j$. For this reason in our analyses we first rescale the denominators of each bin to $B'_i(\vec{q}) = B_i(\vec{q})/N_i$ before summing over all bins to get the final correlation function.

6.2.4 Pair cuts

Even with a proper mixing the real two-particle distribution contains detector related non-femtoscopic correlations at low $\vec{k}^*$ which are not present in the mixed background. These effects arise as consequence of imperfect track reconstruction. During the reconstruction process the signal from a single particle may be accidentally reconstructed as two separate tracks with very close momenta. This "track splitting" then shows up as an increase in the measured correlation function. An opposite effect of "track merging" when two close tracks from two different particles are accidentally reconstructed as only one final particle may occur as well. This in turn leads to a decrease of the correlation. To remove these effect cuts on the level of pairs must be applied to both real and mixed pairs.

Track splitting

The cut that removes the splitting is the same as the one employed in [111] and is discussed in detail in [193]. It is based on a comparison of locations of the actual hits in TPC belonging to the two tracks and assigning a value of "splitting level"(SL) to the pair of tracks according to a formula:

$$SL = \frac{\sum_i S_i}{Nhits_1 + Nhits_2}, \tag{6.5}$$

where i is the pad-row number of the TPC, and $Nhits_1$ and $Nhits_2$ are the total number of hits associated for each track and S_i takes value depending on existence or non-existence of

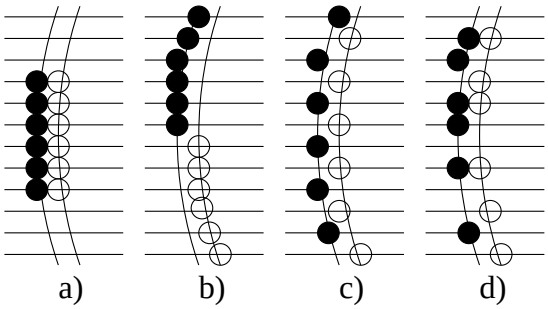

Figure 6.3: Schematic description of the anti-splitting cut. Different scenarios of hit distribution in the TPC for possibly split tracks. Closed circles are hits assigned to one track, open circles are assigned to the other. a) SL = -0.5 (clearly two tracks) b) SL = 1 (possible split track) c) SL = 1 (possible split track) d) SL = 0.08 (likely two tracks). Figure from [111].

hits at a given pad-row:

$$S_i = \begin{cases} +1 & \text{one track leaves a hit on pad-row} \\ -1 & \text{both tracks leave a hit on pad-row} \\ 0 & \text{neither track leaves a hit on pad-row.} \end{cases} \tag{6.6}$$

The SL ranges from -0.5 for certainly distinct tracks to 1.0 for track with high likely-hood of splitting. The principle of this anti-splitting cut is depicted in Figure 6.3. For our analyses we require $-0.5 \leq SL \leq 0.8$ for all pairs of used tracks of the same electric charge.

In addition a strong effect of track splitting has been observed between tracks of primary pion and the bachelor pion from Ξ decay. As can be seen in Figure 6.4 the phase space corresponding to the small difference between momenta of bachelor and primary pions, where the splitting occurs, corresponds to a rather insignificant part of the k^*-space of the $\pi - \Xi$ pairs and can be safely removed by a cutting on difference of momenta $|\vec{p}_{primary} - \vec{p}_{bachelor}| > 0.065\text{GeV}/c$. This is different from anti-splitting procedures used in $\pi-\pi$ HBT where performing cuts on phase-space would lead to a significant loss of statistics.

Track merging

The procedure of removing effects of track merging is again similar as in the case of $\pi-\pi$ analyses [111, 193]. Hits from two tracks are considered merged when the probability of separating them is less than 99% according to the two-track resolution of the TPC. We use requirement of all pairs to have a fraction of merged hits smaller than 10%.

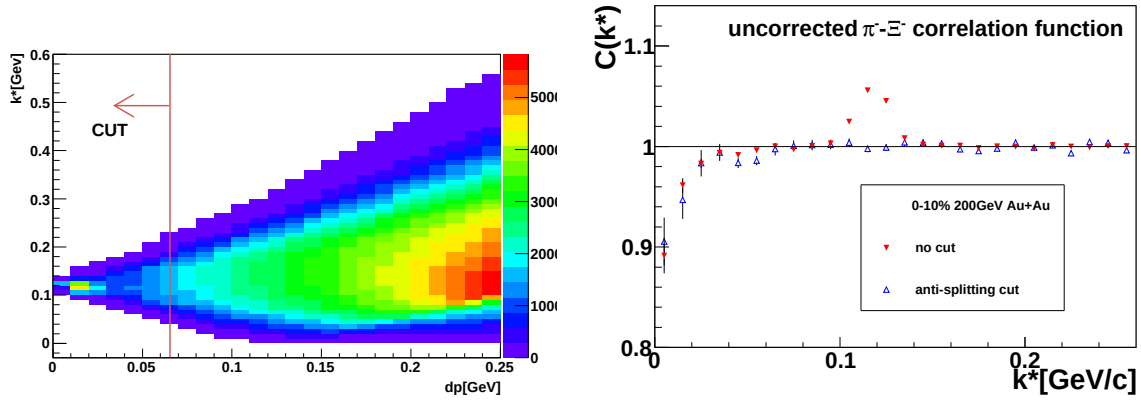

(a) (b)

Figure 6.4: Effects of the track splitting between bachelor and primary pion in the like-sign correlation function. Left: numerator of the correlation function as a function of k^* of the pair and difference of momenta of primary and bachelor pion $dp = |\vec{p}_{primary} - \vec{p}_{bachelor}|$. Right: Comparison of the uncorrected correlation function with and without the applied cut on $dp > 0.065$ GeV/c.

6.3 Purity corrections

As described in Section 3.2.1 the admixture of pairs containing misidentified or non-primary (coming from long-lived decays) particles is a cause a significant decrease as well as deformation of the measured correlation function when compared to a "real" correlation function which would be measured by an ideal experiment in accordance with theoretical formula 3.16 and 3.32. Compared to the Section 3.2.1, where a simple constant λ was introduced as a correction into the measured correlation function, in the case of $\pi-\Xi$ analyses more sophisticated approach has to be used as the amount of non-purities can vary as a function of $\vec{k}^*$.

In this analysis the corrected (real) correlation function $C(\vec{k}^*)_{real}$ is obtained from the experimentally measured $C(\vec{k}^*)_{exp}$ as

$$C(\vec{k}^*)_{real} = \Big[C(\vec{k}^*)_{exp} - 1\Big] * P(\vec{k}^*) + 1, \tag{6.7}$$

where $P(\vec{k}^*)$ is the purity of the pair, the ratio of correlated to all pairs, as a 3-dimensional function of $\vec{k}^* = (k^*, cos\theta, \varphi)$. The purity of the $\pi-\Xi$ pair is calculated as a product of purities of individual particles samples: $P_{\pi\Xi} = P_\pi \cdot P_\Xi$.

pion purity

There are two main sources for impurities of pions. First, with a certain probability, other particles then pions can be wrongly identified as pions according to their dE/dx energy loss. In this analysis this is mainly the case of electrons due to the crossing of electron and pion dE/dx band at low p_T. The additional decrease of purity of pion sample is due to real pions coming from weak decays and decays of long-lived resonances which decay far out of the collision region so that their decay products are not correlated via FSI with the rest of the system.

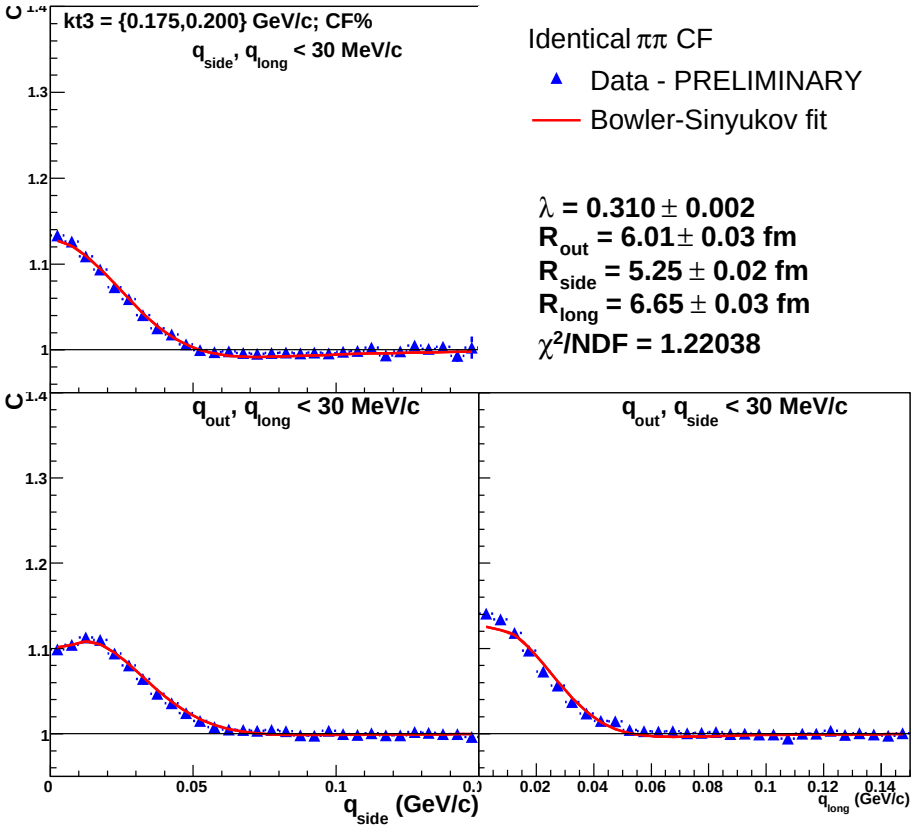

Figure 6.5: Example of a measured identical $\pi-\pi$ correlation function in the 10% most central Au+Au collisions at $\sqrt{s_{NN}}$=200 GeV, combining signal from $\pi^+-\pi^+$ and $\pi^--\pi^-$. The shown results are for pairs with 175MeV/c < k_T < 200MeV/c. The correlation functions are plotted in the *out, side, long* projections with unprojected direction integrated over $q_{out}, q_{side}, q_{long}$ < 30MeV/c.

As discussed in the Section 3.2.1 the inclusion of uncorrelated particles in the femtoscopic measurements with identical particle will result in a decrease of the strength of the correlation and increase of the extracted λ parameter. We use this factor for our analyses and take $\sqrt{\lambda}$ from $\pi-\pi$ HBT as a measure of purity of primary pions. It was discussed [194, 110], that

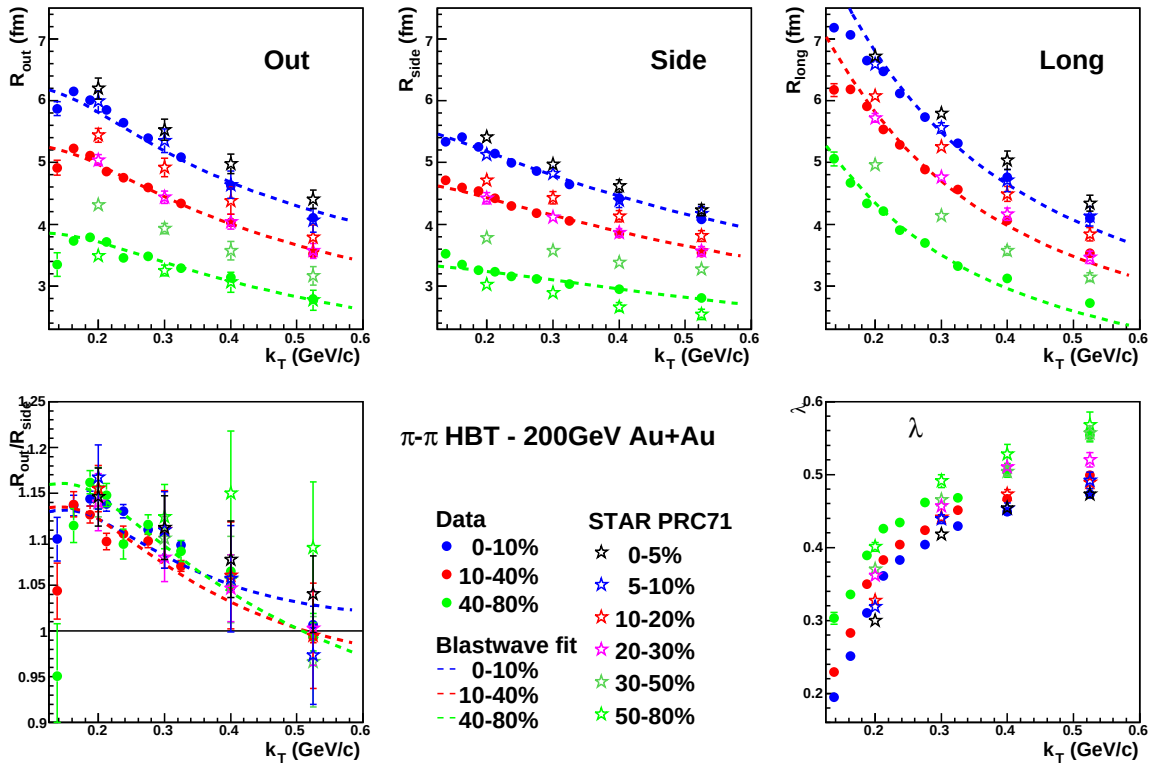

Figure 6.6: k_T dependency of the extracted Gaussian femtoscopic radii from the $\pi-\pi$ correlation function in $\sqrt{s_{NN}}$=200 GeV Au+Au collisions. The results are shown for the same three centrality bins as those used in the $\pi-\Xi$ analysis. The line shows blast wave fits to the data[74]. For comparison data from the previous STAR $\pi-\pi$ measurement [111] are included.

partially coherent emission of particles would lead to an increase of λ as well, but it was experimentally measured[117] that the emission of pions in heavy ion collisions is consistent with fully chaotic emission.

STAR experiment has already performed measurements of $\pi-\pi$ HBT at $\sqrt{s_{NN}}$=200 GeV[111]. However these measurements were done with at that time available statistics from Run II using only four k_T bins with lowest k_T of 200 Mev/c. In our analyses large fraction of the pions that are able to create low k^* $\pi-\Xi$ pairs are, due to π and Ξ acceptances, at or bellow p_T of 200MeV/c. Also the measurements were done for different centrality classes then we use. For these reason it was necessary, as a part of this analyses, to perform a new $\pi-\pi$ HBT measurement with higher statistics data sample of Run IV using exactly the same pion cuts as those used for π–Ξ analyses (as described in Section 6.2.2). Figure 6.5 shows example of the measured $\pi-\pi$ correlation function in the most central Au+Au collisions at $\sqrt{s_{NN}}$=200 GeV. The correlation functions were first corrected for the Coulomb interaction in the same way as in [111], using so called "Bowler-Sinyukov"

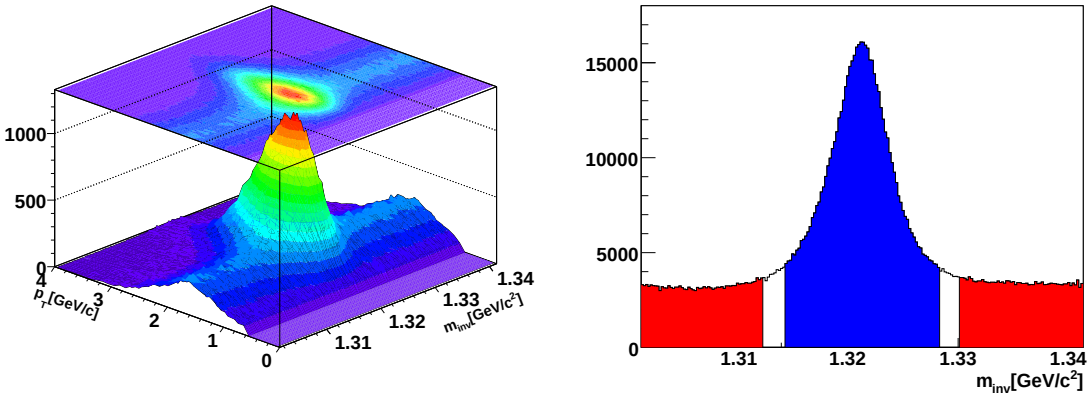

(a) (b)

Figure 6.7: (a)Invariant mass of the reconstructed Ξ^- as a function of its transverse momentum p_T. The data are from 10% most central Au+Au collisions at $\sqrt{s_{NN}}$=200 GeV. (b) The same data integrated over p_T. In blue is mass range used for analyses and calculation of the signal $|m_{inv} - m_{\Xi}| < 7$ MeV/c^2. In red is the range used for calculation of the background, on each side 9 MeV/c^2 $< |m_{inv} - m_{\Xi}| <$ 20 MeV/c^2.

procedure[195, 196]. This procedure is based on the fact that the strength of the correlation signal due to the Coulomb interaction is much less sensitive to the size of the source then the correlation coming from the quantum statistics. The correlation coming from the Coulomb interaction can then be corrected in the measured correlation function 3.41 by changing its parametrization into:

$$C_{\boldsymbol{K}}(\boldsymbol{q}) = (1-\lambda) + \lambda\, K_{coul}(\boldsymbol{q}) \exp\left[-q_{out}^2 R_{out}^2 - q_{side}^2 R_{side}^2 - q_{long}^2 R_{long}^2\right], \qquad (6.8)$$

where the introduced term $K_{coul}(\boldsymbol{q})$ is the squared two-particle Coulomb wave function 3.35 integrated over a Gaussian source of approximately the same extent as the fitted one.

The correlation function in 6.8 is fitted with the 3-dimensional Gaussian in Cartesian *out, side, long* coordinate system and in Figure 6.6 are shown the extracted R_{out}, R_{side}, R_{long}. Most importantly, for this analyses, in the same figure λ parameters are shown together with results from the previous STAR $\pi-\pi$ HBT measurement[111]. The $\sqrt{\lambda}$ from this figure is then used as p_T dependent pion purity $P(p_T)_\pi$ assuming that average p_T of the pions is the same as mean k_T of the corresponding k_T-bin of the $\pi-\pi$ correlation function.

Ξ purity

For Ξ the purity of the sample can be simply deduced from invariant mass plot of the reconstructed Ξ as a function of p_T as presented in Figure 6.7a. For each p_T bin of Figure 6.7a

the raw yield of Ξ is calculated as a sum of content of the m_{inv} bins under the mass peak within the range of ± 7 MeV/c^2 and the amount of background is estimated by linear fit to the background out of Ξ mass peak 9 MeV/$c^2 < |m_{inv} - m_{\Xi}| < 20$ MeV/c^2, as shown in Figure 6.7b. The results of this procedure are presented in Figure 6.8. As can be seen the majority of the reconstructed Ξ^* are in the p_T region of $1 < p_T < 3$ GeV/c. The samples for both used collision energies have purity of about 80% with the exception of the very low-p_T part of the Ξ spectra.

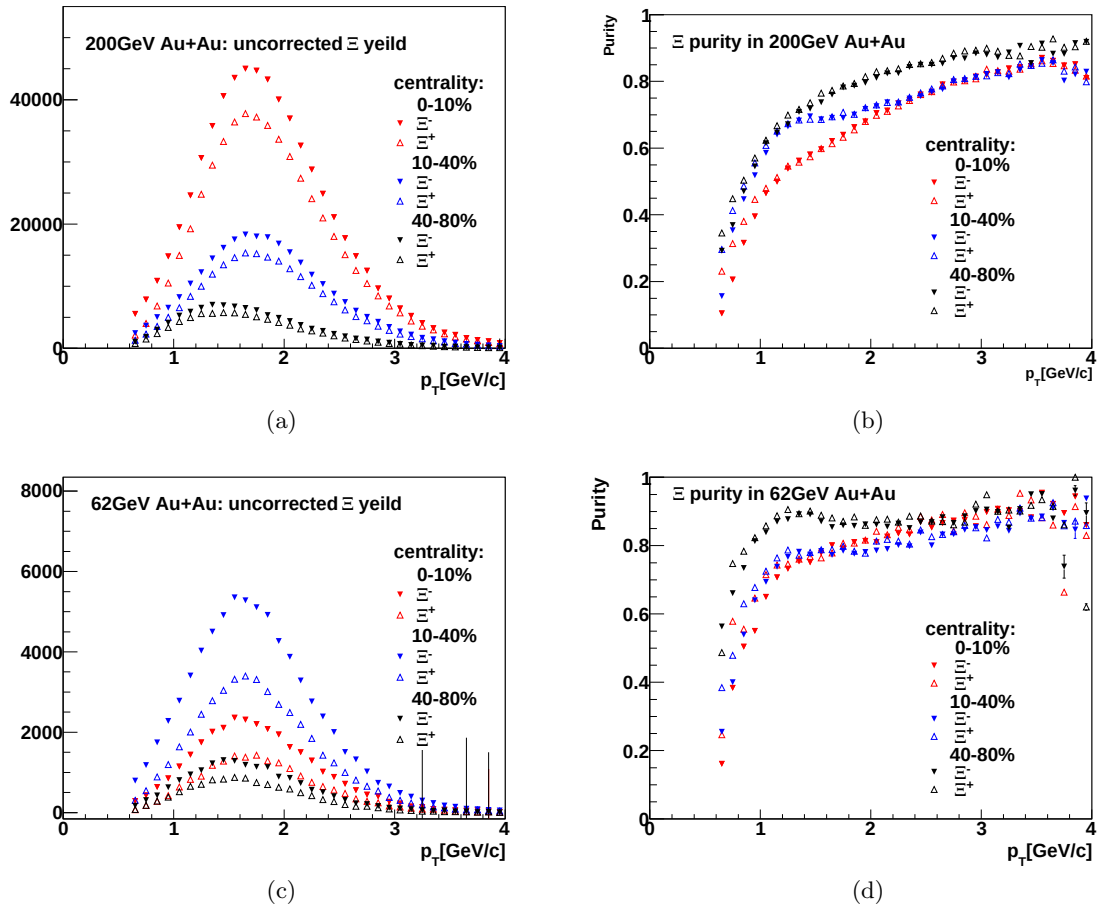

Figure 6.8: Extracted raw yield and purity of the Ξ samples as a function of transverse momentum p_T in Au+Au collisions at (a-b) $\sqrt{s_{NN}}$=200 GeV and (c-d) $\sqrt{s_{NN}}$=62 GeV collision energy.

pair purity

The purity of the $\pi-\Xi$ pairs $P(\vec{k}^*)$ for each bin of $\vec{k}^* = (k^*, cos\theta, \varphi)$ is a product of purity of pion and Ξ sample $P(\vec{k}^*) = P_{\pi}(\vec{k}^*)P_{\Xi}(\vec{k}^*)$. The individual single particle purities as function

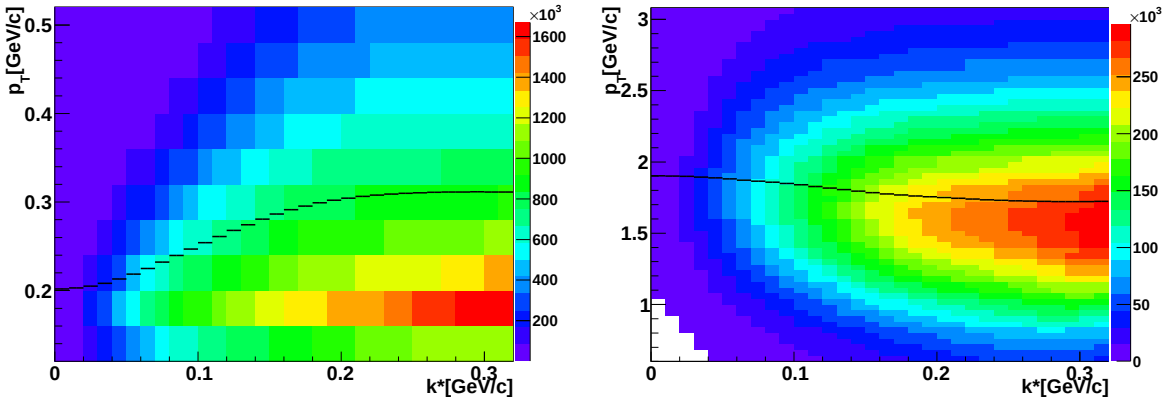

(a) (b)

Figure 6.9: p_T distribution of particles contributing to the $\pi-\Xi$ pairs of given k* for (a)π and (b)Ξ. The solid line shows and average p_T of the contributing particle.

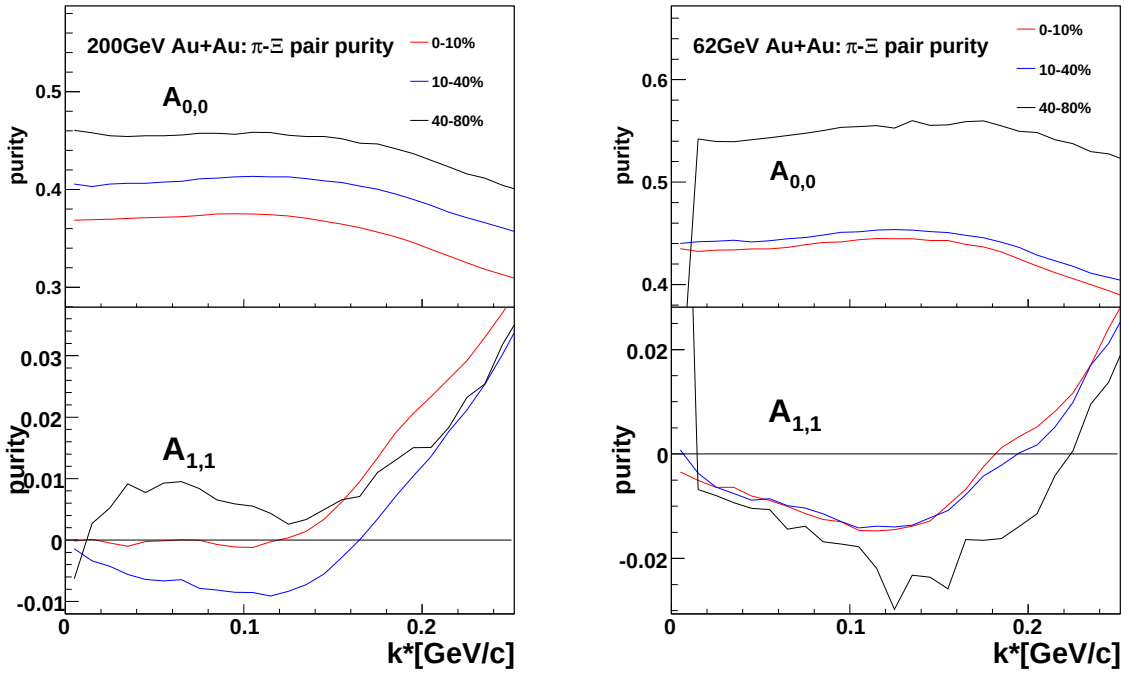

(a) (b)

Figure 6.10: Spherical decomposition of the purity of $\pi^- - \Xi^+$ pairs for three centralities of Au+Au collisions at (a)$\sqrt{s_{NN}}$=200 GeV and (b)$\sqrt{s_{NN}}$=62 GeV.

of $\vec{k}^*$ of the pair are calculated by convolution of the p_T dependent purities obtained in the the previous paragraphs with distributions of $\vec{k}^*(p_T)$ for both particles. In Figure 6.9 are shown the distributions of $k^*(p_T)$ for both π and Ξ . In the same figure is also shown the

average p_T with which both particles contribute to bin of given k^*. It can be seen that, mainly for pions, the mean p_T varies significantly with k^*. This is important for two reasons.

First, with conjunction of Figures 6.6 and 6.8, we expect that the final pair purity will also depend significantly on k^*. Moreover the pair purity may depend not only on the magnitude of the $\vec{k}^*$ vector, but may also be dependent on its direction. Hence using only single constant, such as the λ is used in $\pi-\pi$ HBT, for purity correction would lead to a distortion of the final $\pi-\Xi$ correlation function. For this reason purity correction has to be done bin by bin in 3-dimensional $\vec{k}^*$.

The contribution of particles with different p_T into different k^* bins is also important for the interpretation of results. In models, such as those based on hydrodynamic evolution, where is strong correlation between particles space-time emission point and its momentum the size of the measured homogeneity region changes with p_T of the particle.

The result of the convolution of single particle purities with distribution of $k^*(p_T)$ of the pairs is a 3-dimensional pair purity function $P(\vec{k}^*)$. To visualize the $P(\vec{k}^*)$ we can use the apparatus of the spherical harmonics decomposition introduced in Section 3.2.2 to see the influence of purity correction on not only the absolute height of the correlation function (coefficient $A_{0,0}$) but also on the extracted shift in the R_{out} direction given by the coefficient $A_{1,1}$. The spherical projections of the final pair purities are presented in a Figure 6.10. The figure shows that the purity correction can contain significant angular dependence, and full 3-dimensional purity correction is hence necessary.

6.4 Momentum resolution

Energy loss of the particles traversing the TPC together with limited momentum resolution during the track reconstruction induces uncertainty in determination of the $\vec{k}^*$ of the pair and may lead to systematic distortion of the measured correlation function. Theses effects of momentum resolution then have to accounted for in the analysis.

To estimate the magnitude of the distortion of the correlation function first the momentum resolution for both particles has to be quantified. This is done by embedding known simulated particles into the real data at the level of detector signal and passing the events down the whole reconstruction chain. The reconstructed momenta of the simulated tracks is then compared with the initially embedded ones in the following way. The real (initial) momentum

$$P_x = P\sin\theta\cos\varphi \quad P_y = P\sin\theta\sin\varphi \quad P_z = P\cos\theta \tag{6.9}$$

is altered by the reconstruction so that

$$(P,\theta,\varphi) \quad \longrightarrow \quad (P+\delta P,\theta+\delta\theta,\varphi+\delta\varphi), \tag{6.10}$$

where distributions for $\frac{\delta P}{P}, \delta\theta$ and $\delta\varphi$ are extracted from the embedding data and approximated by normal distribution - characterized by mean and width. The only distribution that has non-negligible mean is the $\frac{\delta P}{P}$ in the case of Ξ. This characterizes the mean change of the momentum due to the energy loss. In the case of pions the $\langle\frac{\delta P}{P}\rangle = 0$, because energy loss is accounted for during the track reconstruction by a Kalman filter procedure.

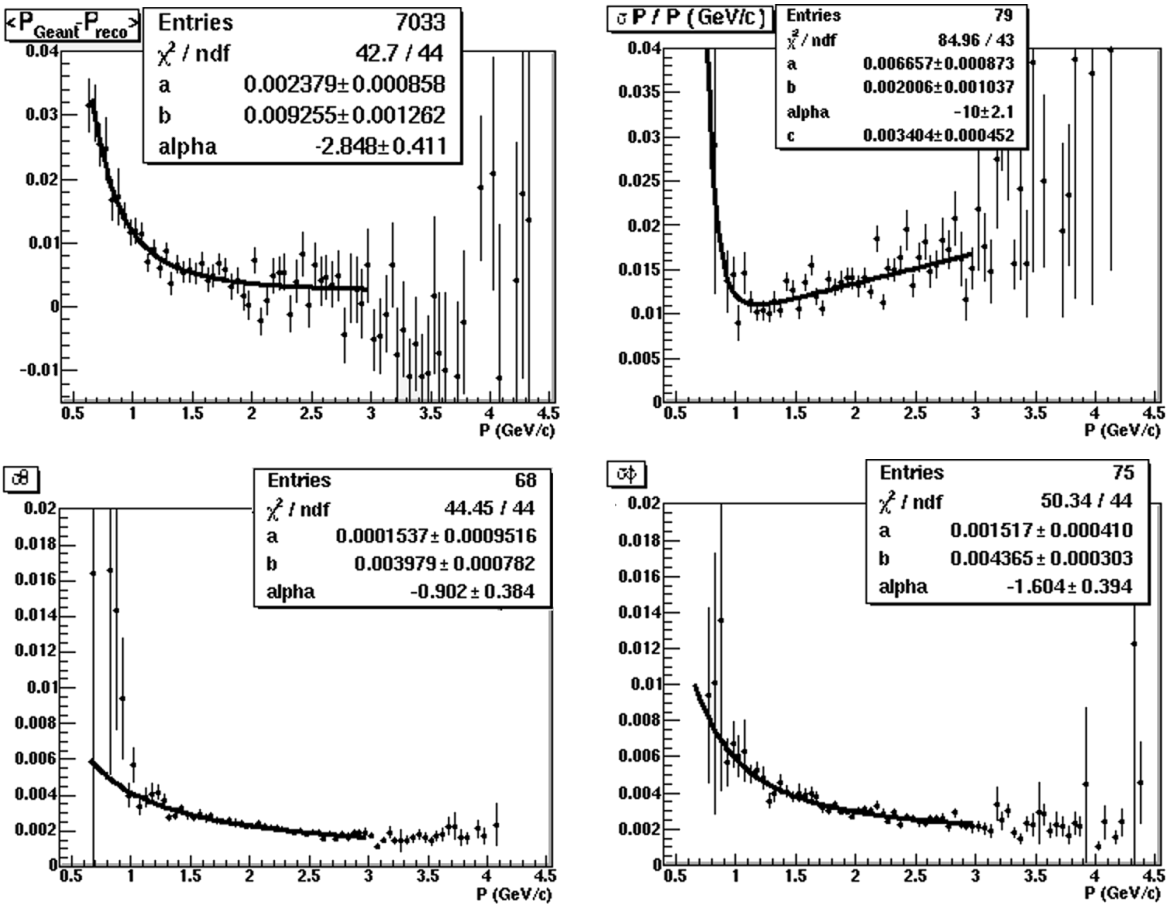

Figure 6.11: Momentum resolution, in form of parameters of Gaussian distribution, from Monte Carlo embedding of Ξ in the 0-10% most central collisions.

In Figure 6.11 there is an example of extracted parameters of the smearing distribution for Ξs in the most central dataset. Only those embedded Ξ that fulfill the same topological cuts after the reconstruction as the real ones are used. The data are fitted with momentum-dependent function

$$f(p) = a + bp^{\alpha} + cp \quad \text{or} \quad f(p) = a + bp^{\alpha}, \tag{6.11}$$

which is then used for corrections. Similarly as in the Figure 6.11 the parametrization of the smearing distributions are extracted for all centrality bins. In the case of pions, momentum resolution changes negligibly with centrality therefore the same parametrization is used for

all centralities, similar to one used in [193, 111]. The results of the parametrized smearing distribution are summarized up in the Figure 6.12.

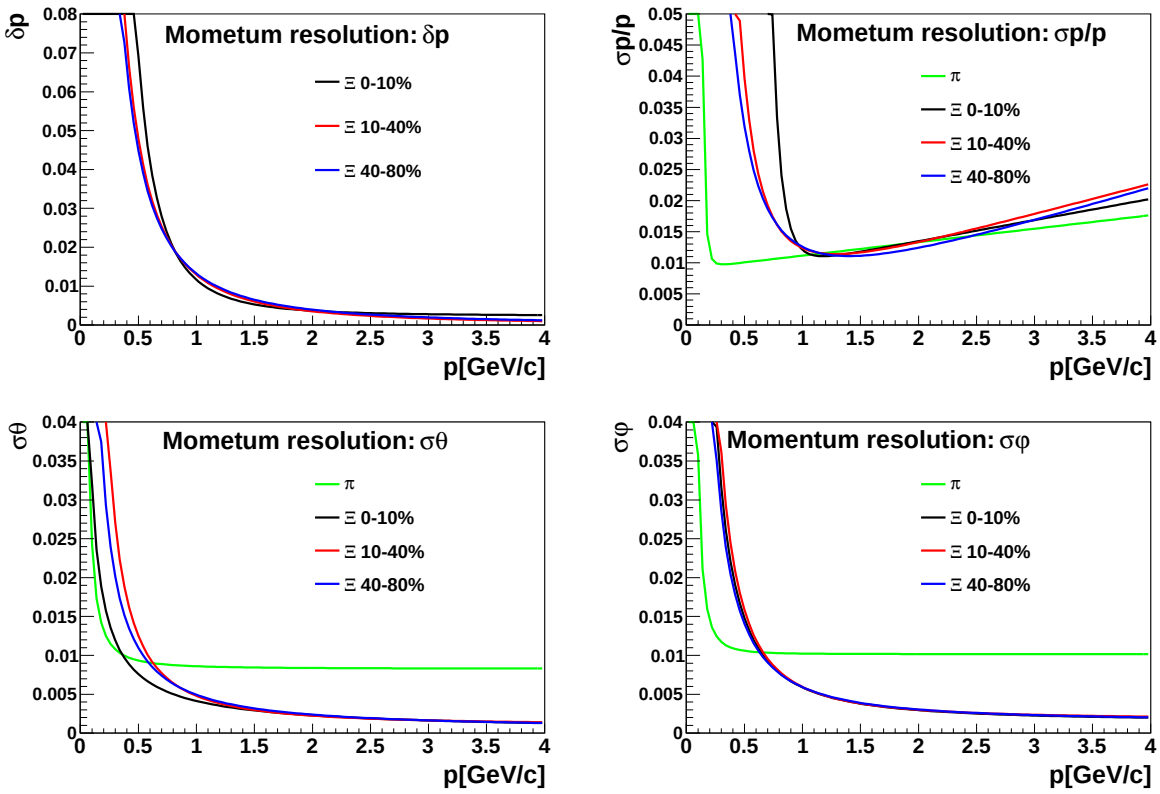

Figure 6.12: Centrality dependence of the π and Ξ momentum resolution.

To estimate the effects of the momentum resolution we show calculations of the correlation function. One without no momentum resolution taken into account and one with momentum resolution. The calculations shown in Figure 6.13 are done using a blast wave model with parametrization of *thermal freeze-out* as it will be described later on in Section 6.5.4. In the case of calculation with momentum resolution the particle momenta are in addition smeared according to 6.10 using parametrization 6.11 and values from Figure 6.12 The $\vec{k}^*$ of the pair is then recalculated and results of the calculation are inserted in the new (smeared) $\vec{k}^*$ bin. One can see from Figure 6.13 that the effects of the finite momentum resolution are very small except for the very lowest k^* bin. Since this bin in the measured correlation function suffers from very low statistics and hence does not influence significantly fits to the correlation function we can safely disregard the effects of the momentum resolution in the fitting and analyses of the $\pi-\Xi$ correlation function.

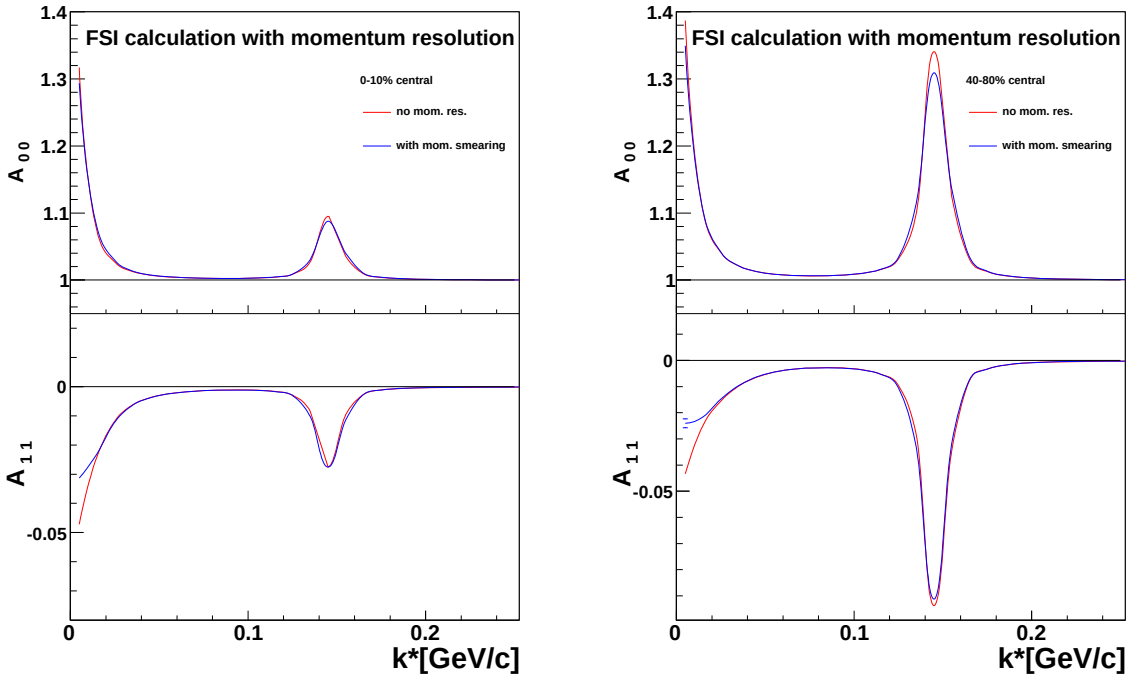

Figure 6.13: Comparison of calculated correlation functions when finite track momentum resolution is taken into account. The data and theoretical correlation function are from (a) the most central and (b) the most peripheral centrality bin.

6.5 Results

In the beginning of this section we briefly review results on π–π HBT that were obtained as a prerequisite for the main analyses. In the next part of this chapter we present results on π–Ξ correlations in Au+Au collisions at two different energies and their centrality dependence. In the second section information about the size of the source and relative shift between average emission points of the two particle species is extracted. Access to this information is of high importance as it is expected that the shift arises as a consequence of a transverse flow. For this reason the obtained results are compared in the last section with hydro-based simulations.

6.5.1 $\pi-\pi$ HBT and blast wave fits

The blast wave model, described in Section 3.3.1, has become a standard tool in describing the particle emission based on the information from measured spectra, v_2 and femtoscopy[109, 197]. Although the blast wave parameters for the $\sqrt{s_{NN}}$=200 GeV Au+Au collisions have already been obtained by the STAR collaboration in [111] it is of advantage

to recalculate them once again as the part of this analysis. The data used for this work is from new and statistically larger dataset and can provide a good cross check of the previous analyses. More importantly for the $\pi-\Xi$ correlations, we use different (larger) centrality bins and the obtained blast wave parameters can be used to parametrize the source of pions in the calculations of $\pi-\Xi$ correlation function within the same centrality bins. Since for comparisons with models we only use the highest statistics $\sqrt{s_{NN}}$=200 GeV data, the blast wave model also fitted only to the $\sqrt{s_{NN}}$=200 GeV $\pi-\pi$ data.

Centrality (%)	T (MeV)	ρ_0	R (fm)	τ (fm/c)	$\Delta\tau$ (fm/c)
0–10	98 ± 2	1.02 ± 0.01	12.6 ± 0.1	8.5 ± 0.2	2.55 ± 0.15
10–40	106 ± 2	0.93 ± 0.01	10.4 ± 0.1	6.8 ± 0.1	1.98 ± 0.10
40–80	120 ± 2	0.76 ± 0.01	7.1 ± 0.1	4.5 ± 0.2	1.36 ± 0.14

Table 6.4: Extracted parameters from a blast wave fit to pion HBT radii at $\sqrt{s_{NN}}$=200 GeV.

The measured $\pi-\pi$ radii were already shown in the Figure 6.6. The obtained results together with measured spectra of pions, kaons and protons[67] and v_2[91] at the same energy were used, similarly as in [111], to obtain the blast wave parameters. Since HBT results with respect to the event plane are not available we can fit only 5 blast wave parameters: T, R, ρ_0, τ, and $\Delta\tau$. The extracted parameters are presented in Table 6.4 for the three centrality bins used in this analysis.

To compare with previous results of [111] a comparison of the obtained blast wave parameters from this work and from [111] is presented in Figure 6.14. As can be seen the newly obtained parameters agree well with the previous measurements. The obtained temperature T is little higher than the published one, but this parameter is mainly driven by the measured spectra. If, for example, only spectra of pions was used in the fit the extracted T would be lower while other parameters would change only marginally.

6.5.2 1-dimensional $\pi-\Xi$ correlation functions

Using cuts and procedures described in the previous section we have obtained correlation functions for each of the charge combinations of $\pi^{\pm}$–$\Xi^{\pm}$ pairs for the three centrality classes as defined in the Table 6.2 and Table 6.3. Purity-corrected 1-dimensional correlations functions $C(k^*)$ are presented in Figure 6.15 as a function of $k^* = |\vec{k}^*|$ for the Au+Au collisions at $\sqrt{s_{NN}}$=200 GeV and $\sqrt{s_{NN}}$=62 GeV. All correlation function are normalized to unity in a region where no FSI effects are present. Since the correlations due to FSI effects may reach in our case to more then 150 MeV/c the normalization region was chosen to be 200 MeV/c < k^* < 400 MeV/c.

For all charged combination the low k^* region ($k^* < 0.05$ GeV/c) of the correlation function is dominated by the Coulomb interaction - positive(attractive) for unlike-sign and

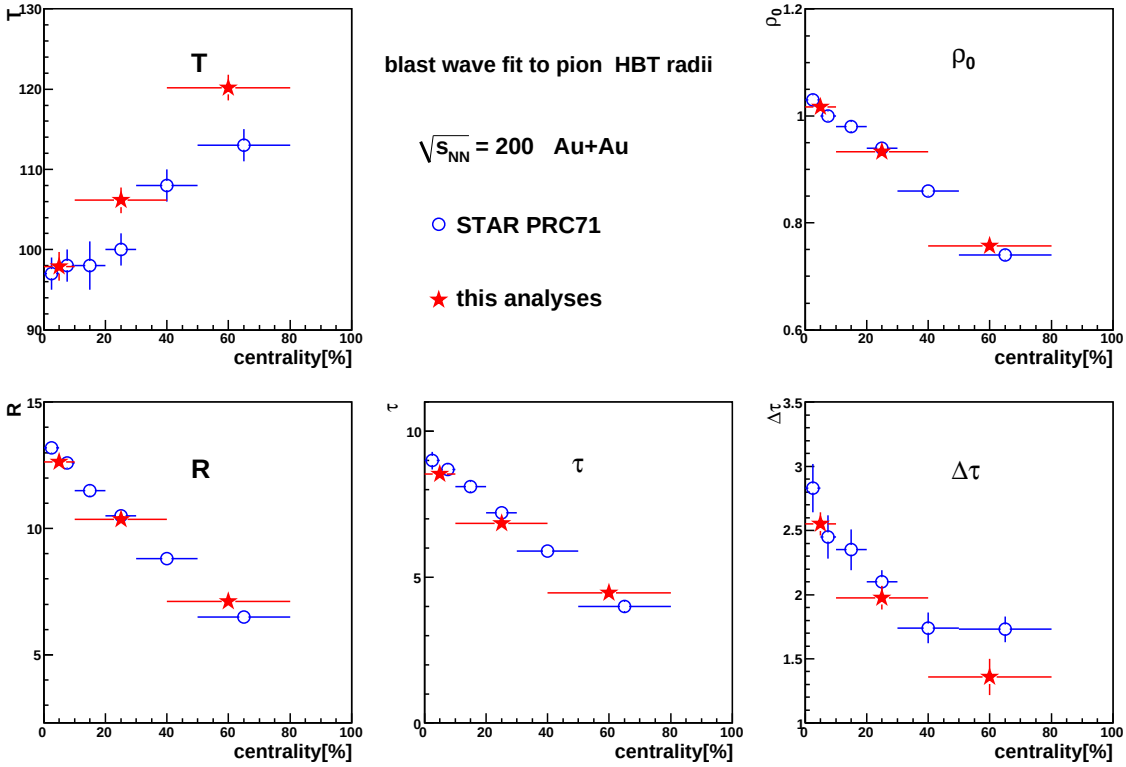

Figure 6.14: Comparison of blast wave parameters of obtained from fits to $\pi-\pi$ HBT. In blue are previously published results in [111] and in red are results obtained in this analysis. While vertical error bars show statistical errors the horizontal ones depict merely width of the used centrality bin.

negative(repulsive) for like-sign pairs. Since both particles are hadrons they interact also strongly. The strong interaction between π and Ξ is not well known, but the total cross section of interactions involving multi-strange baryons is often assumed to be small [198, 199, 200, 84, 201]. One can seen in the Figure 6.15 that in the case of unlike-sign $\pi-\Xi$ pairs there is pronounced peak at $k^* \simeq 150$ MeV/c. This peak corresponds to strong interaction between π and Ξ via a resonance. For two particle decay the k^* used in the correlation function is the same as the decay momentum of the system in its CMS. The k^* is then directly connected to the invariant mass M_{inv} of the system by

$$k^* = \frac{[M_{inv}^2 - (m_\pi - m_\Xi)^2]^{1/2}[M_{inv}^2 - (m_\pi + m_\Xi)^2]^{1/2}}{2M_{inv}}. \tag{6.12}$$

The peak at $k^* = 150$ MeV/c then corresponds to $\Xi^*(1530)^0$ resonance [13]. Although the $\Xi^*(1530)$ is a well established resonance this analysis is a first observation of this resonance in the high track multiplicity environment of ultra-relativistic collisions of heavy ions.

The presence of the Ξ^* in the correlation function can be checked using 6.12 by creating

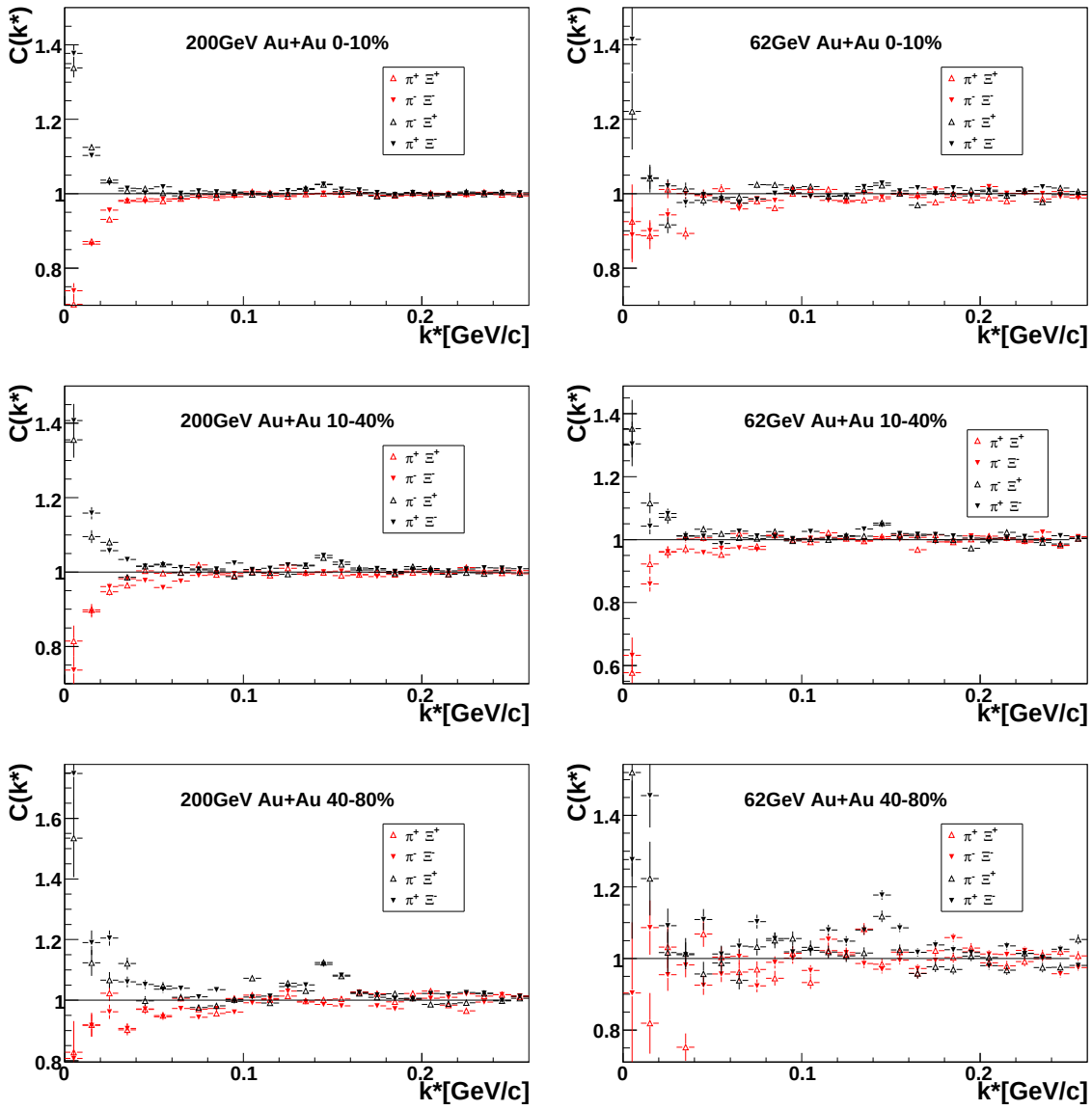

Figure 6.15: Results on 1-dimensional $\pi-\Xi$ correlation function for all combinations of charged $\pi^{\pm}$, $\Xi^{\pm}$ in three centrality bins in of Au+Au collisions at (left)$\sqrt{s_{NN}}$=200 GeV and (right)$\sqrt{s_{NN}}$=62 GeV. The correlation functions have been corrected for purities of the π, Ξ samples. All correlation functions are normalized at 200 MeV/c < k^* < 400 MeV/c.

a background-subtracted invariant mass spectrum of the unlike-sign $\pi-\Xi$ system. This mass spectrum is easily obtained as a "by-product" of the femtoscopic analyses by using subtraction instead of division in the formula 3.39, as function of M_{inv} instead of k^*. Such a mass spectrum for mid-peripheral bin (10-40%) at $\sqrt{s_{NN}}$=200 GeV with combined statistics of π^+–Ξ^- and π^-–Ξ^+ pairs is shown in Figure 6.16. This plot, since it covers large interval of M_{inv} (and thus large interval of k^*) presents a good opportunity to demonstrate the influence

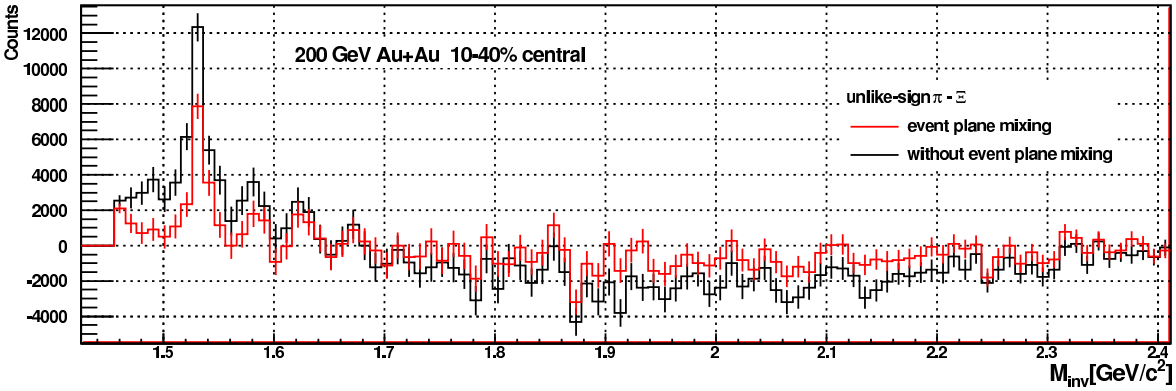

Figure 6.16: Invariant mass of the combined unlike-sign $\pi - \Xi$ pairs after subtraction of background distribution created by event-mixing. Two different backgrounds were used: (black) with events mixed within groups with similar multiplicity and vertex position and (red) with additional grouping in the orientation of the event plane.

of used event mixing technique discussed before in Section 6.2.3. The plot contains results from the same dataset obtained with two different methods of event-mixing used to obtain the uncorrelated background for subtraction. The difference between the two presented results lies in the use of event plane as one of the three event mixing parameters (the other two being multiplicity and main vertex position). While both results in Figure 6.16 show a clear peak at mass corresponding $\Xi^*(1530)^0$, the events that are mixed in bins with similar orientation of event plane (red color) show significant improvement in the shape of the background outside of the mass peak. This is of importance for the construction of correlation functions as this is the region used for the normalization of the correlation function. Proper normalization of the correlation function has in turn strong effect on the quality of fits and extraction of the source sizes.

Returning back to the correlation functions, we can see in Figure 6.15 that the results within the precision given by error bars agree well between like-sign $\pi^- - \Xi^-$, $\pi^+ - \Xi^+$ and unlike-sign $\pi^- - \Xi^+$, $\pi^+ - \Xi^-$ pairs. Therefore to increase further the available statistics we combined together data for like and unlike-signed $\pi - \Xi$ pairs into two combined correlation functions. This summation must, of course, be done on the level of numerator and denominator distributions of 3.39. The centrality dependence of the combined 1-dimensional like and unlike-sign pairs is shown in Figure 6.17 for both collision energies. In both of them we can observe that while the Coulomb part still suffers by small statistics for most of the data and shows rather small sensitivity to centrality of the collision, the correlation in the Ξ^* peak manifests significant dependency on the centrality. Its strength increases from central to the peripheral collisions as we expect - the correlation being strongest for the smallest system.

Since the Ξ^* peak exhibits good sensitivity to the size of the source we can compare the unlike-sign correlation functions in this region to qualitatively study the dependence of

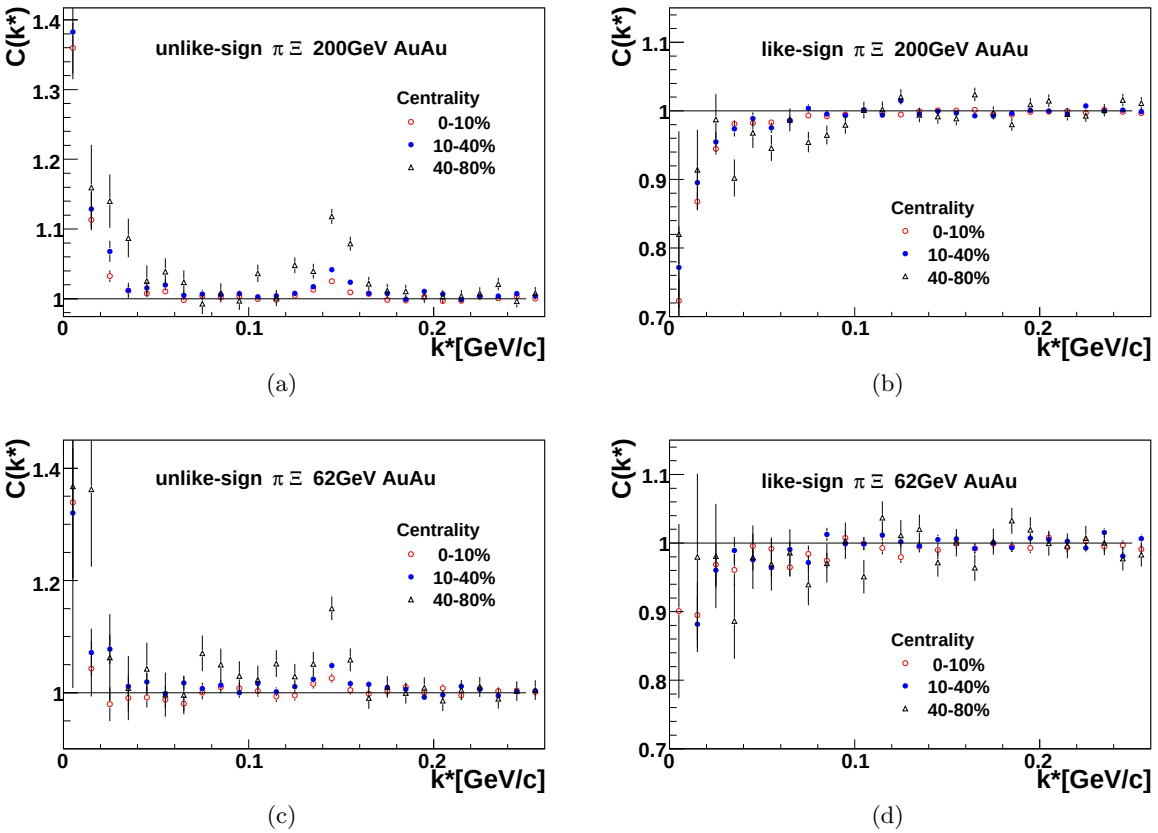

Figure 6.17: Top: The centrality dependence of the correlation function at $\sqrt{s_{NN}}$=200 GeV for combined (a) unlike-sign (b) like-sign $\pi-\Xi$ pairs. Bottom: The centrality dependence of the correlation function at $\sqrt{s_{NN}}$=62 GeV for combined (e) unlike-sign (f) like-sign $\pi-\Xi$ pairs.

the source size on the collision energy, which would otherwise be hard to compare via the statistically impaired Coulomb part. Correlation functions for unlike-sign pairs for both energies and all centralities are directly compared in Figure 6.18. One can see that we do not observe a significant dependence of the $\pi-\Xi$ source on the collision energy that would manifest in the different magnitudes of the Ξ^* peak. This result is similar to that obtained in $\pi-\pi$ measurements [109] that also show only weak increase of the measured pion radii on the energy of the collisions.

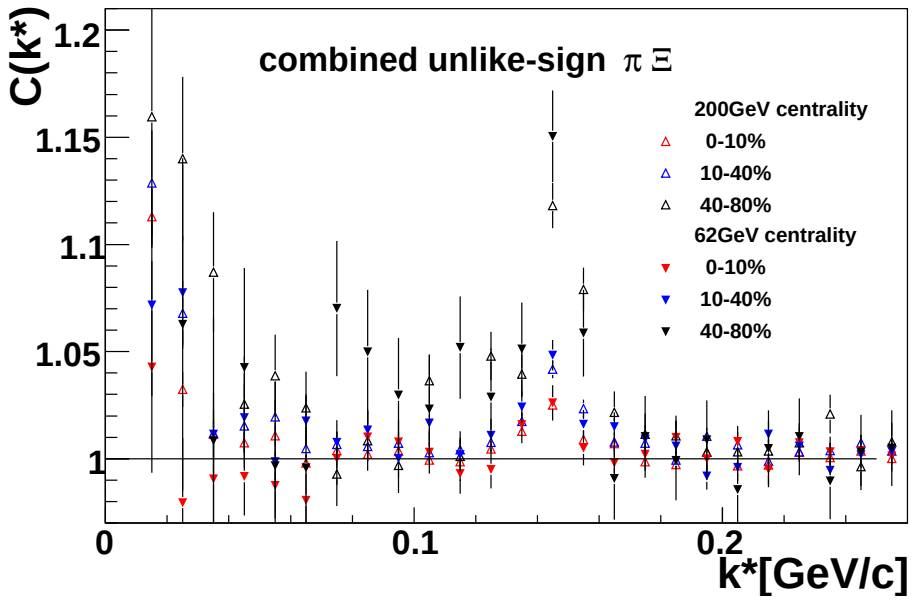

Figure 6.18: Comparison of unlike-sign correlation functions for all three centralities at $\sqrt{s_{NN}}$=200 GeV and $\sqrt{s_{NN}}$=62 GeV.

6.5.3 Emission asymmetry

As mentioned before in Section 2.3 current data suggest than Ξ develops substantial flow and possibly decouples from the system before other particles. Both of these phenomena can create an asymmetry between average emission point of pions and Ξs. As described in Section 3.1.4 the information about this shift is contained in the angular part of the 3-dimensional correlation function $C(\vec{k}^*) = C(k^*, \theta, \varphi)$. To access this information a decomposition 3.43 of $C(\vec{k}^*)$ into the spherical harmonics is used. The coefficients from the decomposition which are of interest to us ($A_{0,0}$ and $A_{1,1}$) are presented in Figure 6.19. Because of the available statistics we can only extract the information about the shift, contained in the $A_{1,1}$ coefficient, from the data at $\sqrt{s_{NN}}$=200 GeV collision energy. In the dataset at $\sqrt{s_{NN}}$=62 GeV the coefficient $A_{1,1}$ is dominated by statistical errors. Out of the available three centrality bins at $\sqrt{s_{NN}}$=200 GeV the statistically most significant is the most central one. In this centrality bin we can use not only the Ξ^* part of the correlation function, but also the low-k^* Coulomb region.

6.5.4 FSI calculations

The easiest way to learn something from the measured correlation function is to compare it qualitatively with a calculated theoretical prediction using some simple prescription or model for the emission function. To calculate the correlation function according to 3.33 we need to understand the two-particle interaction - be able to calculate the two-particle

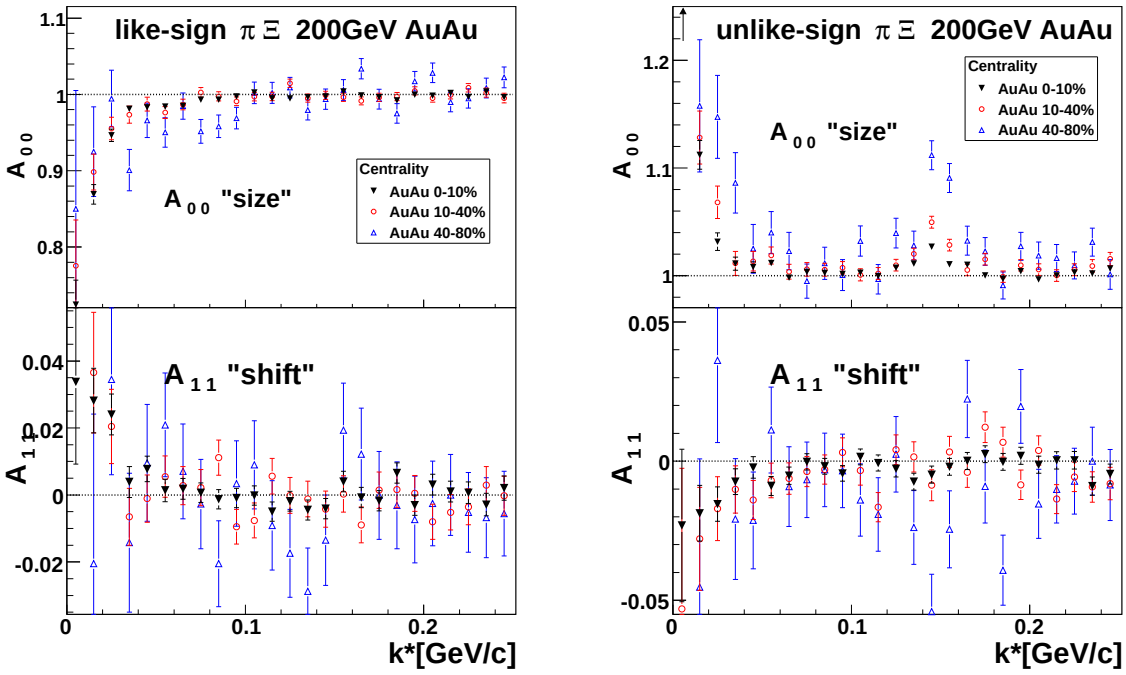

(a) (b)

Figure 6.19: Centrality dependence of the coefficients $A_{0,0}$ and $A_{1,1}$ of spherical decomposition of the 3-dimensional $\pi-\Xi$ correlation function in Au+Au collisions at $\sqrt{s_{NN}}$=200 GeV. Data are combined for a) like-sign and b) unlike-sign $\pi-\Xi$ pairs.

wave-function 3.6. Calculation of $\pi-\Xi$ interaction in the final state is highly non-trivial as the two particles interact not only by Coulomb interaction, but also via a strong interaction going trough a resonance. In this case the strong interaction cannot be simply neglected as it is done for example in the system of identical pions.

At this moment there exist three models for calculating the $\pi-\Xi$ FSI which include the Ξ^* (1530) resonance. The first model was developed by Pratt and Petriconi [202] and has been used in most of our published studies [203, 204]. The newer model was made by Kerbikov and Malinina [205, 206] and the most recent model was made Lednicky [207]. In this work we use the model of Pratt&Petricony which agrees in results well with model of Lednicky.

Gaussian source

The simplest model for the two-particle emission function $S_{PS}(\boldsymbol{r}, \boldsymbol{q})$ is the Gaussian parametrization 3.27. In the Gaussian parametrization there is no correlation between particle momenta and emission coordinates. The emission function hence factorizes into momen-

tum and position distributions. In our case of the two non-identical particles with a large difference in mass we will use Gaussian parametrization of the emission function $S_{PS}(\boldsymbol{r^*}, \boldsymbol{k^*})$ in the center of mass system (CMS) of the of pair. The parametrization is analogous to 3.27, but with separate radii for the two particle species:

$$S_{PS}(\boldsymbol{r^*}, \boldsymbol{k^*}) \sim \exp\left[-\frac{(r^*_{out} - \Delta r^*_{out})^2}{2\left[R^2_{\pi,out} + R^2_{\Xi}\right]^2} - \frac{r^{*2}_{side}}{2\left[R^2_{\pi,side} + R^2_{\Xi}\right]^2} - \frac{r^{*2}_{long}}{2\left[R^2_{\pi,long} + R^2_{\Xi}\right]^2}\right]. \quad (6.13)$$

To compare the measured results with calculations we have used for pions the Gaussian radii obtained from the measurements of the $\pi-\pi$ HBT in Figure 6.6. To describe the whole source, for given centrality, with one set of radii we use the parameters measured in the lowest k_T bin ($150 - 250$ MeV/c) in Figure 6.6 since this corresponds to the average p_T of pions in this analysis. As the standard $\pi - \pi$ HBT measurements are done in the LCMS system the R_{out} radii have to be adjusted by corresponding γ factor for the pair CMS. For the Ξ we have used a single radius, estimation of which is based on the assumption of the flow of Ξ. If the Ξ flows as other particle species the size of its source (homogeneity region) is expected to follow similar $\sim \frac{1}{\sqrt{m_T}}$ scaling as observed for other particle species in Figure 3.9. The radius can be estimated as ~ 2 fm. Similar prediction can be obtained from blast wave parametrization under the flow assumption. Note that the radii actually depend on the p_T and since we don't differentiate in p_T this is a sufficient estimate. Moreover since the Ξ source is small the overall extent of the source in 6.13 will be dominated by the pion radii. The Gaussian radii used for calculations are shown in Table 6.5.

Centrality (%)	$R_{\pi,out}$	$R_{\pi,side}$	$R_{\pi,long}$	Δr^*_{out}	R_{Ξ}
0–10	10.2	5.4	7.1	-8.0	2
10–40	8.9	4.5	5.9	-6.0	2
40–80	6.3	3.3	4.7	-4.0	2

Table 6.5: Parameters for calculations of the $\pi-\Xi$ correlation function with the Gaussian description of the source in the pair CMS at $\sqrt{s_{NN}}$=200 GeVcollision energy.

In Figure 6.20a is shown the calculation using the Gaussian radii from Table 6.5 with the two sources having no average relative shift in the *out* direction, $\Delta r^*_{out}= 0$. From the already presented $\pi-\Xi$ correlation function we know that there is an actual relative shift present in the system as the coefficient $A_{1,1}$ is non-zero. To account for this we introduce "by hand" a shift in the *out* direction Δr^*_{out} between pions and Ξs. The orientation (sign) of the Δr^*_{out} is chosen negative which in our notation corresponds to the case of Ξs emission coordinates being positioned more to the outside of the source. The values of the chosen Δr^*_{out} are also in the Table 6.5. The results of the calculations after introduction of the shift Δr^*_{out} are shown in the Figure 6.20b.

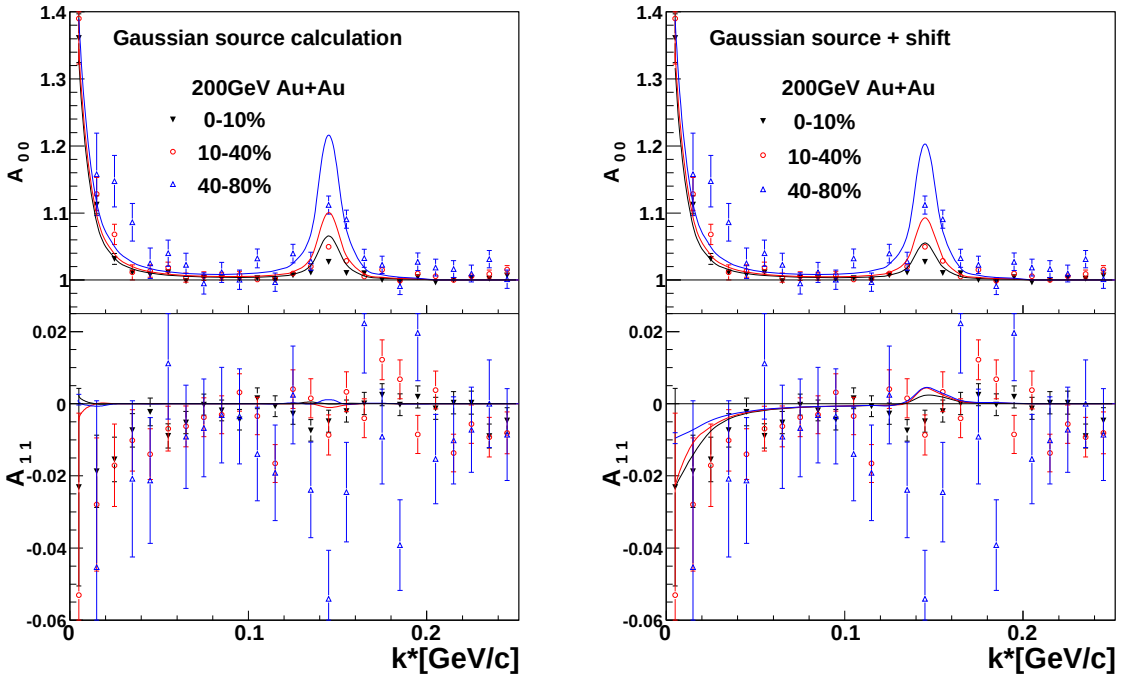

(a) (b)

Figure 6.20: Comparison of the measured correlation functions with FSI calculations using Gaussian parametrization of the source. (a) no shift in the *out* direction and (b) introduced shift between average emission point of π and Ξ. The used parameters are in Table 6.5.

The calculations with $\Delta r^*_{out}= 0$ in Figure 6.20a show similar behavior as the measured data. The correlation function exhibits small sensitivity to the size of the source in the Coulomb (low k^*) region and high sensitivity in the Ξ^* region. It must be pointed out that however that the calculated correlation function shows discrepancy when compared to the real data. Theoretical calculations in the Coulomb part lie at or slightly bellow the data for all the centralities which would suggest that the actual real source is smaller than the one used in the calculations. However in the much more sensitive Ξ^* region the calculations, in all centrality bins, strongly overshoot the data. This would mean the opposite - that the real source is actually larger. Since we have set the $\Delta r^*_{out}= 0$ the coefficient $A_{1,1}$ vanishes in this calculations.

We can try to improve the agreement between data and calculation by an introduction of a non-zero shift Δr^*_{out} (Figure 6.20b). The strength of the correlation in the $A_{0,0}$ coefficient exhibits the same behavior as in the previous case. The $A_{1,1}$ is now non-zero and we see that it qualitatively agrees with the data in the low k^* region. This shows that indeed the shift observed in the measured data is oriented so that the Ξs are emitted on average more

toward the outer edge of the source - as suggested by models containing collective flow. Problem is present again in the resonance region - here the coefficient $A_{1,1}$ has an opposite sign compared to the low k^* part. Even though this may naively suggests an interpretation of different sign of the shift between Coulombicaly and strongly interacting pairs the real reason for this discrepancy is that the $\pi-\Xi$ vawefunction describing the strong interaction via Ξ^* resonance depends non-trivially on the angle θ^* between $\vec{k}^*$ and $\vec{r}^*$ [207]. The distribution of θ^* in each $\vec{k}^*$ bin is given by the relation between momenta and emission coordinates of the particles that contribute to the bin. As the simple Gaussian model of the emission function lacks any x-p correlations it cannot describe properly changes of the source homogeneity lengths and relative shifts with p_T and k^*.

For a better description we need to turn to models that describe betters dynamics of the system and include such correlations.

Blast wave parametrization

The blast wave model has been highly successful in describing the $\pi-\pi$ measurements. Flow induced x-p correlations included in the model seem to describe well the m_T dependence of the pion HBT radii (Figure 6.6 and Table 6.4). Since the collective flow of multi-strange baryons is one of the main motivations for this analyses, it is of interest to see if the same model can be used to describe the Ξ source as well.

Even more interesting question then is if using the hydro-inspired blast wave model we can distinguish two different scenarios of multi-strange baryon production. The first one is what we call the "*thermal freeze-out*". In this scenario the Ξs undergo the same evolution as the rest of the system including the hadronic phase in which they interact with the rest of the system (predominantly pions) and decouple at the same time as pions. The second scenario is the so called "*early freeze-out*" of multi-strange baryons as suggested by the results on multi-strange baryon spectra and v_2 presented in Section 2. In such a scenario the multi-strange baryons are emitted at or shortly after the chemical freeze-out of the system and do not participate in the subsequent evolution of the hadronic matter.

In the first case of *thermal freeze-out* we would assume that the freeze-out configuration of the Ξ source can be described with the similar blast wave parameters as the pion source in Table 6.4. In the case of *early freeze-out* the configuration of the Ξ source, described by the blast wave model, will be different from the source of pions. In this case we can make only reasonable assumptions about what would be the parameters of the blast wave model describing such a scenario. If the Ξs decouple at earlier time we can expect the source being smaller and the temperature higher. The temperature parameter for the case of *early freeze-out* was set to values extracted from measurements of spectra of multi-strange baryons. The parameters used for calculating the theoretical correlation functions using the blast wave

	0-10%		10-40%		40-80%	
	thermal	early	thermal	early	thermal	early
T (MeV)	98	156	106	156	120	156
ρ_0	1.02	0.75	0.93	0.75	0.76	0.75
R (fm)	12.6	3.	10.4	2.5	7.1	2.
τ (fm/c)	8.5	2.	6.8	2.	4.5	1.5
$\Delta\tau$ (fm/c)	2.55	0.05	1.98	0.05	1.36	0.03

Table 6.6: Blast wave parameters used for FSI calculation at $\sqrt{s_{NN}}$=200 GeV collisions energy. The parameters describing *thermal freeze-out* are from fits to pion data[111]. The parameters for the *early freeze-out* are altered in accordance with data on multi-strange spectra and v_2[92].

source parametrization for both scenarios are in Table 6.6.

The inclusion of the x-p correlation in the blast wave model has a consequence for the procedure of the actual calculation of the correlation function. Because of the changing acceptance of the detector with p_T and η of tracks, plus the varying reconstruction efficiency of Ξ the contribution of particles with different momenta varies for individual $\vec{k}^*$ bins (Figure 6.9). For this reason we cannot take simply the thermal momentum distribution for each particle or even the momentum distribution from the blast wave model as we would get different single-particle spectra inside the $\vec{k}^*$ bins. Instead, in our approach we use a two-particle distribution created during even mixing technique. This means that as we create the uncorrelated background distribution of $\pi-\Xi$ pairs for 3.39 we save the information about the momenta of both particles. When we calculate the theoretical correlation function we do not generate the momenta of particles, instead we load the saved pairs and generate only emission points for the particles of given momenta. Since the statistics in some of the low k^* bins, especially in the 3-dimensional correlation function, may not be high enough and the random generation of emission coordinates could cause fluctuations of results from one calculation to another we generate the coordinate for each used pair multiple times (usually$\sim$50) and take the averaged value of the FSI.

In the Figure 6.21 are compared blast wave calculations with real data using the same parameters of the *thermal freeze-out* for both π and Ξ sources. Compared to the previous calculations with Gaussian sources the coefficient $A_{1,1}$ in the region of Ξ^* is non-zero and has the same sign as in the region of Coulomb interaction. This demonstrates that the x-p correlations in the emission of particles are necessary to at least qualitatively describe the $\pi-\Xi$ correlation function.

Despite the improvement of the correlation function when using the blast wave model there is again a significant disagreement in the strength of the correlation signal in both $A_{0,0}$ and $A_{1,1}$ coefficients. While in the Coulomb region the calculated correlation functions

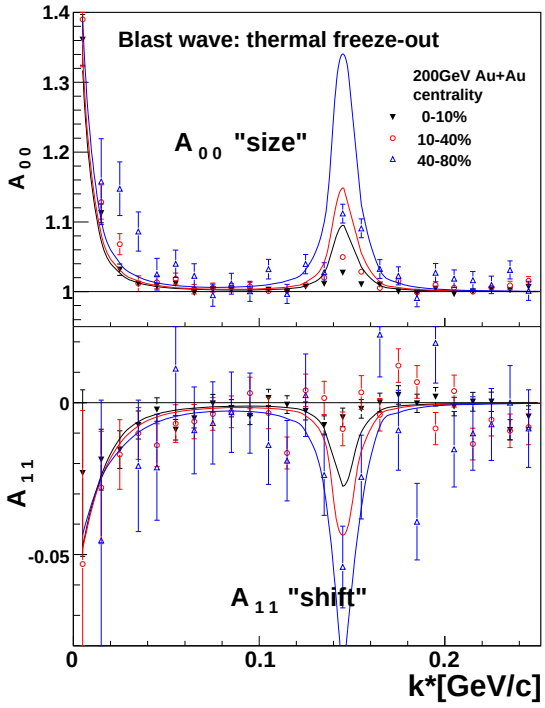

Figure 6.21: Comparison of the measured correlation function with blast wave calculations for the *thermal freeze-out* scenario when both particle species are described by the same set of parameters.

seems to be at or slightly bellow the measured data the calculation strongly overestimates both the size ($A_{0,0}$) and the shift ($A_{1,1}$) in the Ξ^* region.

It is then interesting to see if the theoretical prediction will improve when we consider the *early freeze-out* scenario of Ξ. In Figure 6.22 are compared the measured correlation functions from the central and mid-peripheral data with the calculations for the *thermal* and *early freeze-out* scenarios. The former is the same as in the Figure 6.21 and the latter is obtained by changing the blast wave parameter for Ξ to those marked in Table 6.6 as "early". Even though we have introduced quite significant changes to the blast wave parameters describing the Ξ early freeze-out when compared to the thermal (late) one the change in the calculated correlation function is rather subtle. There is only a small increase in absolute magnitude of the $A_{0,0}$ and $A_{1,1}$ coefficients in the Ξ^* region. The most notable difference between the two scenarios is in the Coulomb part of the $A_{1,1}$ coefficient.

To understand why a big change in parameters of the blast wave model generates only a small change in the calculated correlation function we need to take into an account equation 3.38. Here the shift between the average emission points of the two particle species is a combination of a space and time component. When we consider the *early freeze-out*

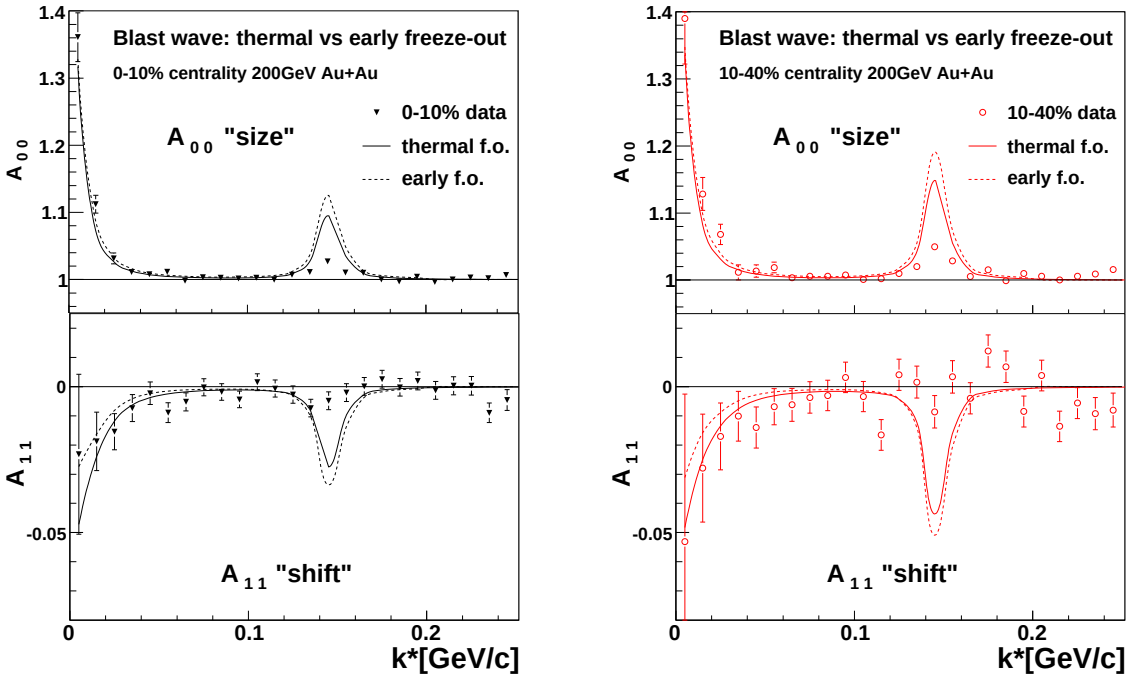

Figure 6.22: Comparison of the measured correlation function with blast wave calculations for the *thermal freeze-out*ans *early freeze-out* scenarios for central and mid-peripheral data at $\sqrt{s_{NN}}$=200 GeV collisions.

scenario we expect the Ξs to decouple at earlier time, $\Delta\bar{t} > 0$. At the same time the Ξs are emitted from a smaller source, smaller meaning the size of the whole source (parameter R) not necessarily homogeneity region, thus closer to the center of system. This means that while $\Delta\bar{t} > 0$ grows to positive values the $\Delta\bar{x}_{out} > 0$ goes from negative value toward zero. These both changes may well compensate in the formula 3.38 which explains the relatively low sensitivity of the correlation function to those two scenarios of Ξ emission. This topic will be explored more in Section 3.3.2 where an example of such an interplay between spatial and time component of the shift is shown in Figure 6.34.

Since changing from *thermal* to *early* freeze-out of Ξ did not bring , within the blast wave model, calculations closer to the data we need to consider other explanations. One possible explanation may lie in the absence of the correlation between emission position and emission time; the x-t correlation. Most recent theoretical advances[122, 147, 208] show that x-t correlations are indeed important in explaining the $\pi-\pi$ HBT measurements, namely the R_{out}/R_{side} ratios. The inclusion of the x-t correlations in the emission function of both π and Ξ, as it is present in detailed hydrodynamical models, could in future lead to a better agreement between the calculated and measured correlation function.

6.5.5 Coulomb fitting

To understand better the correlation function and its implication for the study of the emission of particles in the heavy-ion collisions we need to get quantitative information by fitting the data. In the previous section we have demonstrated that we cannot consistently explain at the same time the Coulomb and strong interaction part of the correlation function using neither simple Gaussian model nor the more advanced blast wave model of the emission. We have also demonstrated that relying on the theoretical calculation in Ξ^* region may be principally problematic as it is not clear what amount of correlation needs to be present in the model to correctly describe the changing properties of the homogeneity region with p_T and $\vec{k}^*$ of the pair. Moreover theoretical framework for calculating the FSI was developed for $k^* \simeq 0$ and it is a question to what degree the *smoothness approximation* 3.19 in 3.32 stays valid in the Ξ^* region. Also the strong interaction of π and Ξ is lot less known than the Coulomb interaction.

For these reasons we are going to use for fitting only the Coulomb low-k^* part of the correlation function together with Gaussian description of the two-particle source. The procedure of using the Gaussian source in the CMS of the pair (pair rest frame - PRF) is a standard fitting procedure used in most of the femtoscopic measurement concerning non-identical particles [109, 197, 203, 149, 150]. For the purpose of fitting source is described by Gaussian shape of the two-particle relative emission function $S_{PS}(\boldsymbol{r^*}, \boldsymbol{k^*})$ in the PRF similarly as in 3.27. Because of the low statistics of the available data we assume that all three radii are equal $R_{out} = R_{side} = R_{long} = R$ and fit only one radius R and a parameter defining the shift in the *out* direction $\Delta r^*_{out} = \langle r^*_{out} \rangle$. The two-particle emission function them will be:

$$S_{PS}(\boldsymbol{r^*}, \boldsymbol{k^*}) \sim \exp\left[-\frac{(r^*_{out} - \Delta r^*_{out})^2}{2R^2} - \frac{r^{*2}_{side}}{2R^2} - \frac{r^{*2}_{long}}{2R^2} \right]. \tag{6.14}$$

Note that compared to 3.27 the parameter R is a Gaussian radius of the whole two-particle emission function ($R^2 = R^2_\pi + R^2_\Xi$).

The procedure of finding optimal parameters of the source model starts with a calculation of the theoretical correlation function in similar way as in the previous section. For a given set of parameters (R, Δr^*_{out}) of source model the correlation function is calculated using saved momenta of particle pairs and the relative emission coordinates $\mathbf{r}^*$ are generated according to the source model 6.14. Again for each pair the coordinates are generated multiple times and the calculation is averaged over the sample. This Monte Carlo calculation of the theoretical correlation function is time consuming and even with the averaging procedure we cannot completely avoid small random fluctuation of results. For this reason we cannot use the automatic optimization programs to do the fitting. Instead, finding the optimum parameters is done by creating a discrete χ^2 map in (R, Δr^*_{out}) parameter space. Since moving and

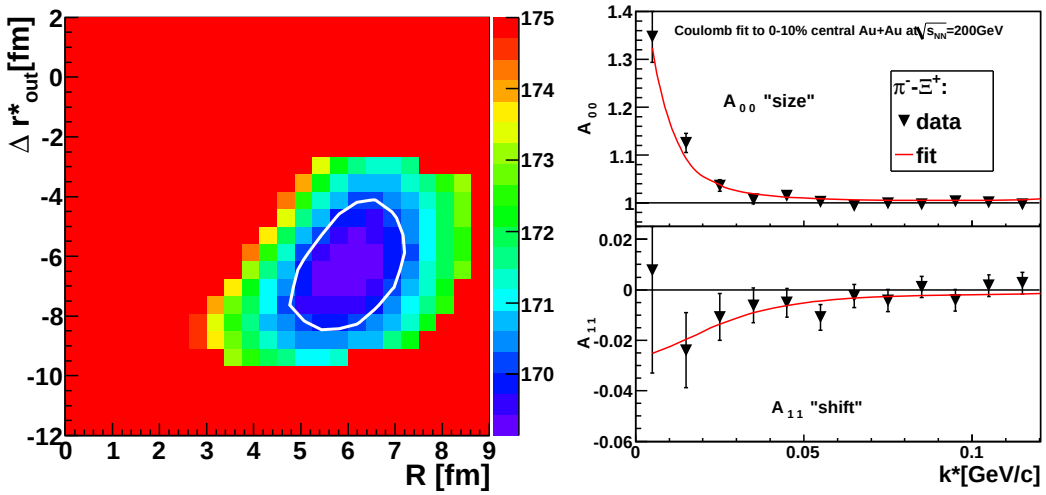

Figure 6.23: Results of the Coulomb fit to the π^-–Ξ^+ correlation function in the most central Au+Au collision at $\sqrt{s_{NN}}$=200 GeV. Left: the calculated χ^2 map with a 1-σ contour at $\chi^2_{min}+1$. Right: comparison of the measured data and the fitted function in the Coulomb region. The fit range of $k^* \leq 60$ MeV/c was used.

calculating the theoretical correlation function in the (R, Δr^*_{out}) space is time consuming the creation of the optimal χ^2 map is done on two passes. In the first pass only a coarse grained map is created in which the approximate position of the minimum is found. After that, map with finer binning is created in the vicinity of the minimum. The minimization system MINUIT [209] is then used to find minimum and extract proper errors from the fit in the map.

An example of a typical result from this fitting procedure is shown in Figure 6.23. Both the measured and calculated correlation functions are normalized to 1 in the region of $250 < k^* < 300$ MeV/c. To stay clear of any effects of the strong interaction in the Ξ^* peak the χ^2 is calculated only from the bins with $k^* \leq 60$ MeV/c. Which correlation function we are able to fit and the quality of the fit results depend on the available statistics. In our highest statistics bin, the most central 0-10% events, we are able to perform separate fits of each of the $\pi-\Xi$ charge combinations. The fit results are presented in Figure 6.24 in the form of 1-σ and 0.2-σ contours in the (R, Δr^*_{out}) plane corresponding to lines where the calculated χ^2 reaches minimum plus 1 and 0.2 respectively. The extracted values of R and Δr^*_{out} are summarized in Table 6.7 together with results from other fits. With a natural assumption that the size of the $\pi-\Xi$ source is the same for all charge combination we extract a combined result of $R = 4.7 \pm 0.5$ fm and $\Delta r^*_{out} = -5.9 \pm 0.9$ fm. We can try to apply similar procedure to the mid-peripheral bin of centrality $10-40\%$. The results in Figure 6.25 and Table 6.7 tell us that the fits to the individual correlation functions suffer

from excessive statistical errors because of the low available statistics. We can improve the results by fitting at the same time the combined like and unlike-sign correlation functions. For the mid-peripheral bin this procedure yields $R = 4.2 \pm 0.7$ fm and $\Delta r^*_{out} = -5.9 \pm 1.4$ fm. The much lower statistics in the most peripheral bin of $40 - 80\%$ allows to only use the combined data fit. The quality of the fit in Figure 6.26 is not very good, but still allows to constrain the values to $R = 0.6 \pm 1.5$ fm and $\Delta r^*_{out} = -2.8 \pm 1$ fm.

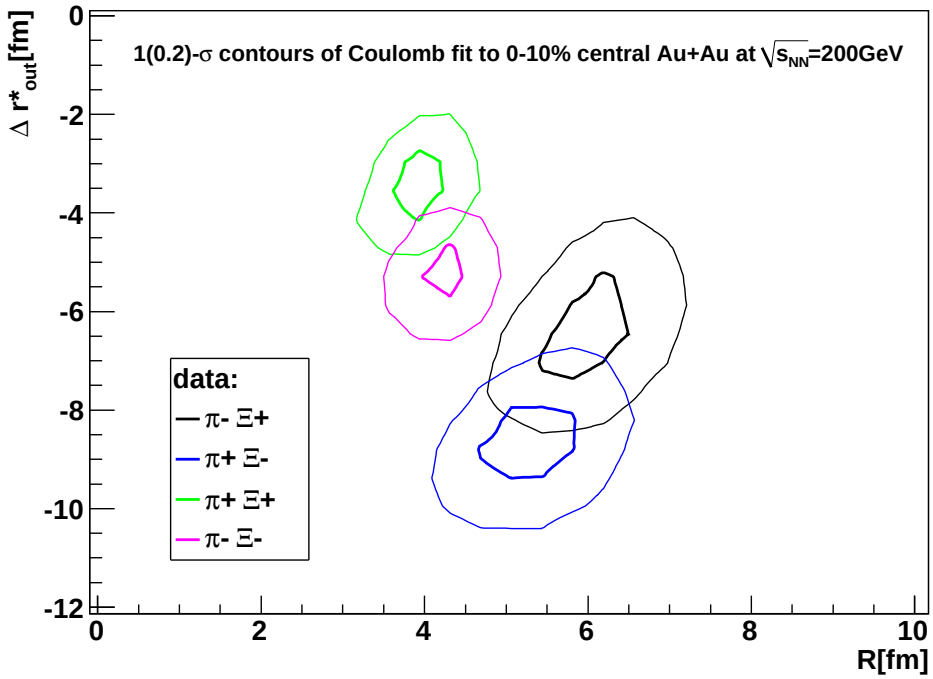

Figure 6.24: Results of the Coulomb fit in the most central 0-10% data for all $\pi-\Xi$ charge combinations. By a thin and thick line are drawn 1-σ and 0.2-σ contours of the χ^2 fit.

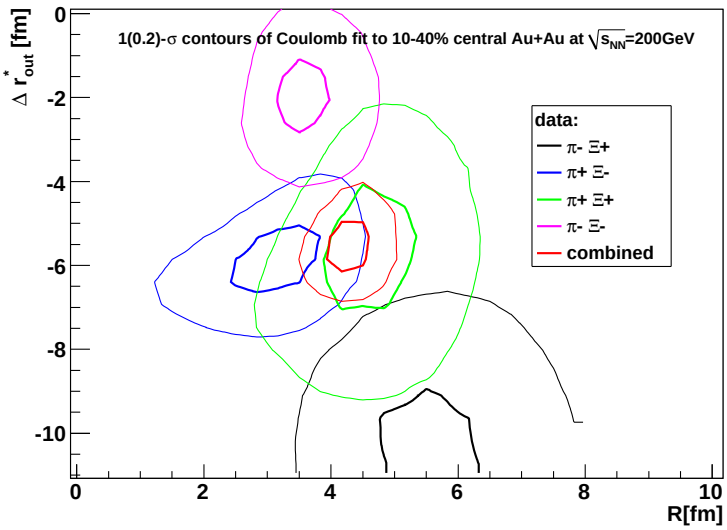

Figure 6.25: Results of the Coulomb fit in the mid-peripheral data (10-40%)for all $\pi-\Xi$ charge combinations. By a thin and thick line are drawn 1-σ and 0.2-σ contours of the χ^2 fit. In addition in red are results of a simultaneous fit to the combined like and unlike-sign correlation function.

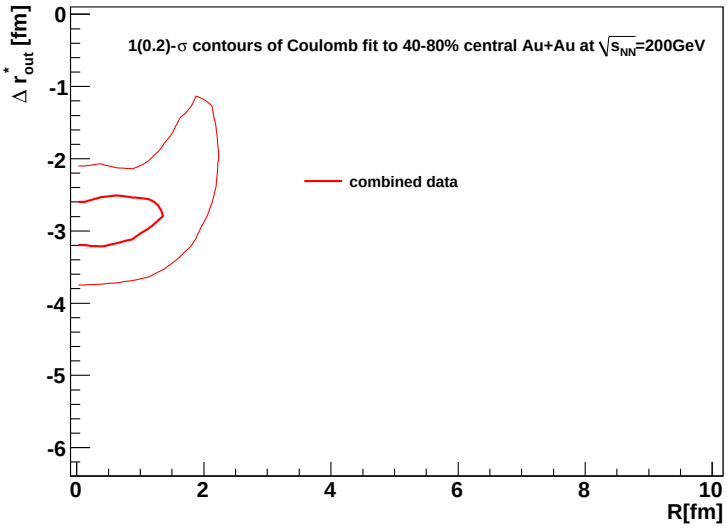

Figure 6.26: Results of the simultaneous Coulomb fit to the combined like and unlike-sign correlation function in the most-peripheral data (40-80%). The 1-σ and 0.2-σ contours of the χ^2 fit are shown by thin and thick line.

Before continuing further we should note a connecting between the obtained $\pi-\Xi$ results and the previous $\pi-\pi$ measurement. The $\pi-\pi$ measurements in Figure 6.6 give the size of the source in the most central collision $R = (6-7)$ fm (depending on p_T). Comparing this with the $\pi-\Xi$ results of $R = 4.7 \pm 0.5$ fm and $\Delta r^*_{out}= -5.9 \pm 0.9$ fm already tells as an important information. Since the R in $\pi-\Xi$ is a convolution of the sizes of the source of pions and Ξs, the $\pi-\Xi$ source being similar in size to the source of pions means that the size of the Ξ source is small. This together with negative and large shift on the order of the size of the whole source suggest that the source (meaning homogeneity region) of the Ξ is significantly smaller than that of pions and shifted to the edge of the system. This observation is in good qualitative agreement with what is predicted by models that include significant collective flow of multi-strange baryons.

One of the most challenging parts of this analysis is the handling of purity corrections. Before any final conclusion can be drawn we must study and understand the effects of the purity correction on the final results. Here we will try to access the systematic errors connected to the performed purity corrections. In the Section 3.2.1 was discussed the λ parameter that is used to regulate the strength of the correlation function when fitting $\pi-\pi$ correlation function. We have used this parameter as a measure of purity of used π. In the Section 6.3 the $\pi-\Xi$ correlation function was already corrected for the effects of π and Ξ purities individually in each $\vec{k}^*$ bin. No further adjustments of the strength of the correlation function should then be necessary during the fit. Because both the R parameter of the fit and the purity correction affect the overall strength of the correlation function the R parameter will be affected by any inaccuracy in the purity correction procedure. We can test the quality of the correlation function and estimate systematic errors due to purity corrections by introduction of the λ parameter in the fit in a similar way as it is done $\pi-\pi$ HBT. In the case of perfectly purity corrected correlation function λ should be 1. In this way of fitting the obtained λ will not be a measure of non-purities as in 3.40, but rather a $\vec{k}^*$ -independent multiplicator of the corrections in Section 6.3. For this reason the λ may be, unlike in $\pi-\pi$ fits, greater then 1. Any inaccuracy in purity correction should hence lead to a deviation from unity. The convergence of the fit in the vicinity of $\lambda = 1$ can be taken as an indicator of the quality of the used purity-corrected correlation function.

After the introduction of λ parameter we obtain 3D χ^2 maps from the fits. A two dimensional slices from such a map for a $\pi^- - \Xi^+$ correlation function in the most central data are shown in the Figure 6.27. One can see that in the $R-\Delta r^*_{out}$ plane the map is quite similar to the one in Figure 6.23. In the $R-\lambda$ the map shows indeed strong relation between the two extracted parameters. To better see the effects of the fitting we present in Figure 6.28 the results of the fits for all correlation functions in the most central bin. The actually extracted values of the fits are included in the Table 6.7 together with previous results for comparison. These results show that when the λ is allowed to vary it converges

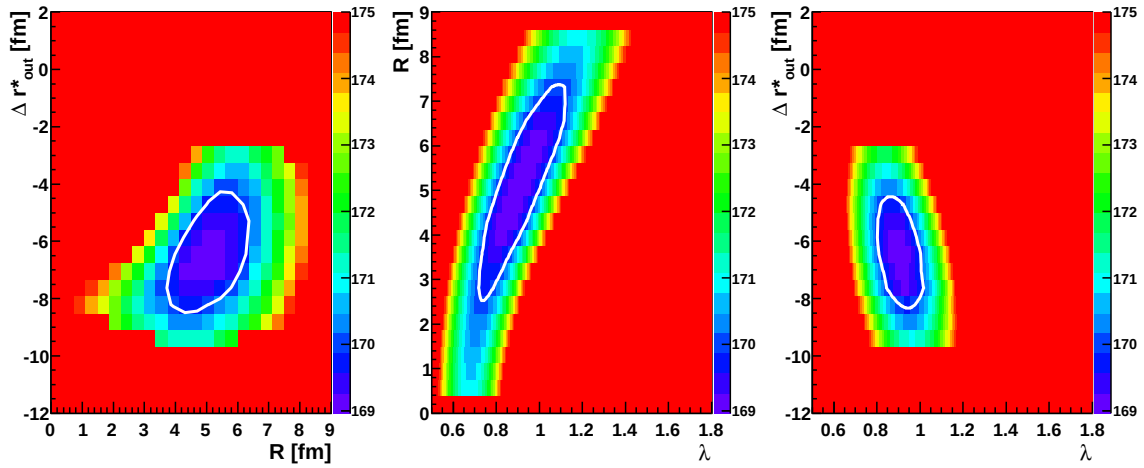

Figure 6.27: Slices from calculated χ^2 map of Coulomb fit to the $\pi^-\!-\!\Xi^+$ in the most central Au+Au collisions at $\sqrt{s_{NN}}$=200 GeV. The χ^2 mas is calculated in three dimensions: R, Δr^*_{out}, and λ. The 2-dimensional slices of the map are shown at the fits optimal value of the remaining variable. The line depicts 1-σ contour around minimum.

to values in range of $0.9 \lesssim \lambda \lesssim 1.15$. We can take that as an estimate of the precision of the performed purity corrections. When we combine the measurements of R and Δr^*_{out} from all the charge combinations we arrive at values of $R = 5.4 \pm 0.5$ fm and Δr^*_{out}= -5.9 ± 0.9 fm. From these results we see that the introduction of λ as an additional parameter brought change to the extracted Gaussian radii on the order of $10 - 20\%$.

We can attempt to use similar method for the mid-peripheral data set. The results are shown in Figure 6.29. This figure is merely shown to demonstrate that we also see the relation between R and λ, but the available statistics is too low to constrain the fits well after the introduction of one more fit parameter. For the mid-peripheral and peripheral dataset it is hence better to use the previous fit results with only R, and Δr^*_{out} fitted (Figure 6.25 and 6.26) and use the estimate of the systematic error obtained from central data. Final results of the fitting procedure for combined datasets with quoted systematic errors are summarized in Table 6.8.

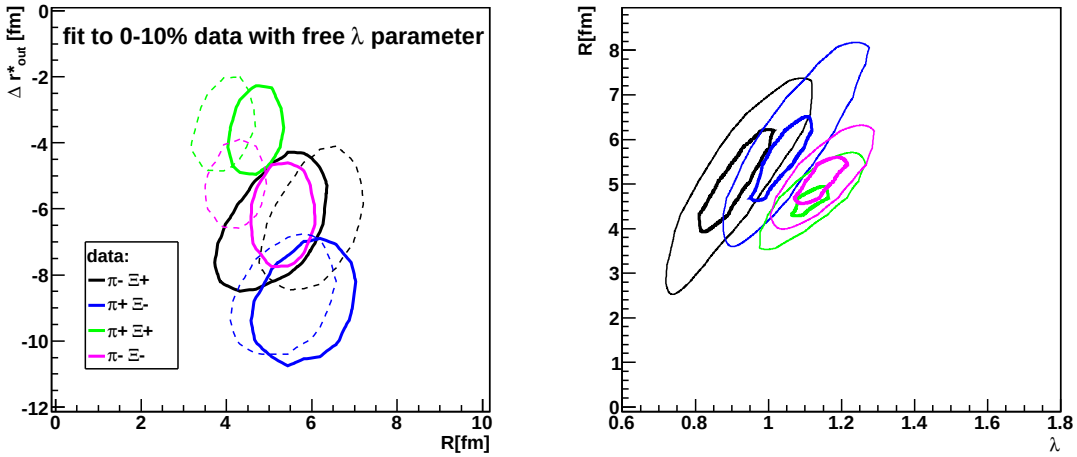

Figure 6.28: Results of the Coulomb fit in three dimensions (R, Δr^*_{out}, λ) to the most central 0-10% data. Left:1-σ contours in the (R-Δr^*_{out}) plane while λ is held at the fits optimal value. By a dashed line are for comparison included 1-σ results from the previous 2-dimensional fit in Figure 6.24. Right: 1(thin line) and 0.2-σ(thick line) contours of the fit in ($\lambda - R$) plane at optimal Δr^*_{out} value.

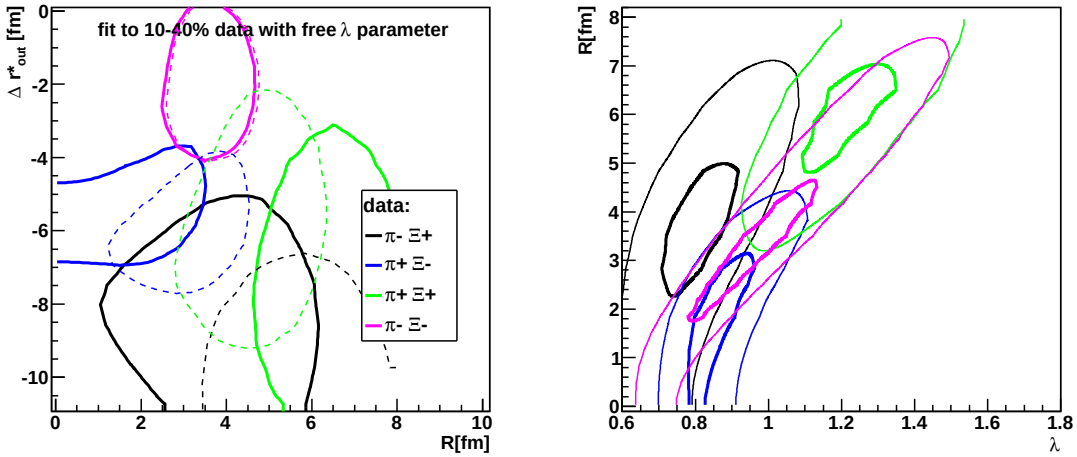

Figure 6.29: Results of the Coulomb fit in three dimensions (R, Δr^*_{out}, λ) to the mid-peripheral (10-40%) data. The depiction of results is similar to Figure 6.28.

data:	2D fit R[fm]	2D fit Δr^*_{out}[fm]	2D fit χ^2/NDF	3D fit with λ λ	3D fit with λ R[fm]	3D fit with λ Δr^*_{out}[fm]	3D fit with λ χ^2/NDF
0-10% centrality							
$\pi^- - \Xi^+$	6.2±1.1	-6.5±2.0	169.14/150	0.91±0.11	5.1±1.3	-6.5±2.0	168.97/150
$\pi^+ - \Xi^-$	5.4±0.8	-8.8±1.4	157.41/150	1.05±0.11	5.8±1.3	-8.8±1.4	157.32/150
$\pi^+ - \Xi^+$	3.9±0.7	-3.5±1.8	153.77/150	1.13±0.10	4.7±0.8	-4.1±1.8	153.38/150
$\pi^- - \Xi^-$	4.3±0.7	-5.3±1.9	172.21/150	1.14±0.09	5.1±0.8	-5.9±1.9	171.32/150
combined	4.7±0.5	-5.9±0.9			5.4±0.5	-5.9±0.9	
10-40% centrality							
$\pi^- - \Xi^+$	5.5±2.0	-10.2±3.6	146.19/150				
$\pi^+ - \Xi^-$	3.2±1.7	-5.9±1.8	156.14/150				
$\pi^+ - \Xi^+$	4.5±1.7	-5.9±3.4	150.23/150				
$\pi^- - \Xi^-$	3.5±1.0	-2.1±2.1	158.36/150				
combined	4.2±0.7	-5.9±1.4	616.66/600				
40-80% centrality							
combined	0.6±1.5	-2.8±1.0	677.05/600				

Table 6.7: Result of the fit to the Coulomb part of the $\pi-\Xi$ correlation function from Au+Au collisions at $\sqrt{s_{NN}}$=200 GeV. All presented errors are statistical errors of the fit.

centrality	R[fm]	Δr^*_{out}[fm]
$0-10\%$	5.4±0.5±0.8	-5.9±0.9
$10-40\%$	4.2±0.7±0.8	-5.9±1.4
$40-80\%$	0.6±1.5±0.8	-2.8±1.0

Table 6.8: Final results of the measured Gaussian femtoscopic radii and relative emission asymmetries in the CMS of the pair for the $\pi-\Xi$ system in Au+Au collisions at $\sqrt{s_{NN}}$=200 GeV. Systematic errors for Δr^*_{out} were found to be negligible.

6.6 Comparison to HYDJET++ model

In the previous sections we have shown that we observe a correlation signal in two regions caused by Coulomb and strong interaction, but we are not able to explain them both at the same time using a simple emission models such as Gaussian or blast wave parametrization. We also understand that the measured sizes and shifts of the homogeneity regions are strongly influenced by transverse expansion of the system. Moreover the observed correlation function is also influenced by decays of resonances that may significantly change (prolong) the emission function. In our case the contribution and influence of resonances on the correlation function is of interest as the $\Xi^{*0}(1530)$ is a long lived resonance from which originates significant part of the observed Ξs.

In this section is studied influence of the collective flow and Ξ^* resonance on the size of the homogeneity length and shift between average freeze-out space time points of Ξ and π. For this we employ hydrodynamics-parametrized statistical hadronization model HYDJET++ which was already described in Section 3.3.2. Similarly as in previous sections we are interested in comparison of different scenarios of emission of multi-strange baryons. For the comparison with simulation we use the data from the most central Au+Au collision. In the HYDJET++ simulation we implement three scenarios: *thermal freeze-out* in which the particle emission occurs much later after the chemical freeze-out $T_{ch} < T_{th}$; *chemical freeze-out* in which the particle emission coincides with, or is shortly after, the chemical freeze-out $T_{th} = T_{ch}$. In addition to these we are able to introduce into HYDJET++ *early freeze-out* a combined scenario (used later in Section 6.6.3) when Ξ and $\Xi^*(1530)$ are emitted already at chemical freeze-out while other particles π, K, p are emitted later at the thermal freeze-out.

	chemical($T_{th} = T_{ch}$)	thermal($T_{th} < T_{ch}$)	STAR BW fit
T_{ch} (MeV)	165	165	165
T_{th} (MeV)	165	100	97
μB (MeV)	28	28	28
μS (MeV)	7	7	7
μQ (MeV)	-1	-1	-1
γ_S	1	1	1
τ (fm/c)	7.0	8.0	8.9
$\Delta\tau$ (fm/c)	2.0	2.0	3.16
R (fm)	9.0	10.0	13.0
η_{max}	2	2	2
ρ_{max}	0.65	1.1	1.03

Table 6.9: Parameters of the HYDJET++ model for simulation of particle emission at thermal and chemical freeze-out. The STAR BW denotes implementation of blast wave parameters from $\pi-\pi$ HBT into HYDJET++ model.

The parameters of HYDJET++ for the *chemical* and *thermal* freeze-out are summarized in Table 6.9. The parameters for these two scenarios were estimated to reasonably reproduce particle spectra and ratios as it will be described in more details in the next section. In addition, one more set of parameters is used which corresponds to values obtained from blast wave fits to STAR data in [111]. For these scenarios we first analyze particle ratios and m_T-spectra to see which parametrization describes best the particle production. After that we study the space-time differences of the Ξ and π emission points including the influence of the relative contribution of Ξ from $\Xi^*(1530)$ resonance decay on the $\pi-\Xi$ emission asymmetries.

6.6.1 Ratios of hadron abundances and m_T-spectra

The particle abundances in heavy ion collisions in a wide energy range can be reasonably described by statistical hadronization models based on the assumption that the produced hadronic matter reaches thermal and chemical equilibrium. The HYDJET++ model has already been successfully applied [124] to describe RHIC data on various particle ratios produced in central Au+Au collisions near mid-rapidity at $\sqrt{s_{NN}}$=200 GeVwith parameters similar to those used in this work: $\widetilde{\mu_B} = 0.0285$ GeV, $\widetilde{\mu_S} = 0.007$ GeV, $\widetilde{\mu_Q} = -0.001$ GeV, the strangeness suppression factor $\gamma_s = 0.8$ and the chemical freeze-out temperature $T_{ch} = 0.165$. However first STAR preliminary measurements [210] of the $\Xi^*(1530)$ spectra and their yields, Figure 6.30, have shown substantially higher $\Xi^*(1530)/\Xi^-$ ratio when compared to statistical model calculations.

Before utilizing the model for analysis of femtoscopic observables it is necessary to check an agreement in description of basic particle production. In Figure 6.31 the m_T-spectra of π^+ and $\Xi^{\pm}$ for the three different parameter sets are compared with STAR data [67, 75]. One can see that π, K, p spectra are better described within the *thermal freeze-out* scenario while the Ξ spectrum is better described within the *chemical freeze-out* scenario. The HYDJET++ used with blast wave parameters from [111] overpredicts the absolute yields, because of the larger volume of the system ($R = 13$ fm). The slope of the p_T-spectra of $\Xi^*(1530)$ [210] is also much better described within the *chemical freeze-out* scenario, but the model underestimates the Ξ^* /Ξ ratio (>2 times), similarly as do other statistical models (see Figure 6.30, and [210]).

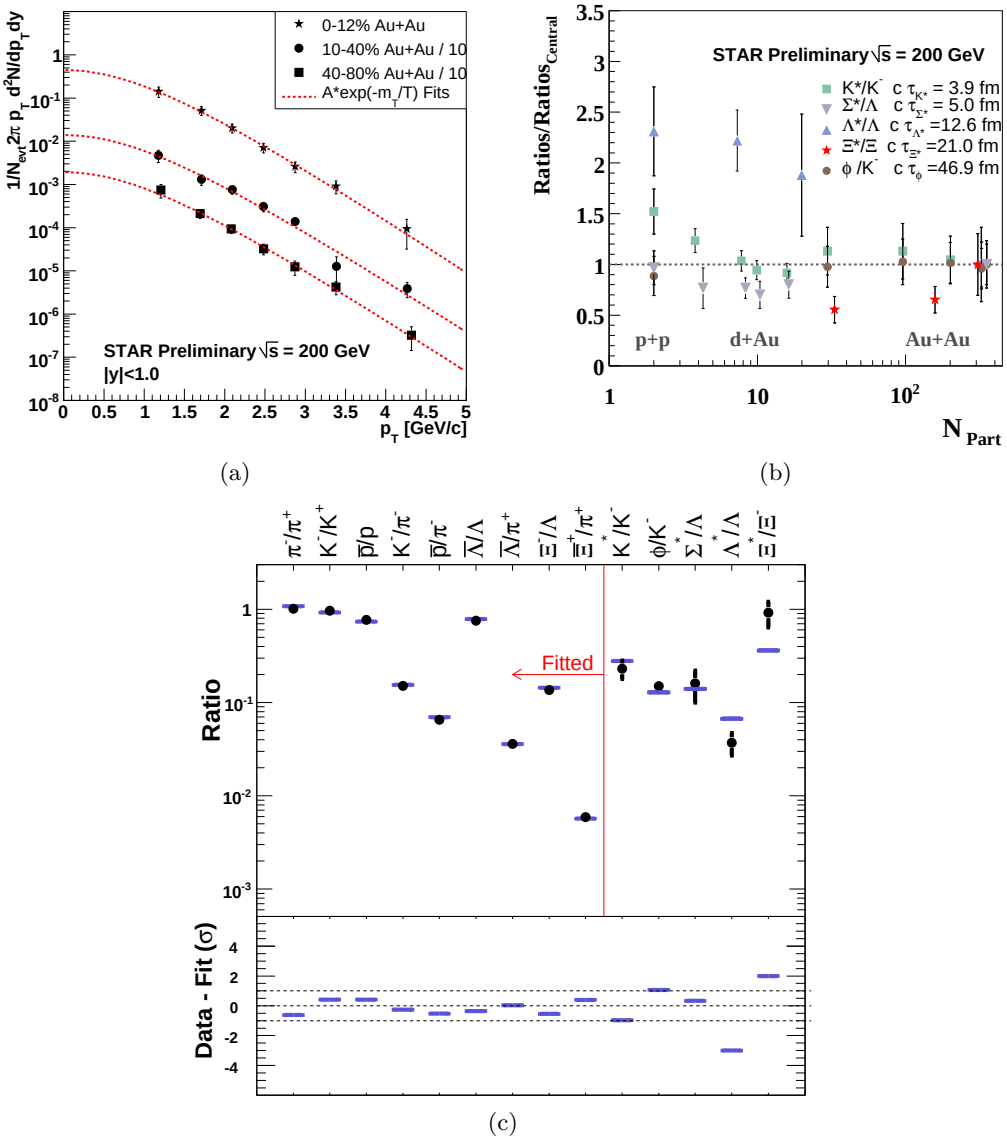

(a) (b)

(c)

Figure 6.30: STAR preliminary results from [210] on $\Xi^0(1530)$ spectra and yields from from Au+Au collisions at $\sqrt{s_{NN}}$=200 GeV. (a) corrected Ξ^* spectra and (b) Ξ^*/Ξ ratios at three different centralities. (c) Comparison with thermal fit(blue) to the STAR data(black).

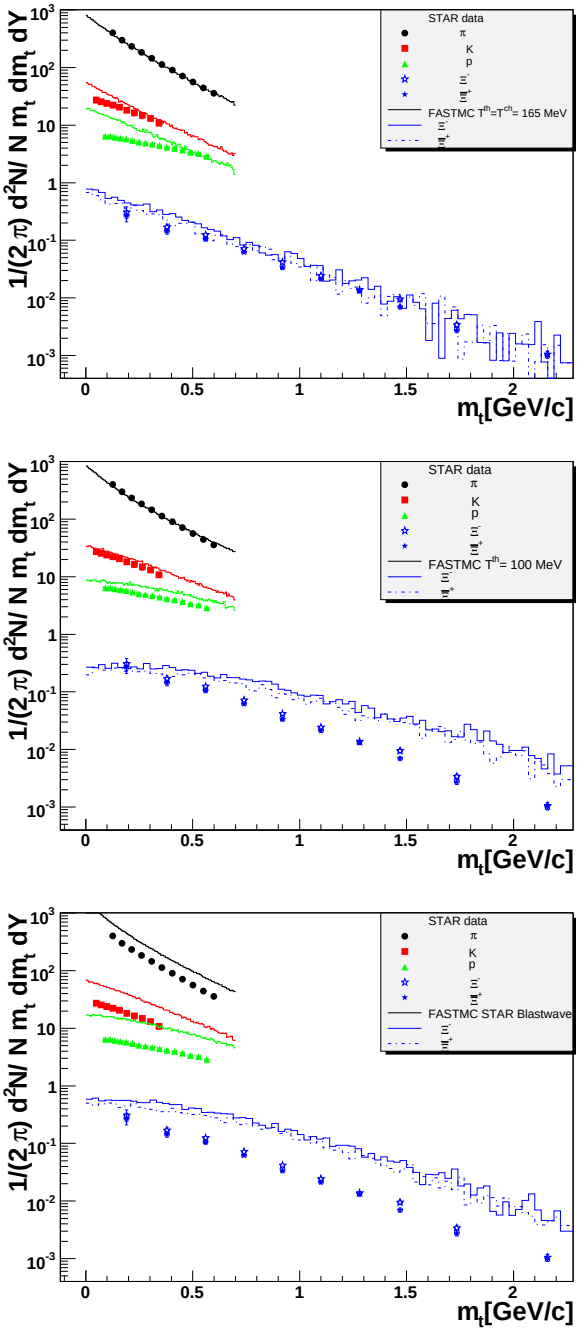

Figure 6.31: The m_T-spectra of π^+, K^+, p and $\Xi^{\pm}$ calculated with HYDJET++(FASTMC) within from the top: chemical($T_{th} = T_{ch}$), thermal($T_{th} < T_{ch}$) freeze-out scenario and blast wave fit parameters. The experimental data of STAR collaboration are shown by the solid points, the HYDJET++ calculations by the lines.

6.6.2 $\pi-\pi$ femtoscopic radii

If the HYDJET++ model is to describe the $\pi-\Xi$ correlation it first needs to be checked that it describes well the source of pions. This can be done easily using the available high precision $\pi-\pi$ data. We can test the imprint of the scenarios under study on the predicted homogeneity lengths.

With this motivation in mind we can extract from the simulation $\pi-\pi$ HBT radii for both cases. The procedure for extraction of the femtoscopic radii from simulation is simple in the case of identical non-interacting pions. The correlation function is calculated from pairs of pions via 3.20. Only pions from similar kinematic region (η, p_T) as in the real data are used. In the case of $\pi-\pi$ and under the assumption of Gaussian source, the correlation function can be expressed explicitly by 3.41. The radii and λ parameter are then obtained simply by fitting the correlation function by 3.41.

The predictions from HYDJET++ for $\pi-\pi$ HBT are presented in Figure 6.32 for the two different scenarios of freeze-out as well as for the HYDJET++ with blast wave parameters. The best description of the data seems to within the *thermal freeze-out* scenario, while the HYDJET++ with blast wave parameters clearly over predicts the measured radii. Most notably good agreement of the λ parameter with the data is reached when the pions from weak decays are included.

6.6.3 Space-time differences of the Ξ and π emission points

The results in Figure 6.31 and 6.32 rule out the possibility to use the same parameters for the HYDJET++ simulation as those obtained from blast wave fit. The simulations also indicate that the m_T-spectra of different particle species and the femtoscopic radii can't be described with the same set of parameters. To solve this problem we need to use the third *early freeze-out* scenario: Ξ, $\Xi^*(1530)$ are emitted at the chemical freeze-out, while the other particles are emitted later at the thermal freeze-out. In this section we will study the separation between particles emission points in the *out* direction in CMS of the pair and compare between the different scenarios.

As it was already pointed out in Section 3.1.1, equation 3.38, for symmetrical system $\langle r^* \rangle_{side} = \langle r^* \rangle_{long} = 0$ and the only observable shift is $\Delta r^*_{out} = \langle r^* \rangle_{out} = \gamma_\perp(\Delta\bar{x}_{out} - V_\perp \Delta\bar{t})$. The space part of the shift may be influenced by the collective expansion of the system, while the time component can change by different decoupling conditions between the particle species.

The preliminary results of measurements of Δr^*_{out}done by the STAR experiment for pairs of $\pi-K$,$\pi-p$, and $K-p$ in Au+Au collisions at $\sqrt{s_{NN}}$=200 GeV and $\sqrt{s_{NN}}$=62 GeV are available in [211]. These results are compared in Figure 6.33 with results from the HYDJET++ simulation. Except for the $K-p$ the simulation is in agreement with the

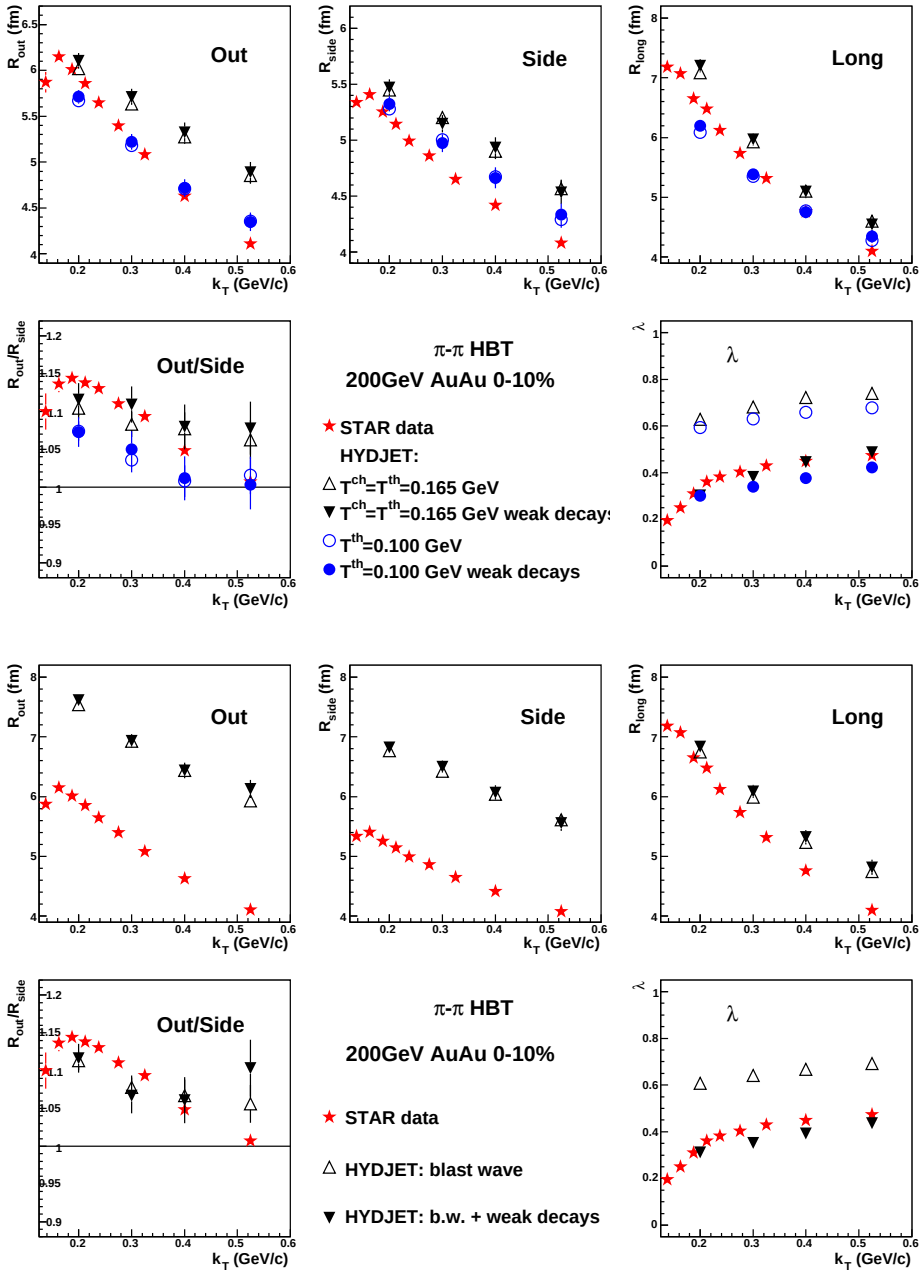

Figure 6.32: Comparison of HYDJET++ calculations of $\pi-\pi$ HBT radii with real data for (top) *chemical and thermal* scenario of freeze-out and (bottom) for calculation with the same parameters that describe pion source in the blast wave model. In all calculation a variant with and without inclusion of pions originating from weak decays is presented.

measured data. The statistical errors of the real data are too large to conclusively decide between the two shown scenarios, but here is slightly better agreement with the *thermal freeze-out* scenario which is also favored by the comparison of particles spectra.

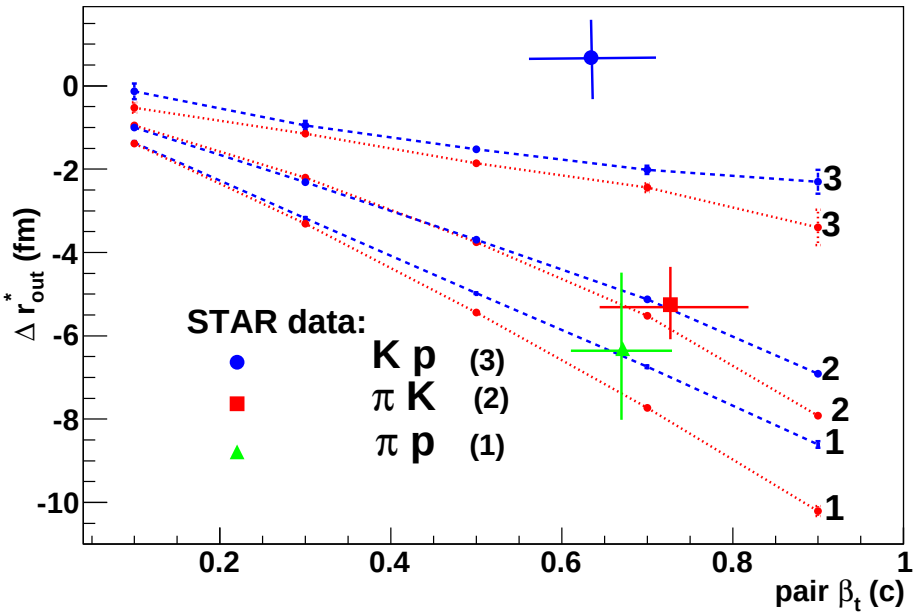

Figure 6.33: The total space-time shift in pair rest frame for $\pi p, \pi K, \pi p$ for *thermal freeze-out* (blue dashed line) and *chemical freeze-out* (red dotted line) scenarios in comparison with STAR collaboration data for Kp (circles), πK (squares), and πp (triangles). The HYDJET++ calculations are shown by numbers: $(1)\pi p$, $(2)\pi K$, $(3)Kp$.

The separations Δr^*_{out} between the emission points of π and Ξ in the pair's CMS are displayed in Fig. 6.34. The values of the shifts were obtained from the simulation using $\pi - \Xi$ pairs from particles that underwent the same cuts as in real data. Moreover since we are comparing the extracted shift to the shift obtained from the Coulomb (low k^*) part of the correlation function only pairs with $k^* < 40$ MeV/c were allowed. For the three different scenarios are also shown both the time and space components of the total shift. The biggest difference between the three cases that influences the total shifts comes from the spacial part of the shift. The spacial shift is negative in all three cases. This corresponds to Ξ being emitted more on the outside of the whole source, as it is expected if source undergoes collective transverse expansion in which the Ξ participates. Due to larger value of the maximal flow velocity and larger system size the Ξs are emitted closer to the surface for the *thermal freeze-out* than for the *chemical freeze-out* and *early freeze-out*. Since the pions are light, their average emission position in the *out* direction is affected by the temperature of the system. The homogeneity region of pions of given momentum shrinks and moves to edge with decreasing temperature of the system and increasing transverse momentum of the particles. The pion smearing is maximal for the *chemical freeze-out*, so its shift is smallest. The smallest value of the overall shift between π and Ξ hence occurs for the *early freeze-out* scenario because the pion shift is maximal (coincides with *thermal freeze-out* and Ξ shift is

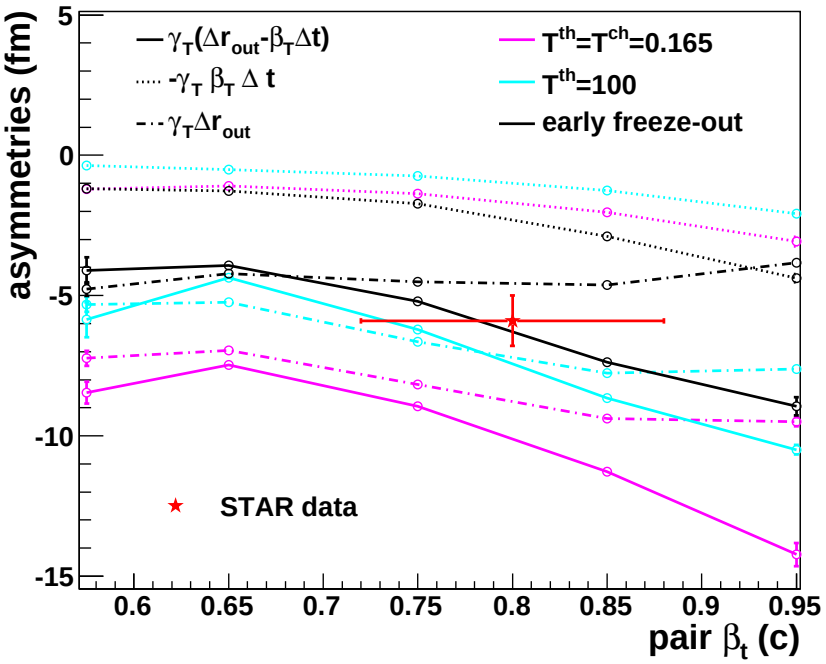

Figure 6.34: The space $\gamma_T\Delta r_{out}$ (dashed-dotted lines) and time $-\gamma_T\beta_T\Delta t$ (dotted lines) relative contributions in the separations Δr^*_{out} (solid lines) between the emission points of π and Ξ for the three different scenarios. In red is shown the measured shift from the real data. The horizontal error bar of the real data is estimated from the p_T distribution of pairs used in analyses.

minimal (coincides with *chemical freeze-out* scenario). Although the best description of the data is obtained within the *early freeze-out* scenario, the statistical error of the measured data is too large to conclusively decide.

As previously stated the STAR experiment observes anomalously high Ξ^* /Ξ ratio in the central collisions [210] when compared to the predictions of statistical model. Since the HYDJET++ model contains the production and decay of Ξ^* we can test the influence Ξ^* /Ξ on the predicted emission asymmetry between pions and Ξs.

For the case of *early freeze-out* the space and time relative contributions to the total space-time shift between the emission points of π and Ξ in the pair's CMS are shown in Figure 6.35 for direct Ξ and Ξ from $\Xi^*(1530)$ decays. The figure demonstrates that while $\Xi^*(1530)$ decay increases the time and space shifts between π and Ξ the overall shift is not so strongly affected. The resulting total shift is larger for the direct Ξs then for Ξs coming only from Ξ^* decays. The shift obtained by HYDJET++ with ratio $\Xi^*/\Xi \sim 0.25$ considered above is then closer to the direct Ξ. Hence a large deviation of the Ξ^*/Ξ ratio from 0.25 can lead to an ambiguous interpretation of Figure 6.34 as both increase of Ξ^*/Ξ ratio and *early freeze-out* decrease Δr^*_{out}. To fully disentangle the effects of Ξ^*/Ξ and different freeze-outs more precise measurements are needed.

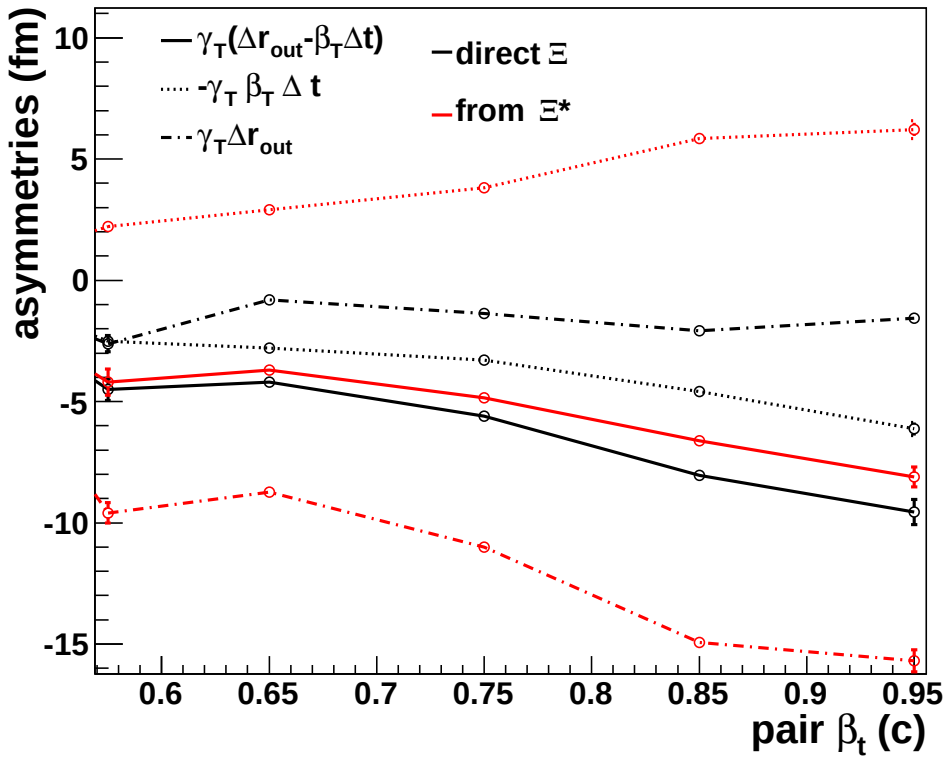

Figure 6.35: The space $\gamma_t \Delta r_{out}$ (dashed-dotted lines) and time $-\gamma_t\beta_t\Delta t$ (dotted lines) relative contributions in the separations Δr^*_{out} (solid lines) between the emission points of π and Ξ in pair's CMS for direct Ξ and Ξ from $\Xi^*(1530)$ decays within *early freeze-out* scenario.

One thing should also be noted and that is that the HYDJET++ is not a transport model and hence does not contain rescattering in the hadron phase which could possibly also alter the shifts extracted from the simulations.

Summary

The presented results on the $\pi-\Xi$ correlations together with $\Xi^*(1530)$ spectra [210] provide an interesting information about the space-time interval between chemical and thermal freeze-outs. Combined comparison of the m_T-spectra and space-time differences between HYDJET++ and real data was performed. The best agreement with the data was achieved within the *early freeze-out* scenario. However the available statistics is too low to make an unambiguous interpretation of the results. More precise measurement of the π–Ξ correlation function as well as Ξ^*/Ξ ratio is thus necessary.

Chapter 7

Conclusions and Outlook

The main goal of this thesis was to study space-time properties of emission of multi-strange baryons with a motivation of observing phenomena connected with a collective behavior of the system created in the collisions of heavy ions. The goal of the thesis was met with following results.

We have employed the apparatus of particle femtoscopy to measure $\pi - \Xi$ correlation functions at two different Au+Au collision energies. This is a first ever femtoscopic measurement that includes multi-strange baryons. In the extracted correlation effects of Coulomb and strong interactions were observed with the latter going via $\Xi^*(1530)$ resonance. Although the $\Xi^*(1530)$ is a well established resonance this measurement is its first observation in the environment of high particle multiplicity of the heavy-ion collisions. The measured correlation function have shown significant centrality dependence, and weak dependence on the collision energy.

In this thesis a novel technique of decomposition of the correlation functions into spherical harmonics was used. With this tool we have been able to access information about the average relative emission asymmetry between pions and Ξ contained in the angular part of the correlation function. The data reveal that on average the Ξ, when compared to pion, is emitted in the transverse direction more at the outer edge of the system. This qualitative observation is in accord with what is expected for a system in which the multi-strange baryons take part in the collective expansion.

Comparison of the measured results with calculated prediction of the two most commonly used models of particle emission (Gaussian source, and blast wave) have shown that we are not able to satisfactorily describe at the same time the correlation originating from Coulomb and from the strong interaction. This problem has been lately under intense theoretical study, because the correlation comes from the strong interaction going through resonance, description of which is not fully known. Also correlations via Ξ^* is at higher values of k^* where the existing theoretical framework is pushed to its limits. The clarification of this

issue could in future bring vital information about the dynamics of the system and particle emission.

To quantify our results further, we have taken the highest statistics dataset ($\sqrt{s_{NN}}$=200 GeV collision energy) and fitted the data in the region of the Coulomb interaction only. The data were fitted with Gaussian model of the emission function in the center of mass of the pair. We have extracted, in each centrality bin, values of the total size of source (homogeneity region) and the value of the average relative shifts in emission between the two particle species.

From the obtained values we can draw the following conclusions. We observe decrease of the sizes and the shifts from central to peripheral collisions. Concentrating on the highest statistics most central data, the measured size of the two-particle π–Ξ source is close to what is measured for single-particle pion source. This means that the source (homogeneity region) of Ξ is significantly smaller than that of pions. This together with the large magnitude of the shift, on the order of the size of the homogeneity region, supports models that include significant transverse flow of multi-strange baryons. In such models the strong flow-induced correlation between particle momenta and emission coordinates causes the Ξ source to be small and significantly shifted toward the edge of the system. The measured results on the π–Ξ correlations are hence an independent confirmation of the flow of multi-strange baryons in heavy-ion collisions.

Since the relative emission asymmetries can be influenced not only by transverse flow, but also by different decoupling conditions of different particle species, we have studied the influence of the different decoupling scenarios of multi-strange baryons. For this we have employed hydrodynamics-parametrized HYDJET++ model which includes production of particles and resonances at chemical equilibrium. Using this model we have studied influence of the collective flow and Ξ^* resonance on the shift between average freeze-out space time points of Ξ and π. The obtained results on $\pi-\Xi$ correlations, together with information on $\Xi^*(1530)$ and other particle spectra, seem to favor the so called *early freeze-out* scenario, in which Ξ and $\Xi^*(1530)$ are emitted earlier then other particle species - already at chemical freeze-out while other particles π, K, p are emitted later at the thermal freeze-out. However the available statistics is too low to make a conclusive unambiguous interpretation of the results. More precise measurement of the $\pi-\Xi$ correlation function as well as Ξ^*/Ξ ratio is thus necessary.

It is then a good news for this analysis that the STAR experiment has already collected huge sample of Au+Au collision data at $\sqrt{s_{NN}}$=200 GeV during its latest 2010 run. The STAR has now an order of magnitude larger available dataset: $\sim 300 \cdot 10^6$ minimum bias and the same amount of centrally triggered data. This advance was possible due to upgrades of the STAR data acquisition system and the data are expected to be available for physics within a year. This together with enhanced particle identification by a new time-of-flight

detector will drastically increase available pair statistics. We expect that it will be possible to carry out the analyses in narrower centrality bins and perform study of the p_T dependence of the radii. This should bring more information about the dynamics of the system. Such a large statistics should also allow measurements in a system similar to $\pi-\Xi$ and that is the $\pi-\Omega$. These measurements will shed more light on the physics of multi-strange baryons in ultra-relativistic heavy ion collisions.

Bibliography

[1] E. Rutherford. The scattering of α and β particles by matter and the structure of the atom. *Phil. Mag.*, 21:669–688, 1911.

[2] C. D. Anderson. THE POSITIVE ELECTRON. *Phys. Rev.*, 43:491–494, 1933.

[3] J. Chadwick. POSSIBLE EXISTENCE OF A NEUTRON. *Nature*, 129:312, 1932.

[4] B. Cassen and E. U. Condon. On nuclear forces. *Phys. Rev.*, 50:846–849, 1936.

[5] Murray Gell-Mann. Symmetries of baryons and mesons. *Phys. Rev.*, 125:1067–1084, 1962.

[6] Murray Gell-Mann. The Eightfold Way: A Theory of strong interaction symmetry. CTSL-20.

[7] G. Zweig. An SU(3) model for strong interaction symmetry and its breaking. CERN-TH-401.

[8] Murray Gell-Mann. A Schematic Model of Baryons and Mesons. *Phys. Lett.*, 8:214–215, 1964.

[9] Hermann Weyl. *Ann. Physik*, 59:101, 1919.

[10] Mills R. Yang C. N. Conservation of isotopic spin and isotopic gauge invariance. *Phys. Rev.*, 96:191, 1954.

[11] Steven Weinberg. A Model of Leptons. *Phys. Rev. Lett.*, 19:1264–1266, 1967.

[12] Yuval Ne'eman. Derivation of strong interactions from a gauge invariance. *Nucl. Phys.*, 26:222–229, 1961.

[13] Amsler NC. et al. (Particle Data Group). *Physics Letters*, B667:1, 2008.

[14] Siegfried Bethke. Experimental Tests of Asymptotic Freedom. *Prog. Part. Nucl. Phys.*, 58:351–386, 2007.

[15] B. Z. Kopeliovich and A. H. Rezaeian. Applied QCD. 2008.

[16] D. J. Gross and Frank Wilczek. ULTRAVIOLET BEHAVIOR OF NON-ABELIAN GAUGE THEORIES. *Phys. Rev. Lett.*, 30:1343–1346, 1973.

[17] Claude W. Bernard et al. The static quark potential in three flavor QCD. *Phys. Rev.*, D62:034503, 2000.

[18] *Quark-Gluon plasma : from big bang to little bang.* Cambridge University Press, 2005.

[19] Cheuk-Yin Wong. *Introduction to High-Energy Heavy-Ion Collisions.* World Scientific Pub Co Inc, 1994.

[20] *Finite-temperature field theory : principles and applications.* Cambridge University Press, 2006.

[21] *Finite Temperature Field Theory.* World Scientific Publishing Co. Pte. Ltd., 1997.

[22] F. Karsch, E. Laermann, and A. Peikert. Quark mass and flavor dependence of the QCD phase transition. *Nucl. Phys.*, B605:579–599, 2001.

[23] J. Cleymans, R. V. Gavai, and E. Suhonen. Quarks and Gluons at High Temperatures and Densities. *Phys. Rept.*, 130:217, 1986.

[24] A. Chodos, R. L. Jaffe, K. Johnson, Charles B. Thorn, and V. F. Weisskopf. A new extended model of hadrons. *Phys. Rev.*, D9:3471–3495, 1974.

[25] Walter Greiner. *Quantum Chromodynamics.* Springer, Berlin, 2007.

[26] Jean Letessier and Johann Rafelski. *Hadrons and Quark-Gluon Plasma (Cambridge Monographs on Particle Physics, Nuclear Physics and Cosmology).* Cambridge University Press, 2005.

[27] C. R. Allton et al. QCD at non-zero temperature and density from the lattice. *Nucl. Phys. Proc. Suppl.*, 141:186–190, 2005.

[28] Ulrike Kraemmer and Anton Rebhan. Advances in perturbative thermal field theory. *Rept. Prog. Phys.*, 67:351, 2004.

[29] G. Boyd et al. Thermodynamics of su(3) lattice gauge theory. *Nucl. Phys.*, B469:419–444, 1996.

[30] J. P. Blaizot, Edmond Iancu, and A. Rebhan. Approximately self-consistent resummations for the thermodynamics of the quark-gluon plasma. I: Entropy and density. *Phys. Rev.*, D63:065003, 2001.

[31] J. P. Blaizot, E. Iancu, U. Kraemmer, and A. Rebhan. Hard-thermal-loop entropy of supersymmetric Yang-Mills theories. *JHEP*, 06:035, 2007.

[32] Jens O. Andersen, Eric Braaten, and Michael Strickland. Hard-thermal-loop resummation of the free energy of a hot quark-gluon plasma. *Phys. Rev.*, D61:074016, 2000.

[33] Jens O. Andersen, Eric Braaten, Emmanuel Petitgirard, and Michael Strickland. HTL perturbation theory to two loops. *Phys. Rev.*, D66:085016, 2002.

[34] M. Creutz, editor. *Quantum Fields on the Computer.* World Scientific, Singapore, 1992.

[35] Frithjof Karsch. Lattice QCD at high temperature and density. *Lect. Notes Phys.*, 583:209–249, 2002.

[36] Edwin Laermann and Owe Philipsen. Status of lattice QCD at finite temperature. *Ann. Rev. Nucl. Part. Sci.*, 53:163–198, 2003.

[37] Kenneth G. Wilson. CONFINEMENT OF QUARKS. *Phys. Rev.*, D10:2445–2459, 1974.

[38] F. Karsch, E. Laermann, and A. Peikert. The pressure in 2, 2+1 and 3 flavour QCD. *Phys. Lett.*, B478:447–455, 2000.

[39] C. R. Allton et al. Thermodynamics of two flavor QCD to sixth order in quark chemical potential. *Phys. Rev.*, D71:054508, 2005.

[40] Frithjof Karsch. Recent lattice results on finite temperature and density QCD, part I. *PoS*, CPOD07:026, 2007.

[41] Owe Philipsen. Status of Lattice Studies of the QCD Phase Diagram. *Prog. Theor. Phys. Suppl.*, 174:206–213, 2008.

[42] Roberto Casalbuoni. QCD critical point: A historical perspective. *PoS*, CPOD2006:001, 2006.

[43] Philippe de Forcrand and Owe Philipsen. Towards the QCD phase diagram. *PoS*, LAT2006:130, 2006.

[44] Philippe de Forcrand and Owe Philipsen. The curvature of the critical surface $(m_{u,d}, m_s)^{crit}(\mu)$: a progress report. *PoS*, LATTICE2008:208, 2008.

[45] S. Beolé. *Looking For Quark Gluon Plasma in Pb-Pb collision at 158 GeV/c.* PhD thesis, Universit Degli Studi Di Torin0, 1998.

[46] Rafael Derradi de Souza. *Produção Térmica de Partículas em Colisões Nucleares Relativísticas*. PhD thesis, Universidade Estadual de Campinas, 2008.

[47] *Lectures on Theoretical Physics*. Interscience, NY, 1959.

[48] A. Bialas, M. Bleszynski, and W. Czyz. Multiplicity Distributions in Nucleus-Nucleus Collisions at High-Energies. *Nucl. Phys.*, B111:461, 1976.

[49] Larry D. McLerran and Raju Venugopalan. Computing quark and gluon distribution functions for very large nuclei. *Phys. Rev.*, D49:2233–2241, 1994.

[50] Larry D. McLerran and Raju Venugopalan. Gluon distribution functions for very large nuclei at small transverse momentum. *Phys. Rev.*, D49:3352–3355, 1994.

[51] Larry D. McLerran and Raju Venugopalan. Green's functions in the color field of a large nucleus. *Phys. Rev.*, D50:2225–2233, 1994.

[52] Burkard C. Reisert. HERA Combined Cross Sections and Parton Densities. 2008.

[53] J. Breitweg et al. ZEUS results on the measurement and phenomenology of F2 at low x and low Q**2. *Eur. Phys. J.*, C7:609–630, 1999.

[54] Larry McLerran. The Color Glass Condensate and Glasma. 2008.

[55] L. D. Landau. On the multiparticle production in high-energy collisions. *Izv. Akad. Nauk SSSR Ser. Fiz.*, 17:51–64, 1953.

[56] B. B. Back et al. The PHOBOS perspective on discoveries at RHIC. *Nucl. Phys.*, A757:28–101, 2005.

[57] B. B. Back et al. Significance of the fragmentation region in ultrarelativistic heavy-ion collisions. *Physical Review Letters*, 91(5):052303, 2003.

[58] J. Adams et al. Measurements of transverse energy distributions in $au + au$ collisions at $\sqrt{s_{NN}} = 200gev$. *Phys. Rev. C*, 70(5):054907, Nov 2004.

[59] System size, energy, and centrality dependence of pseudorapidity distributions of charged particles in relativistic heavy-ion collisions. *Physical Review Letters*, 102(14):142301, 2009.

[60] B. B. Back et al. Charged-particle pseudorapidity distributions in au+au collisions at sqrt(s[sub nn]) = 62.4 gev. *Physical Review C (Nuclear Physics)*, 74(2):021901, 2006.

[61] K. Adcox et al. Measurement of the mid-rapidity transverse energy distribution from s(N N)**(1/2) = 130-GeV Au + Au collisions at RHIC. *Phys. Rev. Lett.*, 87:052301, 2001.

[62] J. D. Bjorken. Highly Relativistic Nucleus-Nucleus Collisions: The Central Rapidity Region. *Phys. Rev.*, D27:140–151, 1983.

[63] J. Adams et al. Experimental and theoretical challenges in the search for the quark gluon plasma: The star collaboration's critical assessment of the evidence from rhic collisions. *Nucl. Phys.*, A757:102–183, 2005.

[64] Johann Rafelski and Berndt Muller. Strangeness Production in the Quark - Gluon Plasma. *Phys. Rev. Lett.*, 48:1066, 1982.

[65] P. Koch, Berndt Muller, and Johann Rafelski. Strangeness in Relativistic Heavy Ion Collisions. *Phys. Rept.*, 142:167–262, 1986.

[66] B. I. Abelev et al. Systematic Measurements of Identified Particle Spectra in pp, d^+ Au and Au+Au Collisions from STAR. *Phys. Rev.*, C79:034909, 2009.

[67] John Adams et al. Identified particle distributions in p p and Au + Au collisions at s**(1/2) = 200-GeV. *Phys. Rev. Lett.*, 92:112301, 2004.

[68] Olga Yu. Barannikova. Probing collision dynamics at RHIC. 2004.

[69] Ekkard Schnedermann, Josef Sollfrank, and Ulrich W. Heinz. Thermal phenomenology of hadrons from 200-A/GeV S+S collisions. *Phys. Rev.*, C48:2462–2475, 1993.

[70] D. Teaney, J. Lauret, and E. V. Shuryak. A hydrodynamic description of heavy ion collisions at the SPS and RHIC. 2001.

[71] D. Teaney, J. Lauret, and Edward V. Shuryak. Flow at the SPS and RHIC as a quark gluon plasma signature. *Phys. Rev. Lett.*, 86:4783–4786, 2001.

[72] Ulrich W. Heinz and Peter F. Kolb. Early thermalization at RHIC. *Nucl. Phys.*, A702:269–280, 2002.

[73] Derek Teaney. Effect of shear viscosity on spectra, elliptic flow, and Hanbury Brown-Twiss radii. *Phys. Rev.*, C68:034913, 2003.

[74] Fabrice Retiere and Michael Annan Lisa. Observable implications of geometrical and dynamical aspects of freeze-out in heavy ion collisions. *Phys. Rev.*, C70:044907, 2004.

[75] J. Adams et al. Scaling Properties of Hyperon Production in Au+Au Collisions at $\sqrt(s_N N) = 200$ GeV. *Phys. Rev. Lett.*, 98:062301, 2007.

[76] C. Adler et al. Mid-rapidity Lambda and Antilambda production in Au + Au collisions at s(NN)**(1/2) = 130-GeV. *Phys. Rev. Lett.*, 89:092301, 2002.

[77] John Adams et al. Multi-strange baryon production in Au Au collisions at s(NN)**(1/2) = 130-GeV. *Phys. Rev. Lett.*, 92:182301, 2004.

[78] B. I. Abelev et al. Strange particle production in p + p collisions at s**(1/2) = 200-GeV. *Phys. Rev.*, C75:064901, 2007.

[79] B. I. Abelev et al. Enhanced strange baryon production in Au+Au collisions compared to p+p at sqrts = 200 GeV. *Phys. Rev.*, C77:044908, 2008.

[80] B. I. Abelev et al. Energy and system size dependence of ϕ meson production in Cu+Cu and Au+Au collisions. *Phys. Lett.*, B673:183–191, 2009.

[81] John Adams et al. Strange baryon resonance production in s(NN)**(1/2) = 200- GeV p + p and Au + Au collisions. *Phys. Rev. Lett.*, 97:132301, 2006.

[82] John Adams et al. K*(892) resonance production in Au + Au and p + p collisions at s(NN)**(1/2) = 200-GeV at STAR. *Phys. Rev.*, C71:064902, 2005.

[83] J. Cleymans, Burkhard Kampfer, M. Kaneta, S. Wheaton, and N. Xu. Centrality dependence of thermal parameters deduced from hadron multiplicities in Au + Au collisions at s(NN)**(1/2) = 130-GeV. *Phys. Rev.*, C71:054901, 2005.

[84] H. van Hecke, H. Sorge, and N. Xu. *Phys. Rev. Lett.*, 81:5764, 1998.

[85] Markus D. Oldenburg. Scaling of anisotropic flow in the picture of quark coalescence. *J. Phys.*, G31:S437–S442, 2005.

[86] B. I. Abelev et al. Centrality dependence of charged hadron and strange hadron elliptic flow from $\sqrt{(}s_N N)$ = 200 GeV Au+Au collisions. *Phys. Rev.*, C77:054901, 2008.

[87] Jean-Yves Ollitrault. Anisotropy as a signature of transverse collective flow. *Phys. Rev. D*, 46(1):229–245, Jul 1992.

[88] H. Sorge. Highly sensitive centrality dependence of elliptic flow: A novel signature of the phase transition in qcd. *Phys. Rev. Lett.*, 82(10):2048–2051, Mar 1999.

[89] H. Sorge. Soft transverse expansion in pb(158 agev) on pb collisions: preequilibrium motion or first order phase transition? *Physics Letters B*, 402(3-4):251 – 256, 1997.

[90] P. Huovinen, P. F. Kolb, U. Heinz, P. V. Ruuskanen, and S. A. Voloshin. Radial and elliptic flow at rhic: further predictions. *Physics Letters B*, 503(1-2):58 – 64, 2001.

[91] J. Adams et al. Azimuthal anisotropy in au+au collisions at $\sqrt{s_{NN}}$ = 200 GeV. 2004.

[92] J. Adams et al. Multi-strange baryon elliptic flow in au+au collisions at $\sqrt{s_{NN}} = 200$ GeV. *Phys. Rev. Lett.*, 95:122301, 2005.

[93] Stephen Scott Adler et al. Elliptic flow of identified hadrons in Au + Au collisions at s(NN)**(1/2) = 200-GeV. *Phys. Rev. Lett.*, 91:182301, 2003.

[94] B. I. Abelev et al. Partonic flow and Phi-meson production in Au + Au collisions at s(NN)**(1/2) = 200-GeV. *Phys. Rev. Lett.*, 99:112301, 2007.

[95] M. Oldenburg. Centrality Dependence of Azimuthal Anisotropy of Strange Hadrons in 200 GeV Au+Au Collisions. *J. Phys.*, G32:S563–S566, 2006.

[96] R. Hanbury Brown and R. Q. Twiss. A New type of interferometer for use in radio astronomy. *Phil. Mag.*, 45:663–682, 1954.

[97] R. Hanbury Brown and R. Q. Twiss. A Test of a new type of stellar interferometer on Sirius. *Nature*, 178:1046–1048, 1956.

[98] Gerson Goldhaber, William B. Fowler, Sulamith Goldhaber, and T. F. Hoang. Pion-pion correlations in antiproton annihilation events. *Phys. Rev. Lett.*, 3:181–183, 1959.

[99] Gerson Goldhaber, Sulamith Goldhaber, Won-Yong Lee, and Abraham Pais. Influence of Bose-Einstein statistics on the antiproton proton annihilation process. *Phys. Rev.*, 120:300–312, 1960.

[100] G. I. Kopylov and M. I. Podgoretsky. Interference of two-particle states in elementary-particle physics and astronomy. *Zh. Eksp. Teor. Fiz.*, 69:414–421, 1975.

[101] R. Lednicky. Correlation femtoscopy. *Nucl. Phys.*, A774:189–198, 2006.

[102] R. Lednicky and V. L. Lyuboshits. Final State Interaction Effect on Pairing Correlations Between Particles with Small Relative Momenta. *Sov. J. Nucl. Phys.*, 35:770, 1982.

[103] E. E. Salpeter and H. A. Bethe. A relativistic equation for bound-state problems. *Phys. Rev.*, 84(6):1232–1242, Dec 1951.

[104] Z. K. Silagadze. Wick-Cutkosky model: An introduction. 1998.

[105] S. Pratt. Pion interferometry for exploding sources. *Phys. Rev. Lett.*, 53:1219–1221, 1984.

[106] M. I. Podgoretsky. ON THE COMPARISON OF IDENTICAL PION CORRELATIONS IN DIFFERENT REFERENCE FRAMES. *Sov. J. Nucl. Phys.*, 37:272, 1983.

[107] S. Pratt. Pion Interferometry of Quark-Gluon Plasma. *Phys. Rev.*, D33:1314–1327, 1986.

[108] G. Bertsch, M. Gong, and M. Tohyama. Pion Interferometry in Ultrarelativistic Heavy Ion Collisions. *Phys. Rev.*, C37:1896–1900, 1988.

[109] Michael Annan Lisa, Scott Pratt, Ron Soltz, and Urs Wiedemann. Femtoscopy in relativistic heavy ion collisions. *Ann. Rev. Nucl. Part. Sci.*, 55:357–402, 2005.

[110] Urs Achim Wiedemann and Ulrich W. Heinz. Particle interferometry for relativistic heavy-ion collisions. *Phys. Rept.*, 319:145–230, 1999.

[111] J. Adams et al. Pion interferometry in Au+Au collisions at $\sqrt{s_{NN}} = 200$ GeV. *Phys. Rev.*, C71:044906, 2005.

[112] L. D. Landau. *Quantum Mechanics-Nonrelativistic Theory (Course on Theoretical Physics, Vol 3)*. Pergamon Pr, 1981.

[113] Richard Lednicky. Finite-size effects on two-particle production in continuous and discrete spectrum. *Phys. Part. Nucl.*, 40:307–352, 2009.

[114] R. Lednicky, V. L. Lyuboshits, B. Erazmus, and D. Nouais. How to measure which sort of particles was emitted earlier and which later. *Phys. Lett.*, B373:30–34, 1996.

[115] Ulrich W. Heinz and Q. H. Zhang. What can we learn from three-pion interferometry? *Phys. Rev.*, C56:426–431, 1997.

[116] Ulrich W. Heinz and Alex Sugarbaker. Projected three-pion correlation functions. *Phys. Rev.*, C70:054908, 2004.

[117] John Adams et al. Three-pion HBT correlations in relativistic heavy-ion collisions from the STAR experiment. *Phys. Rev. Lett.*, 91:262301, 2003.

[118] Z. Chajecki, T. D. Gutierrez, M. A. Lisa, and M. Lopez-Noriega. A A versus p p (and d A): A puzzling scaling in HBT@RHIC. *nucl-ex/0505009*, 2005.

[119] Zbigniew Chajęcki. *Global Conservation Laws and Femtoscopy at RHIC*. PhD thesis, The Ohio State University, 2009.

[120] I. P. Lokhtin et al. Heavy ion event generator HYDJET++ (HYDrodynamics plus JETs). *Comput. Phys. Commun.*, 180:779–799, 2009.

[121] Fabrice Retiere. Flow in ultra-relativistic heavy ion collisions. *J. Phys.*, G30:S827–S834, 2004.

[122] Scott Pratt. Resolving the HBT Puzzle in Relativistic Heavy Ion Collision. *Phys. Rev. Lett.*, 102:232301, 2009.

[123] I. P. Lokhtin and A. M. Snigirev. A model of jet quenching in ultrarelativistic heavy ion collisions and high-p(T) hadron spectra at RHIC. *Eur. Phys. J.*, C45:211–217, 2006.

[124] N. S. Amelin et al. A Fast Hadron Freeze-out Generator. *Phys. Rev.*, C74:064901, 2006.

[125] N. S. Amelin et al. Fast hadron freeze-out generator, part II: noncentral collisions. *Phys. Rev.*, C77:014903, 2008.

[126] Giorgio Torrieri et al. SHARE: Statistical hadronization with resonances. *Comput. Phys. Commun.*, 167:229–251, 2005.

[127] Dirk H. Rischke and Miklos Gyulassy. The time-delay signature of quark-gluon plasma formation in relativistic nuclear collisions. *Nucl. Phys.*, A608:479–512, 1996.

[128] Dirk H. Rischke. Hydrodynamics and collective behaviour in relativistic nuclear collisions. *Nucl. Phys.*, A610:88c–101c, 1996.

[129] M. A. Lisa et al. The E895 pi- correlation analysis: A status report. 2005.

[130] M. A. Lisa et al. Azimuthal dependence of pion interferometry at the AGS. *Phys. Lett.*, B496:1–8, 2000.

[131] P. Chung et al. Comparison of source images for protons, pi-'s and Lambda's in 6-AGeV Au + Au collisions. *Phys. Rev. Lett.*, 91:162301, 2003.

[132] H. Appelshauser et al. Hadronic expansion dynamics in central Pb + Pb collisions at 158-GeV per nucleon. *Eur. Phys. J.*, C2:661–670, 1998.

[133] H. Appelshauser et al. Two-proton correlations from 158-A-GeV Pb + Pb central collisions. *Phys. Lett.*, B467:21–28, 1999.

[134] S. V. Afanasiev et al. Bose-Einstein correlations of charged kaons in central Pb + Pb collisions at E(beam) = 158-A-GeV. *Phys. Lett.*, B557:157–166, 2003.

[135] I. G. Bearden et al. Space-time evolution of the hadronic source in peripheral to central Pb + Pb collisions. *Eur. Phys. J.*, C18:317–325, 2000.

[136] M. M. Aggarwal et al. Central Pb + Pb collisions at 158-A-GeV/c studied by pi- pi- interferometry. *Eur. Phys. J.*, C16:445–451, 2000.

[137] F. Antinori et al. Centrality dependence of the expansion dynamics in Pb Pb collisions at 158-A-GeV/c. *J. Phys.*, G27:2325–2344, 2001.

[138] John Adams et al. Azimuthally sensitive HBT in Au + Au collisions at s(NN)**(1/2) = 200-GeV. *Phys. Rev. Lett.*, 93:012301, 2004.

[139] B. I. Abelev et al. Pion Interferometry in Au+Au and Cu+Cu Collisions at RHIC. *Phys. Rev.*, C80:024905, 2009.

[140] K. Adcox et al. Transverse mass dependence of two-pion correlations in Au + Au collisions at s(NN)**(1/2) = 130-GeV. *Phys. Rev. Lett.*, 88:192302, 2002.

[141] Stephen Scott Adler et al. Bose-Einstein correlations of charged pion pairs in Au + Au collisions at s(NN)**(1/2) = 200-GeV. *Phys. Rev. Lett.*, 93:152302, 2004.

[142] Peter F. Kolb and Ulrich W. Heinz. Hydrodynamic description of ultrarelativistic heavy-ion collisions. 2003.

[143] Tetsufumi Hirano and Keiichi Tsuda. Collective flow and HBT radii from a full 3D hydrodynamic model with early chemical freeze out. *Nucl. Phys.*, A715:821–824, 2003.

[144] Ulrich W. Heinz. Early collective expansion: Relativistic hydrodynamics and the transport properties of QCD matter. 2009.

[145] Scott Pratt. Femtoscopy overview and the HBT puzzle. *Acta Phys. Polon. Supp.*, 1:489–492, 2008.

[146] R. A. Soltz. Review of systematic investigations of the R(out)/R(side) ratio in HBT at RHIC. *J. Phys.*, G31:S325–S329, 2005.

[147] Scott Pratt. The Long Slow Death of the HBT Puzzle. *Acta Phys. Polon.*, B40:1249–1256, 2009.

[148] Z. Chajecki. Identical particle correlations in star. *Nucl. Phys.*, A774:599–602, 2006.

[149] Adam Kisiel. Non-identical particle correlations in 130 AGeV and 200 AGeV collisions at star. *J. Phys.*, G30:S1059–S1064, 2004.

[150] J. Adams et al. Pion-kaon correlations in Au + Au collisions at $\sqrt{s_{NN}} = 130$ GeV. *Phys. Rev. Lett.*, 91:262302, 2003.

[151] E. D. Courant and H. S. Snyder. Theory of the alternating-gradient synchrotron. *Annals of Physics*, 3:1–48, January 1958.

[152] Gordon Baym. RHIC: From dreams to beams in two decades. *Nucl. Phys.*, A698:XXIII–XXXII, 2002.

[153] T. W. Ludlam. RHIC AND QUARK MATTER: A PROPOSED HEAVY ION COLLIDER AT BROOKHAVEN NATIONAL LABORATORY. BNL-35237,Published in Helsinki Quark Matter 1984:0240.

[154] Thomas W. Ludlam. RELATIVISTIC HEAVY IONS AT BROOKHAVEN: HIGH-ENERGY NUCLEAR BEAMS IN THE AGS AND RHIC. *Nucl. Phys.*, A447:349c–369c, 1986. BNL-37083.

[155] NEC. Peletron Charging System. *http://www.pelletron.com/charging.htm.*

[156] List of most common species for BNL Tandems. *http://tvdg10.phy.bnl.gov/species.html.*

[157] J. Alessi et al. Upgrade and Operation of the BNL Tandems for RHIC Injection. Presented at IEEE Particle Accelerator Conference (PAC2001), Chicago, Illinois, 18-22 Jun 2001.

[158] T. Satogata et al. Commissioning of RHIC Deuteron Gold Collisions. Particle Accelerator Conference (PAC 03) 12-16 May 2003, Portland, Oregon.

[159] L. Ahrens et al. The RHIC Injector Accelerator Configurations, and Performance for the RHIC 2003 Au d Physics Run. Particle Accelerator Conference (PAC 03) 12-16 May 2003, Portland, Oregon.

[160] C. J. Gardner et al. Setup and Performance of RHIC for the 2008 Run with Deuteron and Gold Collisions. EPAC'08, 11th European Particle Accelerator Conference, 23- 27 June 2008, Genoa, Italy.

[161] L. Ahrens et al. Setup and performance of the RHIC injector accelerators for the 2007 run with gold ions. Prepared for Particle Accelerator Conference (PAC 07), Albuquerque, New Mexico, 25-29 Jun 2007.

[162] H.E. Wegner P. Thieberger, M. McKeown. *IEEE Trans. Nucl. Sci. NS-30 (4) (1983) 2746.*

[163] P. Thieberger. POSSIBLE USE OF SYNCHROTRONS AS POSTACCELERATION BOOSTERS FOR TANDEMS. *Nucl. Instrum. Meth.*, A220:209–210, 1984.

[164] H. Hahn et al. The RHIC design overview. *Nucl. Instrum. Meth.*, A499:245–263, 2003.

[165] RHIC Design Manual. *http://www.agsrhichome.bnl.gov/NT-share/rhicdm/00_toc1i.htm.*

[166] J. W. Harris. The STAR experiment at the relativistic heavy ion collider. *Nucl. Phys.*, A566:277c–285c, 1994.

[167] K. H. Ackermann et al. Star detector overview. *Nucl. Instrum. Meth.*, A499:624–632, 2003.

[168] M. E. Beddo et al. STAR: Conceptual design report for the Solenoidal Tracker at RHIC. BNL-PUB-5347.

[169] F. Bergsma et al. The STAR detector magnet subsystem. *Nucl. Instrum. Meth.*, A499:633–639, 2003.

[170] S. U. Pandey et al. The silicon drift vertex detector for the STAR experiment at RHIC. *Nucl. Instrum. Meth.*, A477:88–92, 2002.

[171] L. Arnold et al. The STAR silicon strip detector (SSD). *Nucl. Instrum. Meth.*, A499:652–658, 2003.

[172] K. H. Ackermann et al. The STAR time projection chamber. *Nucl. Phys.*, A661:681–685, 1999.

[173] M. Anderson et al. The STAR time projection chamber: A unique tool for studying high multiplicity events at RHIC. *Nucl. Instrum. Meth.*, A499:659–678, 2003.

[174] K. H. Ackermann et al. The forward time projection chamber (FTPC) in STAR. *Nucl. Instrum. Meth.*, A499:713–719, 2003.

[175] M. Shao et al. Extensive particle identification with TPC and TOF at the STAR experiment. *Nucl. Instrum. Meth.*, A558:419–429, 2006.

[176] F. S. Bieser et al. The STAR trigger. *Nucl. Instrum. Meth.*, A499:766–777, 2003.

[177] C. Adler et al. The RHIC zero-degree calorimeters. *Nucl. Instrum. Meth.*, A461:337–340, 2001.

[178] M. Anderson et al. A readout system for the STAR time projection chamber. *Nucl. Instrum. Meth.*, A499:679–691, 2003.

[179] R. Bellwied et al. The STAR silicon vertex tracker: A large area silicon drift detector. *Nucl. Instrum. Meth.*, A499:640–651, 2003.

[180] S. U. Pandey et al. The silicon drift vertex detector for the STAR experiment at RHIC. *Nucl. Instrum. Meth.*, A477:88–92, 2002.

[181] D. Lynn et al. The STAR silicon vertex tracker: A large area silicon drift detector. *Nucl. Instrum. Meth.*, A447:264–273, 2000.

[182] Stephen Baumgart. *A Study of Open Charm Production in Heavy Ion Collisions of Center-of-Mass Energy 200 GeV per Nucleon.* PhD thesis, Yale University, 2009.

[183] E. Gatti and P. Rehak. Semiconductor drift chamber - an application of a novel charge transport scheme. *Nucl. Instrum. Meth.*, A225:608–614, 1984.

[184] David M. Read. The Silicon drift detector and its use in a vertex tracker. UMI-96-33268.

[185] E. Gatti, A. Longoni, M. Sampietro, and P. Rehak. DYNAMICS OF ELECTRONS IN DRIFT DETECTORS. *Nucl. Instrum. Meth.*, A253:393–399, 1987.

[186] V. Rykov. *private comunications.*

[187] Selemon Bekele. *Neutral Kaon Correlations in Au-Au Collisions at Center of Mass Energy of 200 GeV per Nucleon Pair.* PhD thesis, The Ohio State University, 2004.

[188] R. Bellwied et al. Studies of dynamics of electron clouds in STAR silicon drift detectors. *Nucl. Instrum. Meth.*, A439:507–512, 2000.

[189] V. E. Barnes et al. OBSERVATION OF A HYPERON WITH STRANGENESS -3. *Phys. Rev. Lett.*, 12:204–206, 1964.

[190] Javier Castillo. *Production de particules doublement étranges dans les collisions d'ions lourds ultra-relativistes à* $\sqrt{s_{NN} = 130} GeV$. PhD thesis, Université Paris 7 - Denis Diderot UFR de Physique, 2002.

[191] Magali Estienne. *Propriétés chimiques et dynamiques des collisions d'ions lourds aux énergies du RHIC par la mesure de la production des baryons doublement étranges dans l'expérience STAR.* PhD thesis, Université de Nantes, 2005.

[192] Magali Estienne. Multi-strange baryon production in au + au collisions at top rhic energy as a probe of bulk properties. *J. Phys.*, G31:S873–S880, 2005.

[193] Mercedes López Noriega. *Pion Interferometry in AuAu Collisions at a Center of Mass Energy per Nucleon of 200 GeV.* PhD thesis, The Ohio State University, 2004.

[194] M. Gyulassy, S. K. Kauffmann, and L. W. Wilson. Pion interferometry of nuclear collisions. I. Theory. *Phys. Rev.*, C20:2267–2292, 1979.

[195] M. G. Bowler. Coulomb corrections to Bose-Einstein correlations have been greatly exaggerated. *Phys. Lett.*, B270:69–74, 1991.

[196] Yu. Sinyukov, R. Lednicky, S. V. Akkelin, J. Pluta, and B. Erazmus. Coulomb corrections for interferometry analysis of expanding hadron systems. *Phys. Lett.*, B432:248–257, 1998.

[197] Michael Annan Lisa and Scott Pratt. Femtoscopically Probing the Freeze-out Configuration in Heavy Ion Collisions. 2008.

[198] R. A. Muller. Observation of cascade hyperon interactions. *Phys. Lett.*, B38:123–124, 1972.

[199] S. F. Biagi et al. MEASUREMENTS OF THE TOTAL CROSS-SECTIONS OF SIGMA- AND XI- ON PROTONS AND DEUTERONS BETWEEN 74-GeV/c AND 137-GeV/c. *Nucl. Phys.*, B186:1, 1981.

[200] Y. Cheng, F. Liu, Z. Liu, K. Schweda, and N. Xu. Transverse expansion in Au-197+Au-197 collisions at RHIC. *Phys. Rev.*, C68:034910, 2003.

[201] S. A. Bass et al. Hadronic freeze-out following a first order hadronization phase transition in ultrarelativistic heavy-ion collisions. *Phys. Rev.*, C60:021902, 1999.

[202] Scott Pratt and Silvio Petriconi. Alternative size and lifetime measurements for high-energy heavy-ion collisions. *Phys. Rev.*, C68:054901, 2003.

[203] P. Chaloupka. Non-identical particle correlations at 62 GeV and 200 GeV at STAR. *Nucl. Phys.*, A774:603–606, 2006.

[204] P. Chaloupka, M. Sumbera, and L. V. Malinina. pi Xi correlations: Model comparison and Xi*(1530) puzzle. *Acta Phys. Polon.*, B40:1185–1192, 2009.

[205] B. O. Kerbikov and L. V. Malinina. $\pi\Xi$ Correlations: an Interweaving of Resonance Interaction, Channel Coupling and Coulomb Effects. *Phys. Rev.*, C81:034901, 2010.

[206] B. O. Kerbikov, R. Lednicky, L. V. Malinina, P. Chaloupka, and M. Sumbera. $\pi^{\pm}\Xi^{\mp}$ Correlations and the $\Xi^*(1530)$ Puzzle. 2009.

[207] R. Lednicky. *private comunications - to be published.*

[208] Iu. A. Karpenko and Yu. M. Sinyukov. Energy dependence of pion interferometry scales in ultra- relativistic heavy ion collisions. *Phys. Lett.*, B688:50–54, 2010.

[209] F. James and M. Roos. Minuit: A System for Function Minimization and Analysis of the Parameter Errors and Correlations. *Comput. Phys. Commun.*, 10:343–367, 1975.

[210] R. Witt. Xi(1530)0 production in heavy-ion collisions and its implications for Delta(t(therm-chem)). *J. Phys.*, G34:S921–924, 2007.

[211] A. Kisiel, P. Szarwas, and F. Retiere. Non-identical particle correlations in star as a probe of emission asymmetries and radial flow. *Acta Phys. Polon.*, B35:47–53, 2004.